# AN ABSTRACT OF THE DISSERTATION OF

Matthew F. Nahan for the degree of Doctor of Philosophy in Mechanical Engineering presented on July 2, 1997. Title: A Nonlocal Damage Theory for Laminated Plate with Application to Aircraft Damage Tolerance

Abstract approved: Redacted for Privacy

Timothy C. Kennedy

Design of commercial aircraft structure, composed of composite material, requires the prediction of failure loads given large scale damage. In particular, a fuselage of graphite/epoxy lamination was analyzed for damage tolerance given a standard large crack that severed both skin and internal structure. Upon loading, a zone of damage is known to develop in front of a crack-tip in composite laminates; and, its material behavior within the damage zone is characterized as strain softening. This investigation sought to develop a computational model that simulates progressive damage growth and predicts failure of complex laminated shell structures subject to combined tensile and flexural load conditions. This was accomplished by assuming a macroscopic definition of orthotropic damage that is allowed to vary linearly through the shell thickness. It was further proposed that nonlocal plate strain and curvature act to force damage growth according to a set of uniaxial criteria. Damage induced strain softening is exhibited by degradation of laminate stiffness. An expression for the damage reduced laminated plate stiffness was derived which assumed the familiar laminated plate [ABD] stiffness matrix format. The model was implemented in a finite element shell program for simulation of fracture and evaluation of damage tolerance. Laminates were characterized for damage resistance according to material parameters defining nonlocal strain and the damage growth criteria. These parameters were selected using an inverse method to correlate simulation with uniaxial strength and fracture test results. A novel combined-

tension-plus-flexure fracture test was developed to facilitate this effort. Analysis was performed on a section of pressurized composite fuselage containing a large crack. Good agreement was found between calculations and test results.

# A Nonlocal Damage Theory for Laminated Plate with Application to Aircraft Damage Tolerance

by

Matthew F. Nahan

A DISSERTATION

submitted to

Oregon State University

in partial fulfillment of
the requirements for the
degree of

Doctor of Philosophy

Presented July 2, 1997
Commencement June 1998

Doctor of Philosophy dissertation of Matthew F. Nahan on July 2, 1997

APPROVED:

Redacted for Privacy

Major Professor, representing Mechanical Engineering

Redacted for Privacy

Head of Department of Mechanical Engineering

Redacted for Privacy

Dean of Graduate School

I understand that my thesis will become part of the permanent collection of Oregon State University libraries. My signature below authorizes release of my thesis to any reader upon request.

Redacted for Privacy

Matthew F. Nahan

# ACKNOWLEDGMENTS

The following dissertation is dedicated to my parents, John and Evolene Nahan, to lend a tangible rationale to the rearing of thirteen children. Let this dissertation be proof that their seed, shelter, love and expectations have been appreciated and have made a positive contribution to the world.

The author wishes to extend his appreciation to two admirable individuals who freely gave support and direction to this research effort. First, thanks are extended to Dr. Timothy C. Kennedy of the Department of Mechanical Engineering at Oregon State University, for the significant patience and expertise lent to this research effort. Significant freedom of scientific pursuit was possible because of Tim's support. Second, appreciation is extended to Larry B. Ilcewicz currently of the Boeing Commercial Aircraft Company, for his direction, support and enthusiasm. Larry directed me to Tim and facilitated considerable funding for this research effort. This research would not have been possible without him.

Finally, this work was supported by NASA grant NAG-1-1620 and monitored by J. H. Starnes. The author wishes to acknowledge helpful discussions with T. H. Walker, G. Bodine and B. Dopker of Boeing Commercial Airplane Company during the course of this research.

TABLE OF CONTENTS

# Table of Contents (Continued)

LIST OF FIGURES

LIST OF FIGURES (Continued)

LIST OF FIGURES (Continued)

LIST OF TABLES

# A Nonlocal Damage Theory for Laminated Plate with Application to Aircraft Damage Tolerance

## 1. Introduction

Damage tolerance is a design requirement common to aircraft, pipelines, and pressure vessels in general. It could be argued that it should be a requirement of any structure that effects the personal safety of humans. Should life supporting structure incur damage, it is desirable that the damage not progress. That is, it is desirable that the structure be damage tolerant. If the damage does progress, it is desirable that its growth be arrested by some design detail so as to prevent total failure. That is, it is desirable that the structure fail in a safe manner which is the essence of a fail-safe design philosophy. Damage tolerance analysis seeks to predict the operational load at which damage will grow in a dynamic manner. It is applied to ensure tolerance of damage in general and includes assessment of fail-safe design performance.

The sources of damage are many. They include fatigue cracks, maintenance induced damage, manufacturing flaws and foreign object impact. Therefore the set of possible damage conditions is infinite. Standards are typically established which, if met, would ensure that all likely damage conditions are adequately designed for. The damage theory developed herein is applied to the damage tolerance analysis of a large diameter commercial aircraft fuselage. The standard of damage, considered herein, is a 22 inch long crack that severs both the fuselage skin and an underlying frame member. Such a large damage condition was based upon the possibility that, between scheduled inspections, multiple small damage sites could become interconnected into a single large damage site. It also served to account for possible foreign object damage. Details of the damage standard, such as its sharp notch-tip and its tip location mid-way between frames, were selected to represent a worst case condition. The standard does not

represent a fail-safe condition since the defined damage is distant from the frame members which are assumed to serve a fail-safe role.

Behavior of an axially aligned fuselage crack is complicated by pressure induced bulging which looks much like a persons lips while blowing out a candle. The free edge of the crack face disrupts the normal equilibrium within the fuselage skin and causes an increased axial stress and flexure about the crack-tip. From an analytical perspective the behavior is strongly nonlinear.

High performance composites have been considered for many pressure vessel applications including aircraft fuselage design. The fuselage application, reported upon herein, is composed of graphite/epoxy laminated plate. Prior to dynamic growth of a crack in these materials, a zone of damage is known to develop ahead of the crack-tip. In metals a similar zone of plasticity develops ahead of a crack-tip. Unlike metals, however, these materials are known to exhibit a loss of stiffness due to damage. This behavior has been shown to significantly influence fracture strength; however, such softening is difficult to experimentally characterize and the complexity of the damage process has motivated a wide range of analysis techniques.

From an engineering perspective, a successful damage tolerance analysis method would not only be reasonably accurate but would also be affordable in application to large complex structure. A macroscopic model of the damage process was considered essential to ensuring such affordability. It has been assumed that the macroscopically salient feature of the damage process and subsequent fracture is the gross softening of the plate. This behavior is referred to as strain softening and is exhibited by a declining post-yield stress-strain relation. Plasticity has been successfully employed to model plate softening and commercial finite element programs are available for application to complex structure. Plasticity theory attains softening by allowing for growth of a plastic component of strain that results in permanent deformation. Alternatively, damage mechanics has been successfully employed but currently lacks the support of commercial finite element programs. Damage mechanics attains softening by allowing for a reduction in stiffness. Testing of material taken from within the damage zone of a

fracturing laminate suggests that stiffness degradation is significant (Ilcewicz et al., 1993). A theory of damage mechanics is proposed herein for structure composed of highly directional laminated composite plate.

Strain softening behavior results in a brittle-like response for a uniaxial strength test. Failure is localized to a narrow band of material across the width of the specimen. Any attempt to load the specimen beyond its ultimate strength results in damage and softening originating at the weakest material point. Such a condition is unstable under a constant load and leads to rapid failure of the specimen cross-section that includes the weakest point. Simultaneously, the rest of the specimen unloads and the specimen is severed. In finite element analysis, failure develops within a single row of elements. However, refinement of the finite element mesh results in an ever more narrow failure volume. In the limit, failure is predicted to occur with zero volume of material involved and no strain energy dissipated by the failure process. This analytic result is physically unreasonable. One way to correct this problem is to employ a nonlocal treatment of the material's constitutive model. This approach presumes that the response of any material point is dependent upon the state of stress or strain within its nonlocal neighborhood and not simply a function of stress or strain specific to its location. Nonlocal finite element analysis of a uniaxial test of strain softening material would result in a band of material failure of finite width irregardless of mesh refinement.

Macroscopic modeling of material behavior within the notch-tip damage zone should account for the directional nature of fracture strength within a laminate. A second order tensor representation of damage mechanics is proposed to establish an orthotropic damage effect within a plate. Flexure can induce a variation of damage through the plate thickness, the degree of which would depend upon the variation of ply orientation through the laminate thickness. Therefore it is proposed that the second-order tensor representation of damage be allowed to vary linearly through the laminate thickness. The effect of such damage upon laminate stiffness is developed in Section 3. The kinetics of damage growth due to nonlocal strain is proposed in Section 4. The theory was applied to the analysis of fuselage damage tolerance. The fuselage skin

laminate is experimentally characterized for damage growth in Section 6. Fuselage damage tolerance analysis is presented in Section 7.

Large-scale delamination can be a significant component of fuselage damage. This is especially true where skin is bonded to sub-structure (versus mechanically fastened). Large-scale delamination effects are neglected in the present analysis. Rather, flexure induced damage was given priority because flexure induced damage is expected to be a precursor to large scale delamination.

# 2. Literature Review

Literature was reviewed for its relevance to fracture analysis of laminated composite shell structure. Particular focus was given to analysis of aircraft fuselage structure since the application of the theory reported herein was the prediction of rupture for a composite fuselage with large scale damage to its crown (upper quadrant). Thus the following literature review sought to elucidate the methods of fracture analysis applicable to quasi-brittle, laminar composite, thin shell structure under static load conditions. The theories considered do not attempt to model dynamic crack growth which would occur during rupture, but rather predict that rupture has occurred.

## 2.1 Analysis of Fuselage Rupture

The stress intensity factor (SIF) of linear elastic fracture mechanics (LEFM) for notched pressurized cylinders was first established by Folias (1965a & b) in which, depending upon geometry, it was shown to be of a significantly greater value than that of a flat plate subjected to a similar membrane loading. The notch was shown to bulge outward, like lips blowing air, which introduces bending ahead of the notch-tip that interacts with membrane forces to augment the membrane SIF. An SIF for bending stresses was then established by Copley & Sanders (1969). Erdogan & Kibler (1969) established a plasticity corrected SIF by using the Dugdale plastic strip model. He later demonstrated that the Crack Opening Displacement (COD) method predicts failure on a more consistent basis across a range of vessel notch sizes (Erdogan & Ratwani, 1972). The Folias theory was further applied to laminated composite pressure vessels and failure was predicted using the Mar-Lin fracture criterion discussed below (Ranniger et al., 1995). Agreement between prediction and experimental results was mixed,

particularly for anisotropic lamination which deviated considerably from the isotropy assumed by Folias.

Finite Element Analysis (FEA) was applied to the problem in order to obtain results for vessel geometries outside the limits of the Folias theory and for notch sizes that were larger in comparison to the size of the vessel (Ehlers, 1986). For many practical problems, such as fuselage damage tolerance analysis, analytical results (including those of FEA) considerably overestimated the COD. However by including large deflection effects in the governing equations, within the framework of finite element analysis, the problem was largely addressed (Riks et al., 1989).

Particular to metal airframe construction, Swift (1987) presented an excellent historical overview of fuselage damage tolerance analysis. Composite fuselage damage tolerance has been a recent focus of the Advanced Technology Composite Aircraft Structures (ATCAS) program that was directed by the National Aeronautical and Space Administration (NASA). In particular the work contributed by the Boeing Co. evaluated the capability of many fracture theories in predicting the residual strength of composite structure with large notches (Walker et al., 1992 & Ilcewicz et al., 1993). Large scale testing was conducted on a flat stiffened panel with a 14" notch under uniaxial tension and on a curved multi-bay section of fuselage with a 22" notch and severed frame (Walker et al., 1993). Of particular note was the additional failure mechanism of stiffener separation from skin laminate which can preempt notch failure and make experimental correlation problematic (Dopker et al., 1994). DuBois (1996), using a finite element model of the tested fuselage panel and nonlinear strain-softening spring elements along the crack path, over-estimated failure by 25 percent. A drawback of this analysis was that flexural stiffness degradation, ahead of the notch, was not addressed.

## 2.2 Laminate Fracture Theory

Laminate fracture analysis methods can be grouped into two general groups, those that model individual micromechanic failure mechanisms such as matrix cracking or fiber breakage and those methods that are phenomenological in nature. The later type, being macromechanic, attempt to model the effects of damage rather than the damage itself. These effects can be interpreted to modify fracture toughness properties or as some post-yield nonlinear stress-strain behavior. Macromechanic fracture analysis is the focus of this thesis; however, reference will follow regarding the state and usefulness of micromechanic theories. Typical macromechanic theories incorporate parameters that are correlated with results of an affordable set of fracture tests. Being empirical, all theories can be made to agree with a single fracture condition. Thus the discerning criterion of model performance is its accuracy in application to other, more practical, structural configurations.

### 2.2.1 Macroscopic Fracture Criterion

A review of laminate fracture criterion was made by Walker et al., in which various models are compared for a large range of crack sizes (Walker, et al., 1991). The criterion of Mar & Lin, discussed below, was found to best predict large notch test results based upon parameters established from small coupon test results.

Linear Elastic Fracture Mechanics (LEFM), based upon the theory of elasticity, established a square-root stress singularity distribution ahead of a notch tip. For mode-I loading of a notch under a plane stress condition, LEFM predicts a variation of stress

$$\sigma(r) = \sigma^{\infty}\sqrt{a/2r} \qquad (2\text{-}1)$$

where "r" refers to the distance ahead of the notch tip, $\sigma^{\infty}$ the far-field stress, and "a" the half crack length. By defining a Stress Intensity Factor (SIF), $K_I$, as

$$K_I = \sigma^{\infty}\sqrt{\pi a} \tag{2-2}$$

it is possible to establish a critical value of the SIF which would apply to all crack sizes. However, LEFM suffers in that it predicts far-field failure stress values that approach infinity for notches of vanishing size, a result which is physically unreasonable. In practice, small cracks are ignored and a non-fracture strength criterion is relied upon.

Strictly speaking, LEFM is limited to perfectly linear elastic (and thus brittle) material behavior. However, due to the empirical nature of LEFM, material nonlinearity localized to a small fracture process zone (FPZ) ahead of the notch-tip is acceptable. The discerning issue is whether the FPZ remains confined to the area of linear stress concentration, as calculated by LEFM. The Irwin and Dugdale plastic zone models are two methods of addressing the effects of crack blunting due to plastic yielding while remaining within the framework of LEFM (Irwin, 1958, Dugdale, 1960).

To address larger scale material nonlinearity, many models have been entertained. Like the critical SIF of LEFM, a single parameter was sought which signifies fracture given any representation of material behavior within the FPZ. The Crack Tip Opening Displacement (CTOD) and J-integral methods provide such a measure. The CTOD method (Wells, 1961) employed analytical or numerical methods to quantify the crack tip separation. The critical CTOD value is measured at failure in a fracture test and is considered to be directly applicable to the full range of crack sizes and geometries. However, CTOD measurement requires a distinct crack which is often not evident in such quasi-brittle materials as laminar composites and concrete. The J-integral method (Rice, 1968) is especially powerful in that it characterizes fracture (unstable FPZ growth) given a FPZ surrounded by material undergoing nonlinear elastic and monotonically increasing stress-strain loading. For graphite/epoxy laminates as well as concrete, the FPZ may be of a size that is too large for LEFM application, but it occurs within a field of linear elasticity and thus the J-integral method offers no special advantage.

The above analysis methods were developed for brittle or plastic material behavior. However, high performance laminar composites and concrete do not exhibit appreciable plasticity. For these materials, simple tension tests suggest brittle behavior; but fracture tests indicate otherwise. In particular, the material does not nucleate and grow a through crack as realized in metals. As a result, fracture theories have been developed specifically for composites. Furthermore, many of these theories address the short-coming associated with LEFM which predicts ever higher strength as the notch length approaches zero. Waddoups et al. (1971), modeled the FPZ in composites as a tractionless extension of the actual notch. This approach is similar to the Irwin model for plasticity. Length of the crack extension was considered a material property; it and the SIF of the extended notch are two parameters that enable correlation to both a fracture test and no-notch failure.

A Point Stress (PS) criterion (Whitney & Nuismer, 1974 & 75) is another two parameter model; but in contrast to the method of Waddoups, the PS method avoids dependence upon LEFM. The PS method associates failure with the development of a stress equal that of the no-notch strength at some distance, $d_o$, ahead of the stress concentration. Linear elasticity is employed in calculating the stress field; but contrary to LEFM, the SIF is not used as a fracture parameter. Distance parameter $d_o$ represents a characteristic dimension for the FPZ and is assumed to be a material constant, applicable to all notch sizes. Based upon the general solution of an elliptical hole through an infinite plate, the limit-condition of a crack results in an exact expression for the notch-tip stress according to

$$\sigma(r) = \sigma^{\infty} \frac{a}{\sqrt{a^2 - r^2}} \tag{2-3}$$

The PS criterion specified that, for position $r = d_o$ ahead of the notch-tip, the stress would equal the no-notch failure strength $\sigma^o$. The criterion applied to equation (2-3) results in

$$\sigma^{\infty} = \sigma^{o}\sqrt{1-\left(\frac{a}{a+d_o}\right)^2} \qquad (2\text{-}4)$$

which relates the far-field fracture stress to the no-notch strength and characteristic dimension, $d_o$. Thus, $d_o$ is quantified via correlation with a fracture test.

A strain based method, similar to the PS method, was formulated by Poe (1983) in which a critical strain intensity factor and fiber failure strain are two parameters that enable correlation to both a fracture test and no-notch failure. A characteristic dimension and fiber failure strain can also serve as an equivalent set of failure parameters. The characteristic dimension corresponds to the distance ahead of the notch tip at which fracture will occur if the fiber failure strain is realized. The characteristic dimension was found to be relatively independent of layup and material as long as failure occurred by self-similar crack extension and experienced limited delamination and splitting.

A three parameter fracture method was derived by Pipes et al. (1979) which employed the unnotched laminate strength and a PS type characteristic dimension that was made to vary relative to the notch size according to a variable exponential power. Use of three failure parameters improved correlation over the range of notch size results but required two different sized fracture tests and a unnotched strength test to quantify parameters.

The above fracture methods assume a homogeneous material exhibiting linear stress-strain behavior. However, composites are inherently inhomogeneous, having both fiber and matrix constituents. Linear elastic analysis, of a crack whose tip contacts a neighboring material region has shown that the SIF is not of the classical square-root singularity form; rather it is of a singularity that is a function of the relative shear stiffness and Poison's ratio of the two constituents. This micromechanic consideration lent support to the two parameter macromechanic model of Mar & Lin (1977) in which the notched failure stress is of a non-classical exponential dependence upon notch length; that is

$$\sigma^{\infty} = H(2a)^{-m} \qquad (2\text{-}5)$$

Parameter "H" is the composite fracture toughness value and exponent "m" establishes the rate of stress singularity. The authors established "m" values ranging from 0.25 to 0.35 for various laminar composites which are comparable to a value of 0.5 for homogeneous material.

### 2.2.2 Strain Softening Models

Unlike metals or perfectly brittle materials, high performance composites can exhibit a gradual reduction in resistance to deformation after surpassing some threshold in strain. Such behavior is not captured in load controlled tension testing because the softening leads to a localized and catastrophic failure. Under tension loading, strain softening nucleates at some flaw-like anomaly which exhibits the lowest threshold strain in the specimen. Softening of the nucleus, under a constant load, requires that strain increase over the specimen cross-section containing the flaw. Elevated strain leads to more material surpassing a threshold strain and localization of failure across a narrow section of the specimen. The specimen material outside of the band of localized softening undergoes simultaneous relaxation. Under most load conditions, this process is unstable and failure appears brittle and catastrophic. On the other hand, fracture testing of such material shows a gradual failure progression. This behavior has been associated with significant strain softening in the FPZ while material outside of the FPZ maintains specimen integrity. Such failure of strain softening material has often been referred to as quasi-brittle.

Hillerborg et al. (1976) pioneered the development of strain softening models for concrete using a simple stress-displacement relation associated with cohesive restraint during crack face separation. The method utilized nonlinear numerical analysis to model the progression of the FPZ. Hillerborg later referred to the method as the Fictitious Crack Model, FCM, in work which compared its performance to several other models discussed above (Hillerborg, 1983). The FCM method simplifies the area of potential

strain softening to a line along which the notch could advance. Upon reaching the threshold stress, material at the notch tip separates while continuing to support a lesser stress, representing partial ligament integrity. Further separation leads to total loss of resistance and advancement of the tractionless notch surface. Hillerborg employed a linear stress-displacement softening behavior, such as that illustrated in Figure 2.1 which results in an blunting of the notch-tip stress distribution. The notch-tip stress distribution evolves under increasing load and an example snap-shot is shown in Figure 2.2 at a stage in which material at the notch-tip location has completely exhausted its strain-softening potential and the stress free surface of the notch has in effect grown.

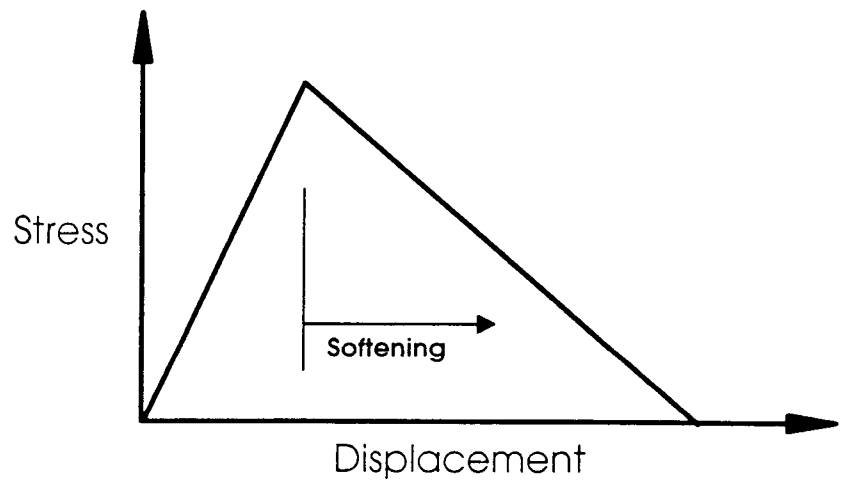


Figure 2.1 Material Stress vs. Displacement Relation of the Fictitious Crack Model.

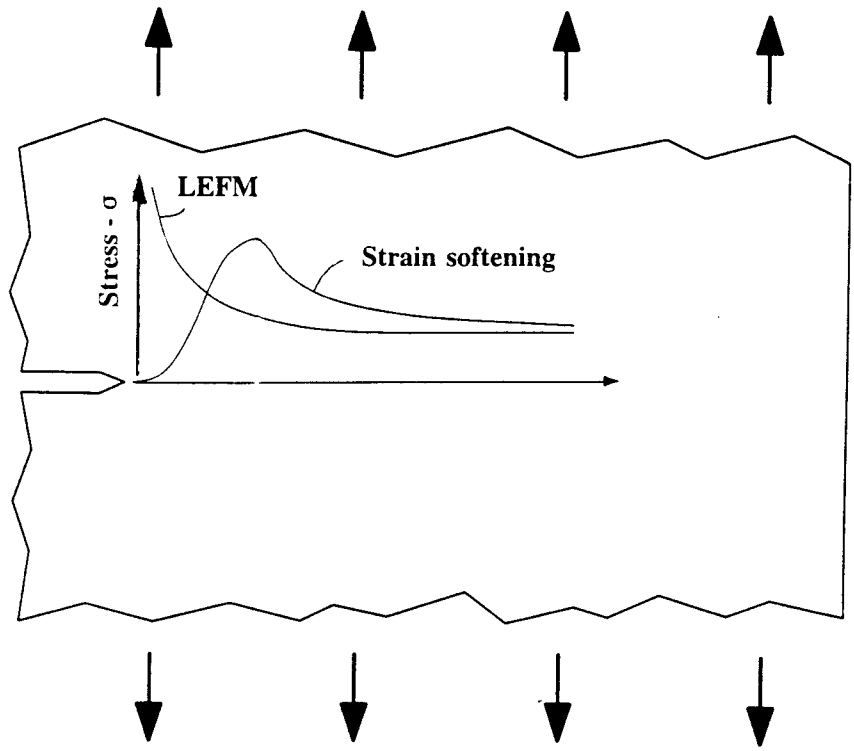


Figure 2.2 Stress Distributions within the Fracture Process Zone.

The FCM method was originally developed for concrete but later applied to laminated composites (Backlund & Aronsson, 1986) and various test specimen designs (Hollmann & Backlund, 1988). Depending on the complexity of the stress-displacement function, any number of parameters could be employed to characterize degradation within the FPZ; but at a minimum, the linear softening function is a two parameter model. Some have used multi-segmented-linear stress-displacement FPZ behavior (Carpinteri, et al., 1987 & Dopker et al., 1994) to demonstrate the insufficiency of the linear function of Figure 2.1 and the significance of a knee in the softening portion of the relationship. The previously mentioned fuselage analysis by DuBois used the FCM method and employed bilinear softening for membrane behavior while ignoring flexural softening. FCM has been widely employed due to its conceptual simplicity and

compatibility with commercial finite element programs. However its deficiencies are that the path of crack growth must be assumed apriori and it offers an incomplete representation of multi-dimensional continuum degradation within the FPZ volume.

Fracture tests of concrete and composites indicate that the FPZ encompasses a material volume of significant width normal to the crack and yet the FCM recognizes none. As an alternative, Bazant (1984a) proposed a Crack Band Model (CBM) in which a stress-strain softening relation was proposed for characterizing the FPZ as a band of degraded material. The band width, normal to the crack, is considered a material constant and the state of strain softening is uniform across its width. The CBM and FCM methods are essentially equivalent if the deformation across the band width, due to strain, is equal to the stretch of the cohesive FCM spring. At a minimum, however, the CBM is a three parameter model due to the addition of the band width as a material constant.

Bazant (1984a) used the CBM to demonstrate fracture specimen size effects, particularly for such materials as concrete and composites. Using a simplified interpretation of the CBM to model fracture, the general size effect law

$$\sigma_N = \frac{B * f_u'}{\sqrt{1+\beta}} \tag{2-6}$$

was established based upon crack growth energy release rate considerations. The size effect law relates the far-field notched strength, $\sigma_N$, to a non-dimensional size parameter, $\beta$, which is a function of specimen size and band width. Parameter $f_u'$ is the tensile strength and B is characteristic of the strain energy released from a complete softening of the material. As shown in Figure 2.3, the size effect law is consistent with the no-notch strengths as well as LEFM for specimen sizes much greater than that of the FPZ.

Bazant (1994) recently investigated the size effect for fracture of composites. Due to its simplicity, the CBM method offered clarity to the size effect issue and established the importance of modeling the volume of material undergoing strain softening. The CBM assumes, in consideration of energy dissipation, that all material

within the FPZ has experienced complete softening. In reality, however, the FPZ includes material having only partially softened and still contributes a cohesive resistance to fracture. This portion of the FPZ is referred to as being active.

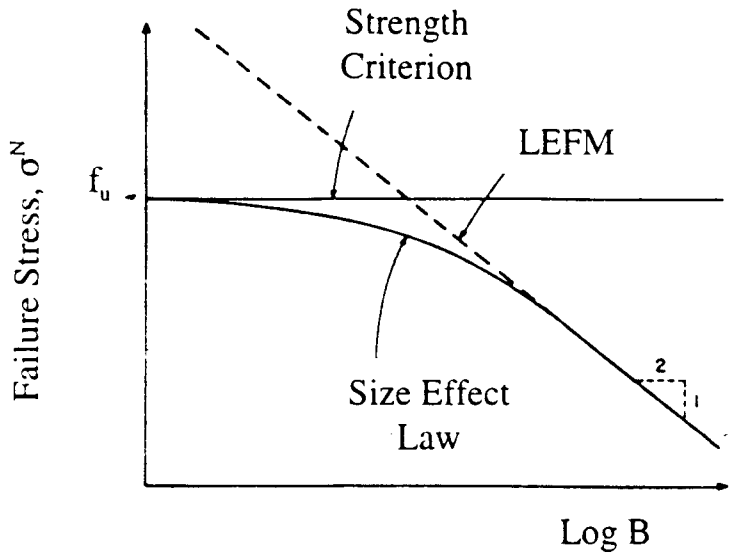


Figure 2.3 Size Effect According to Crack Band Model.

To realistically represent stress-strain softening within the FPZ, continuum mechanics has recognized two forms of strain softening: that associated with stiffness degradation (Figure 2.4a), and that associated with yield limit degradation (Figure 2.4b). Either or both forms of softening can evolve in a material as shown in Figure 2.5 for concrete loaded in tension. Yield limit degradation is associated with accumulation of permanent strain, no reduction in stiffness, and is modelled using the theory the of plastic deformation (Bazant & Lin, 1988a). Stiffness degradation is associated with progressive fracture and a variety of methods exist to model this behavior. The Smeared Cracking

Model (Bazant & Lin, 1988b) addressed stiffness degradation representative of cracks of a common orientation. Stiffness degraded as the secant modulus of the stress-strain softening relation. Stiffness degradation has also been modelled using damage mechanics as discussed below. Many authors have proposed methods to potentially model both modes of strain softening, simultaneously, for elasto-plastic fracturing materials (Bazant & Kim, 1979, Han & Chen, 1986, Ju, 1989, Hansen & Schreyer, 1994).

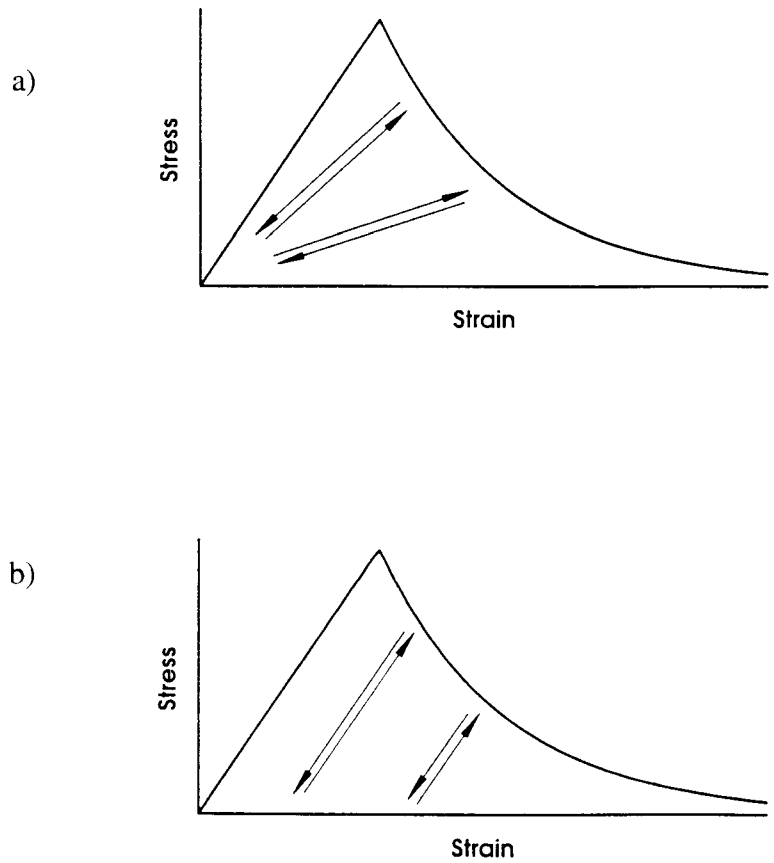


Figure 2.4 Strain Softening a) Stiffness Degradation. b) Yield-Limit Degradation.

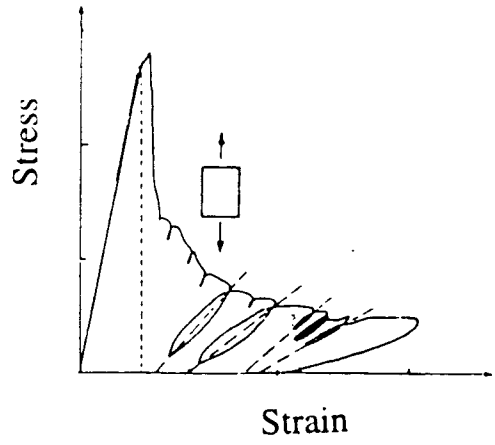


Figure 2.5 Tensile Stress-Strain of Concrete - Both Strain Softening and Permanent Strain Suggested (Mazars et al., 1989a).

The Crack Band Model can be modelled using Finite Element Analysis; however strain softening in a FEA model localizes to a single row of elements. Therefore the element size used to model the FPZ must be of the band width size. Any other size would constitute a different material behavior. Dopker et al. (1994) simulated fracture of graphite/epoxy laminates using the yield limit degradation technique and the crack band model. ABAQUS, a commercial FEA code, was employing in that effort and incremental plasticity theory controlled bi-linear stress-strain softening behavior (Ilcewicz et al., 1993). The steep descent of stress in the softening behavior of the graphite/epoxy laminates created challenging convergence difficulties which were overcome using dynamic nonlinear solution techniques. The analysis correlated well with fracture tests and was found to be superior to the fracture criteria discussed above.

### 2.2.3 Localization Limiting Theories

The element size limitation discussed above is undesirable because it prevents the investigation of behavioral detail within the FPZ. If the element size limitation were discarded, then upon progressive mesh refinement, the FPZ tends to localize to a region of vanishing volume. This would imply that structural failure ultimately occurs with no energy dissipation, a result which is physically unrealistic. The root of this problem is not numerical; but rather, for the example of static uniform tension, it is associated with the loss of ellipticity of the incremental equilibrium equations and bifurcation between paths of continued homogeneity and inhomogeneity between softening and unloading regimes (Rice, 1977). At the point of bifurcation, we know the orientation of localization but its width is left undetermined. For this reason several unconventional continuum theories have been considered which offer the ability to limit the width of strain localization and maintain ellipticity of static equilibrium equations. These include non-local spacial integration, micro-polar theory and displacement field enrichment using higher-order gradient terms. Work of de Borst & Mahlaus (1991) considered each of these theories

The framework of micro-polar continuum mechanics (Eringen, 1968) was established by the Cosserat brothers in 1909. It has received little interest until recently. Micro-polar continuum mechanics differs from classical elasticity in that material points have additional rotational degrees of freedom and corresponding couple stresses. The micro-rotational stiffness is dependent upon a characteristic length parameter which translates into a finite width of strain localization for softening materials. Recent efforts have employed plastic deformation theory for strain softening material in the context of micro-polar continuum (de Borst & Muhlhaus, 1991). De Borst noted that those degrees of freedom that are particular to micro-polar theory are activated only under conditions of shear, a condition that is satisfied to a varying degree, in fracture. However, he suggests that "when decohesion is the predominant failure mode, rather than frictional slip, the Cosserat effect is generally too weak to preserve ellipticity of the boundary

value problem". Micro-polar theory has been incorporated into FEA of fracture for linear elasticity (Kennedy & Kim, 1987); however, no work has been identified which incorporates strain softening and FEA of fracture.

Incorporating nonlocal averaging into strain softening constitutive equations has also been shown to limit strain localization. The classical approach of nonlocal theory was developed in the 1960's (Kroner, 1967, Eringen & Edelen, 1972) but it did not work in application to strain softening materials. This lead Bazant et al., (1984b,c,d) to introduce certain modifications to the classical approach in the form of an imbricated theory. Although the theory worked, it proved to be inconvenient due to the necessity of modeling material as a composite of local and nonlocal continuum. It was then proposed that only those terms responsible for strain softening be treated in a nonlocal manner while the elastic behavior remains local (Pijaudier-Cabot & Bazant, 1987). This approach has worked well and continues to see application and development.

For strain softening of the yield limit degradation type, the plastic strain tensor (Bazant & Lin, 1988a) as well as the scaler hardening-softening parameter (Stromberg & Ristinmaa, 1996) have acquired nonlocal form. All nonlocal analysis for strain softening of the stiffness degradation type has relied upon damage mechanics in which damage, defined as a state variable in addition to stress and strain, affects material stiffness. Nonlocal treatment has been applied directly to the local damage variable (Stevens & Krauthemmer, 1989, Xia & Tao, 1993 & Chen & Schreyer, 1994) or to the strain-based force behind damage growth (Pijaudier-Cabot & Bazant, 1987, Bazant & Lin, 1988b, Valanis, 1991, Brekelmans, 1993, de Vree et al., 1995 & Kennedy & Nahan, 1996).

Nonlocal averaging has typically employed a radially varying isotropic weight function that does not evolve during strain softening (Pijaudier-Cabot & Bazant, 1987, Bazant & Lin, 1988b). Its shape is defined using a material characteristic length parameter and directly influences the ultimate width of strain localization. Recent application to anisotropic laminates has retained the assumption of nonlocal isotropy Kennedy & Nahan, 1996) without investigating its legitimacy. Other work has sought

to define non-isotropic nonlocal weighting by considering the micromechanic influence of neighborhood crack interactions (Bazant, 1994).

Strain Localization can also be controlled by adding spacial derivatives of strain within the stress-strain softening relation. Local stress becomes a function of local strain and higher order derivatives of the strain field. The higher ordered gradient terms can be thought of as macro-manifestation of such micro-processes as bridging. When a material point reaches the threshold of softening, it is restrained from collapsing if its strain is elevated above that of surrounding material, as expressed by high-order strain terms. Such a formulation may be derived by taking a Taylor series expansion of the nonlocal strain integral discussed above (de Borst & Muhlaus, 1991). Strain derivatives of an even order characterize the symmetric nature of the strain field about a material point; and as such, they contribute no directional bias in limiting localization. Indeed the odd ordered terms, derived form Taylor expansion of a symmetric nonlocal integral, are identically zero. As such, the first order strain gradient enrichment (Schreyer & Chen, 1986) is held suspect. Good results have been obtained using a second order strain gradient enrichment (Belytchko & Lasry, 1988, de Borst & Muhlhaus, 1991, Brekelmans, 1993, deVree & Brekelmans, 1995).

Localization control, for materials of the yield limit degradation type, has been achieved by enriching the effective plastic strain with the spacial Laplacian of the effective plastic strain (de Borst & Muhlhaus, 1992 & Sluys et al., 1993). Their FEA formulation produced a non-symmetric tangent stiffness matrix which presents difficulties for adaptation of most nonlinear FEA codes. Although this approach has not been applied to fracture analysis, no barriers to this extension have been identified.

### 2.2.4 Damage Theory

Damage theory constitutes the definition of a damage variable and the kinematic description of its growth. Damage theory has been employed to model such modes of

failure as elastic stiffness degradation and fatigue and has been formulated along with plastic deformation for elasto-plastic degrading materials. Several reviews of damage theory are available (Krajcinovic, 1984, 1985, Chaboche, 1990, Lemaitre, 1992).

The introduction of damage theory (Kachanov, 1958) included a scaler variable which represented the accumulated density of microvoids for the modeling of material creep rupture. Damage parameter, D, has been interpreted as the effective area lost due to nucleation and growth of voids or micro-cracks and evolves from a value of zero to unity, representing total degradation. The basic principals of damage mechanics are presented below for the simple one dimensional case. With respect to the uniaxially loaded cylinder shown in Figure 2.6, damage is defined as the ratio of damage site area to nominal cross-sectional area (Lemaitre, 1984); i.e.,

$$D = \frac{S_d}{S} \tag{2-7}$$

where:

$$0 < D < 1 \tag{2-7a}$$

Damage varies from a value of 0 to 1, the later representing complete material separation and failure. This definition has lead to the concept of a damage effective stress associated with material located between the damage sites. The average stress realized by such material is

$$\tilde{\sigma} = \frac{P}{S - S_d} = \frac{\sigma}{(1 - D)} \tag{2-8}$$

From this basic premise, damage theories have followed various paths to achieve significant diversity. Critical to softening of the stiffness degradation type is determination of a damage effective stiffness, $\tilde{E}$, and it has been arrived at using either of two principles. The Strain Equivalence Principle (Lemaitre, 1971) states that the strain associated with a damaged state under applied stress is equivalent to the strain associated with its undamaged state under the effective stress; i.e.,

$$\frac{\sigma}{\tilde{E}} = \frac{\tilde{\sigma}}{E} \tag{2-9}$$

Entering equation (2-8) into equation (2-9) results in the damage effective stiffness

$$\tilde{E}=E(1-D) \tag{2-10}$$

This approach to formulation of damage effective stiffness has been used by many (Lemaitre, 1984, Pijaudier-Cabot & Bazant, 1987, Bazant & Lin, 1988b, Ju, 1989). The same formulation could be arrived through consideration of a damage effective strain, $\tilde{\varepsilon}$, and a stress equivalence principle. However no literature has been identified which utilizes this equivalent approach and it will therefore not be developed herein. A probable reason for its lack of use is that it would offer no advantage over the traditional effective stress/equivalent strain approach.

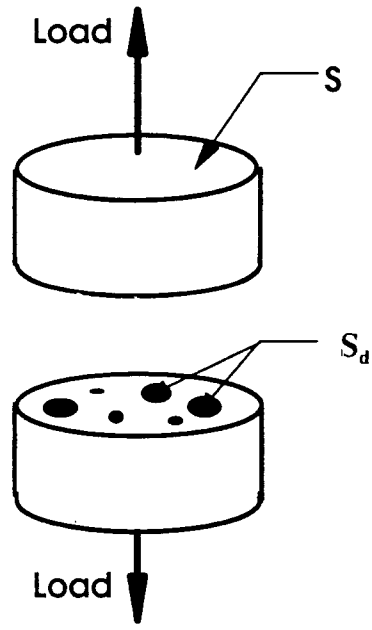


Figure 2.6 One-Dimensional Damage Model

Another approach uses the Principle of Elastic Energy Equivalence (Cordebois & Sidoroff, 1979) to arrive at the damage effective stiffness. It proposes that the strain energy within a damaged material is equally represented by that of damage effective stress acting through the nominal stiffness and that of classical stress acting through a damage effective stiffness; i.e.,

$$\frac{1}{2E}\tilde{\sigma}^2 = \frac{1}{2\tilde{E}}\sigma^2 \tag{2-11}$$

Substituting the effective stress of equation (2-8) into equation (2-11) yields the damage effective stiffness

$$\tilde{E}=E(1-D)^2 \tag{2-12}$$

This principle has been used extensively (Cordebois & Sidoroff, 1979, Lee et al., 1985, Chow & Wang, 1987, Kennedy & Nahan, 1996).

A damage effective strain can also be considered in this formulation as developed by Lee et al. (1985). If $U^e$ refers to the elastic strain energy of a material, then the elastic strain associated with a damaged state is

$$\varepsilon = \frac{\partial U^e(\sigma,D)}{\partial\sigma} = \frac{\partial}{\partial\sigma}\left\{\frac{1}{2\tilde{E}}\sigma^2\right\} = \frac{\sigma}{\tilde{E}} = \frac{\sigma}{E(1-D)^2} \tag{2-13}$$

which is the expected result for stiffness degradation due to damage. Equation (2-13) can be re-arranged to identify the damage effective strain, $\tilde{\varepsilon}$, as being complementary to the effective stress.

$$\varepsilon(1-D) = \frac{\sigma/(1-D)}{E} = \frac{\tilde{\sigma}}{E} = \tilde{\varepsilon} \tag{2-14}$$

Physically, the damage effective strain can be rationalized as the averaged state of strain experienced by material between damage sites. An alternate derivation of $\tilde{\varepsilon}$ is obtained

by defining damage as the ratio of deformation due to void growth of crack opening, $\delta_d$, to the total deformation, $\delta$ (Brekelmans, 1993); i.e.,

$$D = \frac{\delta_d}{\delta} \tag{2-15}$$

The effective strain is therefore

$$\tilde{\varepsilon} = \delta/L - \delta_d/L = \delta/L - \delta D/L = \varepsilon(1-D) \tag{2-16}$$

where L refers to the nominal ligament length. Little application of the effective strain concept has been identified in literature. However, it has been presented above because it is the basis of the damage theory developed herein. Having formulated a definition of effective strain, expression of the strain energy equivalence principle in terms of strain would again produce the effective stiffness relation of equation (2-12).

The scaler one-dimensional relations of equations (2.10) and (2.12) will take on more complexity for the various representations of damage and material anisotropy. Both formulations can represent damage effects upon a material because their respective damage growth kinetics will be compensatory (Hansen & Schreyer, 1994).

Damage, being an internal state variable, has an associated generalized force of equal order. Many have chosen a form of strain or stress as the damage force since these entities are familiar and offer physical clarity. For example Bazant formulated a uniaxial damage model for plate media (using a single fixed micro-crack orientation) and chose strain normal to the crack plane as the force behind the damage growth (Bazant & Lin, 1988b). De Vree & Brekelmans (1995) employed Von Mises equivalent strain as the force behind their isotropic scaler damage. Other scaler damage models have employed an equivalent scaler strain based upon only the tensile components of principle strain (Stevens & Krauthemmer, 1989). For higher order damage models, individual damage components could be associated with independent forces and kinematics (Krajcinovic, 1985). As an example Kennedy & Nahan (1996) utilized a second order damage tensor

of fixed principal orientation equal to the principal laminate axis, and each principal component evolved relative to the component of strain in their respective directions.

The intuitive selection of a damage force, mentioned above, could be considered arbitrary. Thus, many have employed the framework of thermodynamics of dissipative material for greater rigor in defining the damage force as the damage energy release rate. Inherent in the thermodynamic formulation is the definition of material free energy which is often expressed as the elastic strain energy density. For example, Pijaudeir-Cabot & Bazant (1987) used an elastic strain energy density that was dependent upon a scaler definition of damage through the effective stiffness relation of equation (2.10). This resulted in a damage force equal to the strain energy associated with the undamaged material stiffness. Thus, thermodynamics established yet another scaler equivalent strain as the damage force. The second-order damage theory of Lee et al. (1985) used the strain energy equivalence principle resulting in a thermodynamic damage force that was quadratic in strain and linearly dependent upon damage. Others have embellished upon the constitution of free energy to include terms representing void and micro-crack surface energy (Hansen & Schreyer, 1994) and damage dependent residual strain energy (Ramtani et al., 1992, Lesne, 1992). Thermodynamics thus offers significant flexibility in formulating the energy contribution to the damage process.

The kinetics of damage evolution kinetics can be established for individual components of the damage tensor (Kennedy & Nahan, 1996). The damage-force relationship is established from experimental association with material stiffness reduction. Although this approach works well for defining scaler damage kinetics, its application to individual components of a damage tensor could lead to an unwieldy number of criteria and can have limitations in representing interaction effects. Alternatively a dissipative potential can be employed, following the theory of plastic flow, which defines a surface in the space of damage forces which envelopes all states that can be reached without any energy dissipation (i.e. without further damage growth). The potentials are composed of invariant scaler, quadratic or higher powered functions of the damage force so as to be valid irregardless of coordinate basis. Damage force

growth can then expand the damage surface according to the normality rule and consistency condition to establish a coordinated and rigorous basis for tensorial damage evolution (Lee et al., 1985, Ju, 1989, Hansen & Schreyer, 1994, Ramtani et al., 1992).

### 2.2.5 Micromechanic Damage Theory

Micromechanics has been used to model both stress-strain softening in general and the cohesive stress-displacement softening across a single macro-crack tip. The latter have addressed fiber bridging and pull-out strengths and their evolution with crack face opening (Li, 1990, Llorca & Elices, 1992). Relevant to this thesis, however, are those theories that characterize stress-strain softening on a progressive multi-dimensional continuum basis and reflect gradual material degradation. These are in contrast to theories of the ply elimination type which could be considered crude. The intent of this review is not to be complete but rather to site examples and describe the current level of application.

Of three example methods, all separate damage of fibers from that of the matrix. The theory of Voyiadjis & Kattan (1993) employed separate phenomenological second order damage tensors for fiber and matrix constituents. The resultant laminate compliance tensor was related to such a representation of damage using the rule of mixtures and the principle of energy equivalence. Damage kinematics was formulated based upon the usual consistent and normal expansion of a damage surface that is quadratic in terms of the thermodynamic damage force. Numerical and experimental verification was not offered.

The theory of Lo et al. (1993) employed phenomenological second order damage tensors to represent intraply matrix and interply delamination damage for fatigue degradation. Damage growth obeyed a power law relation with respect to the number of load cycles which is similar to the well known da/dN macro-crack fatigue growth

formulation. The fiber was subject to a local maximum strain failure condition. Numerical application was made to a cross-ply laminate with a circular cutout.

The theory of Shahid & Chang (1995a,b) was implemented numerically and demonstrated using a number of laminates and fracture conditions. Their experiments addressed the same graphite/epoxy laminate that constitutes the fuselage skin laminate investigated herein. According to the theory, stiffness degradation was associated with three scaler damage parameters for each ply which reflected the state of matrix crack density, fiber/matrix debonding and fiber failure. Matrix crack damage evolved until the matrix cracking and fiber-matrix shear-out failure criteria were satisfied relative to strength parameters that evolve with damage. Matrix crack induced softening was computed using simplified analytical solutions for groups of three aligned orthotropic plies with co-oriented matrix cracks within the middle ply. Fiber damage resulted in progressive isotropic stiffness degradation that eventually lead to total ply failure. Interestingly, fiber damage was computed on an essentially nonlocal basis but was derived from statistical micromechanics. Fiber failure was the dominant damage mode; and the size of its nonlocal interaction zone was shown to be the discerning parameter in simulating significant differences in fracture toughness between equal laminates of different manufacturing origins.

### 2.2.6 Flexure of Strain Softening Material

The investigation of flexural strain softening has been limited, and no work was identified that specifically addressed fracture resistance given a through crack in a flexed plate. Of special interest is the work of Chuang & Mai (1989) in which analytical solutions were obtained for a beam of tension softening material under pure bending conditions; fracture was not considered. The beam was assumed to be homogeneous through its thickness and the stress-strain softening relation for tension loading was known. The analysis identified a moment-curvature relation that also exhibited softening

characteristics. Relative to a perfectly brittle material (instantaneous loss of load resistance at some threshold strain), strain softening was predicted to increase flexural strength by as much as three-fold.

Given a beam or plate that is homogenous through its thickness, any of the previously discussed macromechanic strain softening models for in-plane load behavior could be applied to flexural problems using layered finite element analysis. The analysis could employ implicit or explicit layering. Implicit layering divides the cross-section of each element into layers; each layer is subject to a uniform strain according to its position from the neutral axis and the resultant element flexural stiffness is based upon integration of the softening in each layer. This technique was employed by Dopker et al. (1994), using a yield limit degradation type softening model, even though the laminate could not be considered homogeneous through its thickness. Explicit layering establishes a finite element for each layer which greatly increases the computational costs.

Considering that micromechanic damage models already operate on the ply level, they should apply to flexural conditions without conceptual modification. The work of Reddy et al. (1995) is the only identified example of this type of effort. Their work also touched upon effects of combined tension plus flexure using conditions similar to that analyzed and tested as part of this thesis effort.

No literature was identified that analyzed fracture of plates having a through-thickness notch and subject to strain softening behavior. However, for linear elastic behavior of laminated composites under pure bending conditions, Zhao et al. (1993) used a modified form of the Point Stress (PS) fracture criterion to study flexural fracture strength. The usual limitations of the PS criterion were retained in this effort. Kwon (1993) studied the effects of partial crack closure in a composite laminate subject to bending. However, crack closure is not relevant to the tension dominant fracture considered in this dissertation.

## 2.3 Measurement of Strain Softening

Direct measurement of the stress-strain softening behavior from a typical tension test is not possible due to strain and damage localization to a narrow band of the specimen length. Using displacement control, many authors have employed this type of test but results are limited to stress-displacement softening associated with the total band of softening material. That is, the total material experiencing strain softening must be treated as a row of springs. Although such results would satisfy the line-spring model (fictitious crack model) introduced in Section 2.2.2, they would not satisfy the objective of this research to characterize, on a continuum basis, the material's stress-strain softening behavior.

Although not novel, Bazant & Pijaudeir-Cabot (1989) and Mazars (1989b) managed to obtain continuum stress-strain softening measurements using a test specimen designed to prevent strain and damage localization. They bonding steel bars to a concrete plate and loaded the combined specimen in tension. Given sufficient steel, the concrete can uniformly degrade while the total specimen remains stable. The stress-strain softening of the concrete is obtained by subtracting the contribution of the elastic steel rods from that of the total specimen response. Having the complete stress-strain softening relation of the concrete, another test which allows strain localization would enable the determination of the materials nonlocal characteristic length (Bazant & Pijaudeir-Cabot, 1989). This technique has not been applied to laminated composites.

The most common measurement of stress-strain softening has been made via indirect correlation of a continuum model with fracture test results. Such models must employ a technique for the realistic simulation of failure localization. Section 2.2.3 identified several such techniques all of which require the experimental quantification of a characteristic length parameter which reflects the long-range nature of the failure mechanisms. Therefore, model parameters characterizing the stress-strain softening relation and the characteristic length must be varied until an optimum correlation is

achieved with test results (Ilcewicz et al., 1993, Dopker et al., 1994, DuBois, 1996, Kennedy & Nahan, 1996). This method has been referred to as the Inverse Method.

The above experimental techniques allow for the determination strain softening behavior given a continuous ever-increasing load. As presented, however, they do not enable the determination of whether strain softening is of the stiffness or the yield limit degrading types (see Figures 2.4a & b); it is also possible that both types of behavior constitute the softening behavior. The displacement controlled simple tension test could be interrupted during softening and load removed and re-applied to easily determine whether stiffness has degraded or whether permanent strain has developed. Such a technique has been performed upon concrete to show a combination of stiffness degradation and permanent strain. No application of this technique to laminated composites was identified in literature.

Direct evidence of stiffness degradation was achieved for laminated composites using results of interrupted fracture tests (Ilcewicz et al.,1993). Large notch fracture tests were performed on several fuselage skin laminate candidates in which loading was interrupted after damage initiation and prior to specimen failure. Uniaxial specimens were then cut from within and outside of the fracture process zone. Subsequent tension testing of the damaged and undamaged coupons showed that a significant reduction in stiffness had developed within the damage zone. This test was performed upon the fuselage skin laminate that is the subject of analysis in this dissertation and it, in particular, was shown to exhibit stiffness degradation.

Such experimental results do not preclude strain softening of the yield-limit degradation type. This type of softening would be identified by the development of permanent strain. In a fracture test, permanent strain would develop within the fracture process zone and be residual if the test was interrupted prior to specimen failure. Direct measurement of this residual strain using strain gages or moire interferometry could be attempted but such information is often compromised by failure of the gage bond or degradation of the surface plies. Alternatively, the permanent strain within the damage zone would act as a wedge lodged into the crack-tip such that when load was removed

the notch could not return to its original closed condition. Therefore it stands to reason that permanent strain could be indicated by failure of the notch to return to its original closed condition or if strain gages located ahead of the fracture process zone indicated residual extension. No evidence of this experimentation has been identified in literature.

A review, of broad scope, addressing damage measurement methods is available from Lemaitre & Dufailly (1987).

# 3. Laminated Plate Damage Mechanics

Damage mechanics has been employed, herein, to represent the effects of progressive degradation of laminated composite plate structure. The developed theory models plate softening resulting from in-plane and flexural load induced damage. A general discussion of damage mechanics can be found in the literature survey of Section 2. The theory models strain softening associated with stiffness degradation and assumes that strain softening of the yield-limit degradation type was insignificant. This position is supported by experimental evidence of stiffness degradation (Ilcewicz et al., 1993) and the lack of evidence, in literature, for significant permanent strain associated with the later in high-performance composite laminates.

The theory identifies damage as a second-order tensor. A second-order tensor can represent orthotropic detail whereas isotropic damage (scaler) was considered too simplistic for modeling degradation of orientated laminates. Fourth order damage entails the association of a damage components with each component of stiffness. Due to the complexity of the anisotropic plate stiffness associated with laminates, fourth order damage definition was considered unwieldy.

The mechanics of linear laminate behavior can be represented using the well known classical laminated plate theory (CLPT) (Jones, 1975). This theory was extended, herein, to incorporate second-order damage mechanics. The resultant damage effective stiffness (i.e. reduced stiffness) maintained the familiar [ABD] form associated with CLPT; however its components are embellished with 6 components of damage. Damage is always referred to the principal laminate coordinate system but the principal orientation of each damage increment follows that of the principal strain.

It was assumed that the variation of the damage through the plate thickness can be approximated as linear; this assumption is fundamental and novel. It is acknowledged that actual damage through a laminate is likely to be highly variable due to the number of damage modes possible and the assorted ply orientations and stacking sequences

available to lamination. But macroscopic representation of such complexity is not new to damage mechanics; and the suitability of this engineering approach should ultimately be judged by its ability to predict plate macro-behavior. The averaging nature of the linear damage assumption is discussed in Section 4. Plate strain, $\boldsymbol{\varepsilon}$, and damage, $\mathbf{D}$, represent material stasis within the plane of the plate. The variations of strain and damage through the thickness of the plate are approximated as linear according to

$$\boldsymbol{\varepsilon}(z) = \boldsymbol{\varepsilon}^0 + z\,\mathbf{K} \tag{3-1}$$

$$\mathbf{D}(z) = \mathbf{D}^0 + z\,\boldsymbol{\alpha} \tag{3-2}$$

In equation (3-1), second-order tensors $\boldsymbol{\varepsilon}^o$ and $\mathbf{K}$ represent mid-plane strain and curvature respectively. Likewise, second-order tensors $\mathbf{D}^0$ and $\boldsymbol{\alpha}$ respectively represent bulk mid-plane plate damage and the bulk damage gradient in equation (3-2).

Damage, D(z), evolves from a value of zero to unity; the latter corresponds to complete failure of the material point. Limits exist, for the combination $\mathbf{D}^0$ and $\boldsymbol{\alpha}$, so as to ensure that damage at the plate surface does not violate its meaningful range of zero to unity. These limits bound the shaded area of Figure 3.1.

Damage mechanics has usually incorporated the concept of an effective stress which represents the heightened stress experienced by material between damage sites. As detailed in Section 2.2.4, however, damage mechanics can also be developed using the concept of an effective strain. Because stress is highly discontinuous through the thickness of a laminate while strain is linear, the following theory is developed using the concept of effective strain. Physically, the effective strain, $\tilde{\varepsilon}$, represent the strain of a material ligament located between damage sites. For one-dimensional conditions, the effective strain is

$$\tilde{\varepsilon} = (1 - D)\,\varepsilon \tag{3-3}$$

The classical concept of strain represents a homogenized composition of deformation due to void growth or crack face separation and stretch of material between damage sites. Representing the strain associated with material separation as $\varepsilon^d$ and recalling the concept of effective strain defined in equation (3-3), the classical strain concept can be decomposed; i.e.,

$$\varepsilon = D\varepsilon + \tilde{\varepsilon} = \varepsilon^d + \tilde{\varepsilon} \tag{3-4}$$

which will be utilized later.

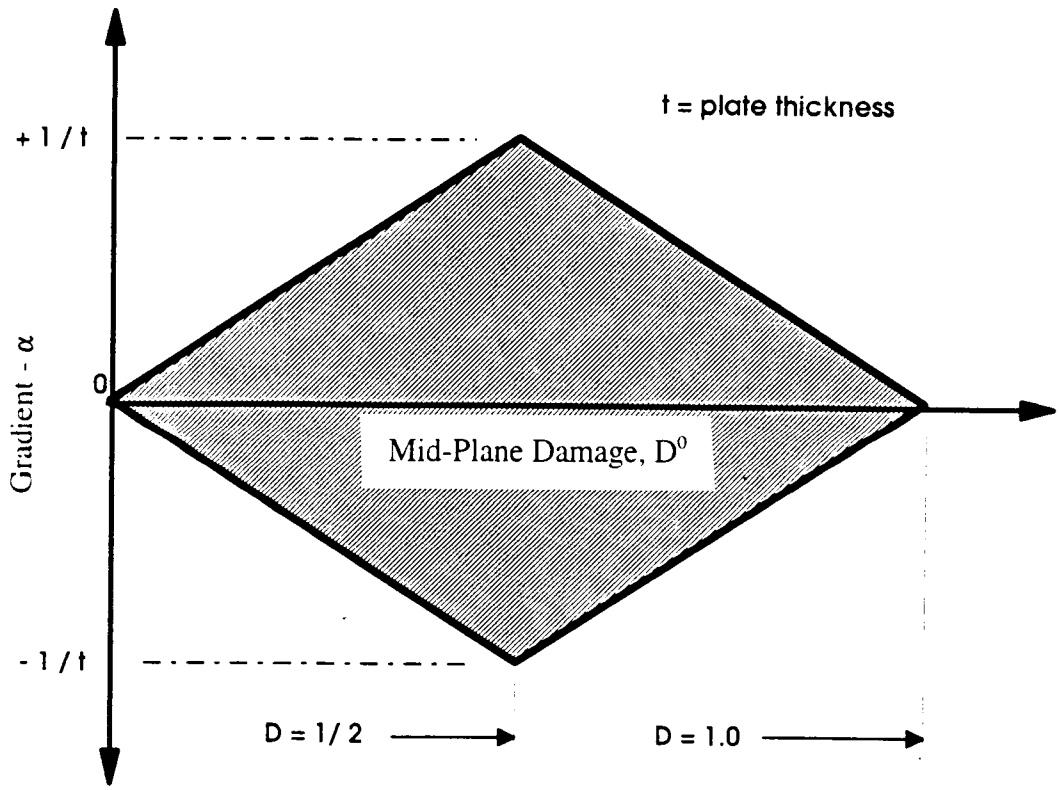


Figure 3.1 Permissible Range of Damage.

Returning to the relation of equation (3-3), the distribution of effective strain through a plate is obtained by including equations (3-1) and (3-2). The resultant effective plate strain

$$\tilde{\varepsilon}(z) = (1 - D^0)\,\varepsilon^0 + z[-\alpha\varepsilon^0 + (1 - D^0)K] + z^2[-\alpha K] \tag{3-5}$$

is of quadratic variation through the plate thickness. Equation (3-5) can be expressed in terms of effective strain components according to

$$\tilde{\varepsilon}(z) = \tilde{\varepsilon}^0 + z\,\tilde{K} + z^2\,\tilde{\varphi} \tag{3-6}$$

where:

$$\tilde{\varepsilon}^0 = (1 - D^0)\,\varepsilon^0 \tag{3-6a}$$

$$\tilde{K} = -\alpha\varepsilon^0 + (1 - D^0)K \tag{3-6b}$$

$$\tilde{\varphi} = -\alpha K \tag{3-6c}$$

It should be noted that in the absence of damage, the effective strain, as defined in equation (3-6), reduces to classical plate strain that is of linear variation through the plate thickness.

For two-dimensional plate continuum damage, equation (3-3) can be restated, in expanded matrix form (Lemaitre, 1992)

$$\begin{bmatrix} \tilde{\varepsilon}_{11}(z) & \tilde{\varepsilon}_{12}(z) \\ \tilde{\varepsilon}_{12}(z) & \tilde{\varepsilon}_{22}(z) \end{bmatrix} = \left( \begin{bmatrix} 1 & 0 \\ 0 & 1 \end{bmatrix} - \begin{bmatrix} D_{11}(z) & D_{12}(z) \\ D_{12}(z) & D_{22}(z) \end{bmatrix} \right) \begin{bmatrix} \varepsilon_{11}(z) & \varepsilon_{12}(z) \\ \varepsilon_{12}(z) & \varepsilon_{22}(z) \end{bmatrix} \tag{3-7}$$

Damage parameters are defined relative to the principal laminate basis. For load conditions in which shear strain is significant in this basis, the principal orientation of

damage is not expected to coincide with the laminate bases and damage component $D_{12}$ is therefor anticipated. A symmetric form of the damage matrix was employed in equation (3-7). This choice implies the existence of an orthogonal set of principal damage directions which is intuitively acceptable.

The substitution of plate strain, $\varepsilon_{ij}(z) = \varepsilon_{ij}^{0} + z\,K_{ij}$, and plate damage, $D_{ij}(z) = D_{ij}^{0} + z\,\alpha_{ij}$, into equation (3-7) produced an effective plate strain matrix that was not necessarily symmetric. A non-symmetric effective strain would reflect deformation associated with rigid body motion. Referral to equation (3-4) indicates that any anti-symmetric part of the effective strain would have to be negated by the anti-symmetric part of strain associated with material separation (i.e. $\varepsilon^{d} = D\varepsilon$) in order to maintain the known symmetry of classical strain. If we assume that the principal directions of classical strain and damage coincide, then the strain associated with material separation is automatically symmetric and so too must the effective strain. The theory developed herein accepts this assumption and thus requires that the effective strain be symmetric. In practice, the kinematics of damage evolution dictate whether this assumption is complied with or not. Ideally, the established damage kinetics would ensure such a compliance and the effective strain would passively maintain symmetry. However, to avoid this rigid requirement, only the symmetric part of any effective strain will be carried forward from this juncture. It is expected that the effective strain resultant from any chosen kinematic damage evolution law would not significantly deviate from the assumed coincidence of damage and classical strain. The symmetric effective strain can be established as

$$[\tilde{\varepsilon}(z)]_{sym} = [\tilde{\varepsilon}^{0}]_{sym} + z\,[\tilde{K}]_{sym} + z^{2}\,[\tilde{\varphi}]_{sym} \tag{3-8}$$

where:

$$[\tilde{\varepsilon}^{0}]_{sym} = \frac{[\tilde{\varepsilon}^{0}] + [\tilde{\varepsilon}^{0}]^{T}}{2} \tag{3-8a}$$

$$[\tilde{K}]_{sym} = \frac{[\tilde{K}] + [\tilde{K}]^{T}}{2} \tag{3-8b}$$

$$[\tilde{\varphi}]_{sym} = \frac{[\tilde{\varphi}] + [\tilde{\varphi}]^T}{2} \tag{3-8c}$$

Executing the above symmetry operation, rearranging the relation of effective strain into Voight notation and conversion from tensorial shear strain to engineering shear strain, the effective second-order strain can be restated as

$$\begin{Bmatrix} \tilde{\boldsymbol{\varepsilon}}^\circ \\ \tilde{\mathbf{K}}^\circ \\ \tilde{\varphi} \end{Bmatrix} = \begin{bmatrix} \mathbf{N}_D & 0 \\ -\mathbf{N}_\alpha & \mathbf{N}_D \\ 0 & -\mathbf{N}_\alpha \end{bmatrix} \begin{Bmatrix} \boldsymbol{\varepsilon}^\circ \\ \mathbf{K} \end{Bmatrix} \tag{3-9}$$

where

$$[N_D] = \begin{bmatrix} 1-D_{11}^0 & 0 & -D_{12}^0/2 \\ 0 & 1-D_{22}^0 & -D_{12}^0/2 \\ -D_{12}^0 & -D_{12}^0 & 1-\dfrac{\left(D_{11}^0 + D_{22}^0\right)}{2} \end{bmatrix} \tag{3-10}$$

and

$$[N_\alpha] = \begin{bmatrix} \alpha_{11} & 0 & \alpha_{12}/2 \\ 0 & \alpha_{22} & \alpha_{12}/2 \\ \alpha_{12} & \alpha_{12} & \left(\alpha_{11} + \alpha_{22}\right)/2 \end{bmatrix} \tag{3-11}$$

Classical Laminated Plate Theory, CLPT, relates plate strain to resultant plate stresses according to what has usually been referred to as the [ABD] stiffness matrix.

However, because the damage tensor has been designated by "D", the laminate bending stiffness sub-matrix will be re-designated using the letter C and the laminate stiffness matrix well be referred to as [ABC]. According to CLPT, stress is related to strain according to

$$\begin{Bmatrix} \mathbf{N} \\ \mathbf{M} \end{Bmatrix} = \begin{bmatrix} \mathbf{A} & \mathbf{B} \\ \mathbf{B} & \mathbf{C} \end{bmatrix} \begin{Bmatrix} \varepsilon^0 \\ \mathbf{K} \end{Bmatrix} \tag{3-12}$$

where **N** refers to in-plane plate force per unit length; and **M** is plate bending moment per unit length. Sub-matrices **A, B** and **C** refer to in-plane, extension-bending coupling and the bending stiffnesses respectively. If $\bar{Q}_{ij}(z)$ represents stiffness in the plane of the plate at any position through the plate thickness, and $(\bar{Q}_{ij})_k$ represents that of the k$^{th}$ ply, then stiffnesses can be formulated (Jones, 1974) as

$$A_{ij} = \int_{-t/2}^{+t/2} [\bar{Q}_{ij}(z)]dz = \sum_{k=1}^{n} \left(\bar{Q}_{ij}\right)_k \left(z_k - z_{k-1}\right) \tag{3-13a}$$

$$B_{ij} = \int_{-t/2}^{+t/2} [\bar{Q}_{ij}(z)]\, z\, dz = \frac{1}{2}\sum_{k=1}^{n} \left(\bar{Q}_{ij}\right)_k \left(z_k^2 - z_{k-1}^2\right) \tag{3-13b}$$

$$C_{ij} = \int_{-t/2}^{+t/2} [\bar{Q}_{ij}(z)]\, z^2\, dz = \frac{1}{3}\sum_{k=1}^{n} \left(\bar{Q}_{ij}\right)_k \left(z_k^3 - z_{k-1}^3\right) \tag{3-13c}$$

If quadratic strain and complementary quadratic stress resultant terms are considered, an extension of CLPT would relate the stress to strain according to

$$\begin{Bmatrix} \mathbf{N} \\ \mathbf{M} \\ \mathbf{L} \end{Bmatrix} = \begin{bmatrix} \mathbf{A} & \mathbf{B} & \mathbf{C} \\ \mathbf{B} & \mathbf{C} & \mathbf{E} \\ \mathbf{C} & \mathbf{E} & \mathbf{F} \end{bmatrix} \begin{Bmatrix} \varepsilon^0 \\ \mathbf{K} \\ \phi \end{Bmatrix} \tag{3-14}$$

The quadratic strain component, $\varphi$, is absent from plate theory because experimental measurements support the assumption that this term is negligible for linear elastic material behavior. Quadratic strain implies a quadratic deformation profile through the plate thickness. The quadratic resultant load term, **L**, is the second moment of stress through the plate thickness per unit length. **L** exists in a general laminated plate irregardless of whether the plate displacement profile is assumed linear or quadratic. To date, this term has been of little practical importance. Stiffnesses **E** and **F** are derived in a manner like that of stiffnesses **A, B** and **C** of equations (3-13a,b,c). Stiffnesses **E** and **F** are therefore

$$E_{ij} = \int_{-t/2}^{+t/2} [\bar{Q}_{ij}(z)]\, z^3\, dz = \frac{1}{4}\sum_{k=1}^{n} \left(\bar{Q}_{ij}\right)_k \left(Z_k^4 - Z_{k-1}^4\right) \tag{3-15a}$$

$$F_{ij} = \int_{-t/2}^{+t/2} [\bar{Q}_{ij}(z)]\, z^4\, dz = \frac{1}{5}\sum_{k=1}^{n} \left(\bar{Q}_{ij}\right)_k \left(Z_k^5 - Z_{k-1}^5\right) \tag{3-15b}$$

The effective laminate stiffness can be formulated using the elastic energy equivalence hypotheses (Cordebois & Sidoroff, 1979) summarized in equation (2-9). This hypothesis states that the elastic strain energy of the damaged material is the same in form as that of an undamaged material except that the stresses or strains are replaced by their effective counterparts. For an anisotropic laminate, this hypothesis is formulated as

$$\frac{1}{2}\begin{Bmatrix} \tilde{\varepsilon}^\circ \\ \tilde{\mathbf{K}}^\circ \\ \tilde{\varphi} \end{Bmatrix}^T \begin{bmatrix} \boldsymbol{A} & \boldsymbol{B} & \boldsymbol{C} \\ \boldsymbol{B} & \boldsymbol{C} & \boldsymbol{E} \\ \boldsymbol{C} & \boldsymbol{E} & \boldsymbol{F} \end{bmatrix} \begin{Bmatrix} \tilde{\varepsilon}^\circ \\ \tilde{\mathbf{K}}^\circ \\ \tilde{\varphi} \end{Bmatrix} = \frac{1}{2}\begin{Bmatrix} \varepsilon^\circ \\ \mathbf{K} \end{Bmatrix}^T \begin{bmatrix} \tilde{\boldsymbol{A}} & \tilde{\boldsymbol{B}} \\ \tilde{\boldsymbol{B}} & \tilde{\boldsymbol{C}} \end{bmatrix} \begin{Bmatrix} \varepsilon^\circ \\ \mathbf{K} \end{Bmatrix} \tag{3-16}$$

The effective stiffness matrix, $[\tilde{A}\tilde{B}\tilde{C}]$, represents the damage reduced laminate stiffness. Substitution of equation (3-9) into equation (3-16) enables the definition of this effective stiffness

$$\begin{bmatrix} \tilde{\mathbf{A}} & \tilde{\mathbf{B}} \\ \tilde{\mathbf{B}} & \tilde{\mathbf{C}} \end{bmatrix} = \begin{bmatrix} \mathbf{N}_D & -0 \\ -\mathbf{N}_\alpha & \mathbf{N}_D \\ 0 & -\mathbf{N}_\alpha \end{bmatrix}^T \begin{bmatrix} \mathbf{A} & \mathbf{B} & \mathbf{C} \\ \mathbf{B} & \mathbf{C} & \mathbf{E} \\ \mathbf{C} & \mathbf{E} & \mathbf{F} \end{bmatrix} \begin{bmatrix} \mathbf{N}_D & 0 \\ -\mathbf{N}_\alpha & \mathbf{N}_D \\ 0 & -\mathbf{N}_\alpha \end{bmatrix} \tag{3-17}$$

Individual sub-matrices of $[\tilde{A}\tilde{B}\tilde{C}]$ can be expanded according to equation (3-18) in which it is apparent that the development of damage brings the quadratic stiffness terms, $E_{ij}$ and $F_{ij}$, into play.

$$\tilde{\mathbf{A}} = \mathbf{N}_D^T : \mathbf{A} : \mathbf{N}_D - 2\mathbf{N}_D^T : \mathbf{B} : \mathbf{N}_\alpha + \mathbf{N}_\alpha^T : \mathbf{C} : \mathbf{N}_\alpha \tag{3-18a}$$

$$\tilde{\mathbf{B}} = \mathbf{N}_D^T : \mathbf{B} : \mathbf{N}_D - 2\mathbf{N}_D^T : \mathbf{C} : \mathbf{N}_\alpha + \mathbf{N}_\alpha^T : \mathbf{E} : \mathbf{N}_\alpha \tag{3-18b}$$

$$\tilde{\mathbf{C}} = \mathbf{N}_D^T : \mathbf{C} : \mathbf{N}_D - 2\mathbf{N}_D^T : \mathbf{E} : \mathbf{N}_\alpha + \mathbf{N}_\alpha^T : \mathbf{F} : \mathbf{N}_\alpha \tag{3-18c}$$

Expansion of the effective stiffness sub-matrices, equations (3-18a,b & c), can be found in Appendix A for a symmetric ($B_{ij} = E_{ij} = 0$) and balanced laminate influenced by a general case of damage.

To appreciate the influence of damage on laminate stiffness, consider the case in which the principal damage basis is coincident with that of the laminate (i.e., $D_{12} = \alpha_{12} = 0$.). For this condition cracks can be conceptualized to developed in orientations normal to the principal laminate directions. Considering damage in the primary laminate directions, a few significant components of the effective laminate stiffness are

$$\tilde{A}_{11} = A_{11}\left(1 - D_{11}^O\right)^2 + C_{11}\alpha_{11}^2 \tag{3-19a}$$

$$\tilde{B}_{11} = -2C_{11}\left(1 - D_{11}^O\right)\alpha_{11} \tag{3-19b}$$

$$\tilde{C}_{11} = C_{11}\left(1 - D_{11}^O\right)^2 + F_{11}\alpha_{11}^2 \tag{3-19c}$$

To verify the above relations, consider the following thru-thickness variation of the effective laminate in-plane stiffness due to the assumed uniaxial damage condition.

$$\tilde{Q}_{11}(z) = [Q_{11}(z)]\left(1 - D_{11}(z)\right)^2 = [Q_{11}(z)]\left(1 - D_{11}^{o} - z\,\alpha_{11}\right)^2 \qquad (3\text{-}20)$$

Equation (3-20) can be integrated through the thickness of the plate, as directed in equations (3-13a,b & c), to verify the relations of equations (3-19a,b & c).

To further appreciate the influence of damage on the laminate stiffness, the relations of equation (3-19a,b & c) were non-dimensionalized and plotted in Figures 3.2 through 3.4. The diamond pattern, within the plots, corresponds to the permissible range of the damage shown in Figure 3.1. Variation of the in-plane and bending stiffnesses, shown in these figures, demonstrate that the mid-plane damage term, $D^o$, is much more dominant than the damage gradient term, $\alpha$. This result was expected since these stiffnesses represent even variations of stiffness about the plate mid-plane whereas the damage gradient terms represents the influence of an odd stiffness variation.

Prior to damage, the extension-bending coupling stiffness component $B_{11}$ does not exist for a symmetric laminate. However, should a damage gradient develop, so too would a damage effective stiffness $\tilde{B}_{11}$ according to equation (3-19). A physical appreciation for this damage effect can be had by comparing it to the $B_{11}$ stiffness for the same plate with one half of the laminate removed and the other half in perfect condition. Application of tension to the plate centroid would generate curvature according to a extension-bending coupling stiffness that will be referred to herein as $B_{11}^{HP}$. Figure 3.3 is a plot of the damage effective extension-bending interaction stiffness term $\tilde{B}_{11}$ normalized with respect to $B_{11}^{HP}$ of the half-plate case. As expected, both the mid-plane damage and damage gradient terms exhibit strong influence upon $\tilde{B}_{11}$. Within the range of permissible damage coordinates, the maximum effective interaction component, $\tilde{B}_{11}$, was ⅔ that of the half-plate case. Considering the extreme asymmetry of the half-plate case, the potential influence of damage on the development of extension-bending interaction is significant.

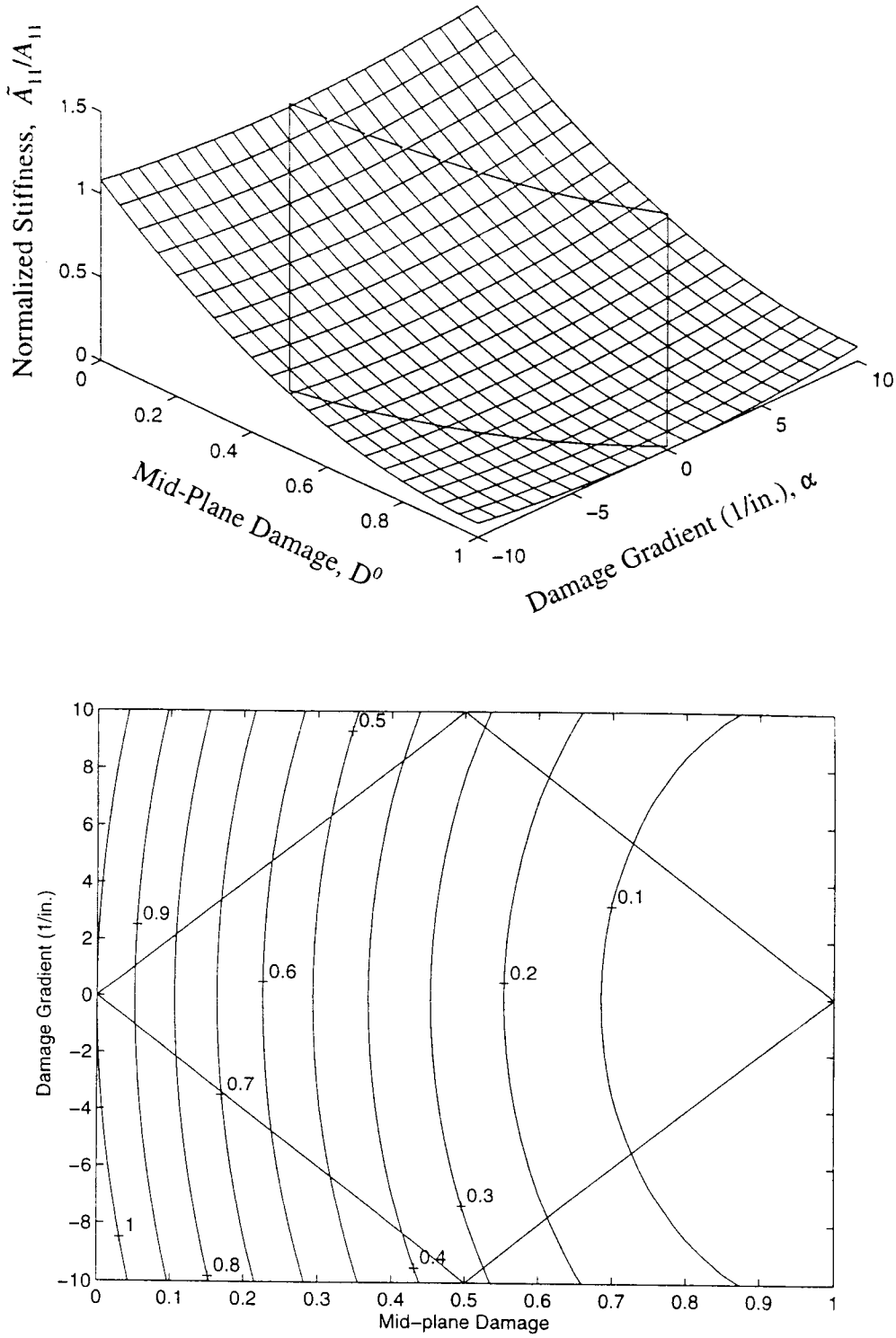


Figure 3.2 Normalize Effective In-plane Stiffness $\tilde{A}_{11} / A_{11}$ versus Damage.

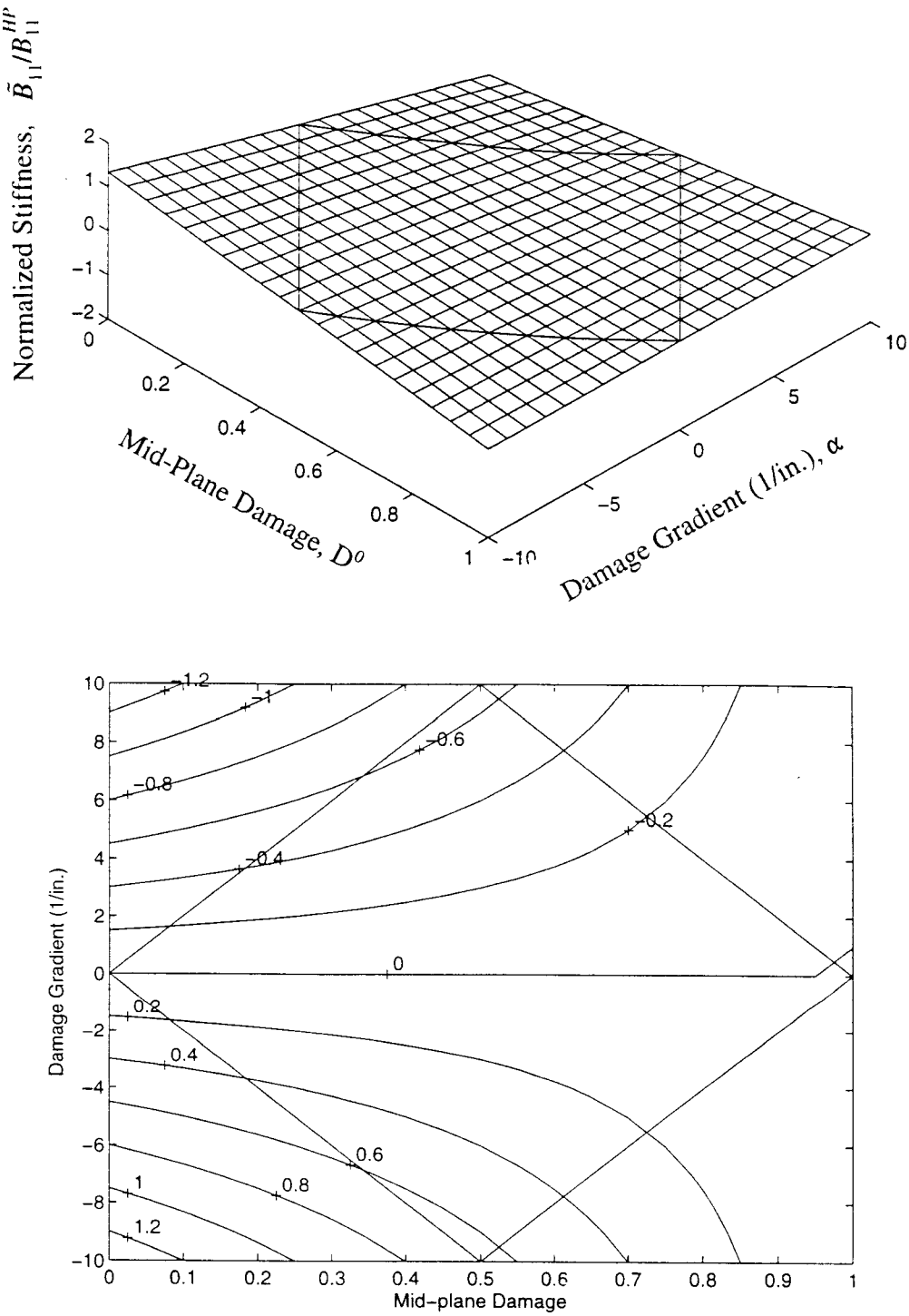


Figure 3.3 Normalize Effective Extension-Bending Coupling Stiffness $\tilde{B}_{11} / B_{11}^{HP}$ versus Damage.

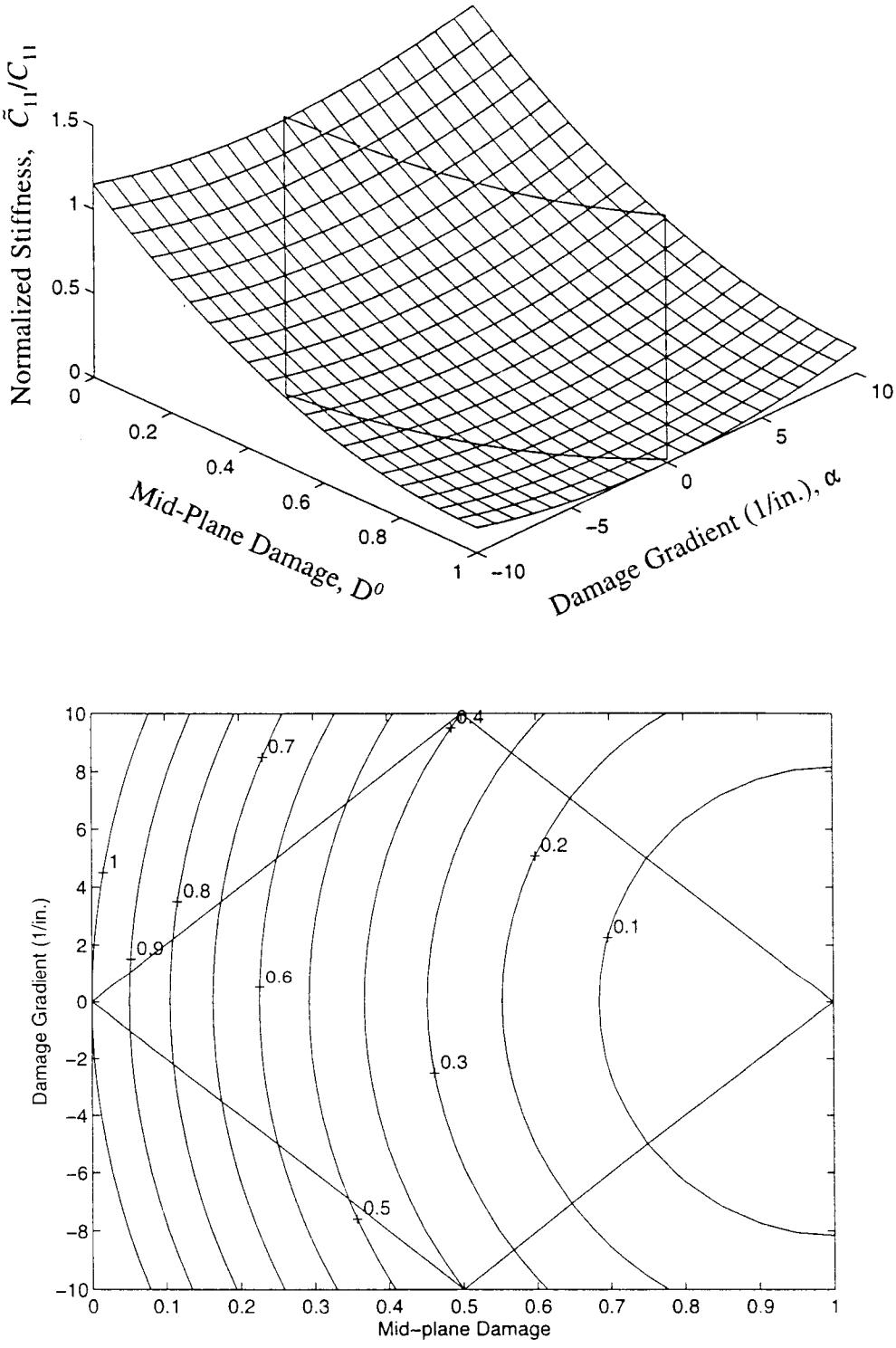


Figure 3.4 Normalize Effective Bending Stiffness $\tilde{C}_{11} / C_{11}$ versus Damage.

The components of effective stiffness, for a general damage condition, are too complex to illustrate (see Appendix A). Additionally, the various components of damage should evolve in a concerted manner according to a user chosen damage kinematics model. Such a model may limit the permutations of damage. The subject of damage kinematics is addressed in the following section.

# 4. Plate Damage Kinetics

Damage kinetics must be proposed for governing the growth of damage. Unlike the principled development of damage mechanics, significant creative freedom is commonly exercised in the development of damage growth kinetics. This creative license is warranted due to the lack of experimental guidance and lack of scientific consensus on the physical operatives influencing damage. Two basic methods exist to define the kinetics of damage evolution. The theory developed herein chose to employ nonlocal strain as the force behind damage growth; the concept of nonlocal strain is developed below. This theory proposes simple uniaxial damage growth functions depending on the dominant strain condition within the principal laminate basis. Alternatively the thermodynamics of dissipative materials could have been employed to identify the damage force and establish a rational orchestration for the relative evolution of the damage tensor. Of these two methods, the uniaxial criterion is more straight forward in implementation and possibly more intuitively transparent. While the thermodynamic approach is rigorous in its physical foundation, it is still very much a product of the researcher's creative influences. A discussion of damage kinetics and methods practiced can be found in the literature review of Section 2.

Strain was chosen as the force behind damage growth because not only can an intuitive association be made between strain and material cracking (i.e. damage), but as discussed in Section 3, the principal direction of damage and strain should coincide in order to ensure symmetry of the effective strain matrix. This condition of coincidence can best be ensured by defining the evolution of damage with respect to strain. The intuitive argument could also be made for using the resultant plate stresses as the force behind damage; but for a generally anisotropic laminate, the condition of coincidence could not be ensured using such a definition. Also, the variation of strain through the thickness of a composite plate is of a continuous linear variation whereas stress is highly discontinuous. Thus strain can serve as a more straight-forward, intuitively transparent,

cause of macroscopic damage. Finally, employing strain as the damage force allows for the resultant progressive damage theory to serve as a direct extension of laminate failure criteria such as the maximum strain, Tsai-Hill or Tsai-Wu criteria expressed in terms of strain (Jones, 1975).

A simple damage growth scheme is proposed in the following sections that is akin to the maximum strain failure criterion (Jones, 1975) and based upon the nonlocal form of mid-plane strain and curvature. The scheme includes a two criteria, one is activated if shear is insignificant within the principal laminate basis. For this case, the principal damage basis is coincident with that of the laminate. The other criterion represents shear dominate loading; and as such, damage is assumed to grow according to pure shear conditions. This scheme does not guarantee the coincidence of the principal damage and strain but does maintain an approximate alignment. As discussed in Section 3, the effective plate stiffness, equation (3-17), was based upon the symmetric part of the damage effective strain in order to support the freedom just exercised. The above simple damage growth scheme is developed below in two stages. Section 4.2 is limited to conditions void of curvature. Section 4.3 represents an extension to conditions of combined extension plus curvature.

Conventional numerical analysis of strain softening materials encounters the problem of progressive failure localization to a material volume of vanishing size. Such failure progresses with zero energy dissipation, a result which is physically unrealistic. The fundamental problem has been identified to be the loss of ellipticity of the incremental equilibrium equations and bifurcation between material paths of continued homogeneity versus inhomogeneity associated with softening and unloading regimes (Rice, 1977). This issue and several remedies are discussed in the literature review of Section 2. Of the known remedies, the nonlocal approach was chosen for support of the theory developed herein. Specifically, strain, in its role as the force behind damage growth, was treated by the nonlocal method (Pijaudiier-Cabot & Bazant, 1987). In all other respects, material state variables such as strain and stress are treated as local.

## 4.1 Nonlocal Strain

All kinematic relations, developed in this section, refer to the nonlocal form of strain as designated by a bar cap (i.e. $\bar{\varepsilon}$). This designation should not be confused with the tilde designation given to the effective strain developed in the section 3. Nonlocal mid-plane plate strain can be defined (Pijaudier-Cabot & Bazant, 1987, Bazant & Cedolin, 1991, Kennedy & Nahan, 1996) as

$$\bar{\varepsilon}^{0}_{ij}(x,y) = \frac{1}{A_r(x,y)} \iint_A \omega(\xi - x, \eta - y, l_{ch})\, \varepsilon^{0}_{ij}(\xi,\eta)\, d\xi\, d\eta \qquad (4\text{-}1)$$

which integrates classical plate strain over a two-dimensional range, as illustrate in Figure 4.1, to obtain the nonlocal strain for all material focal points of location (x,y).

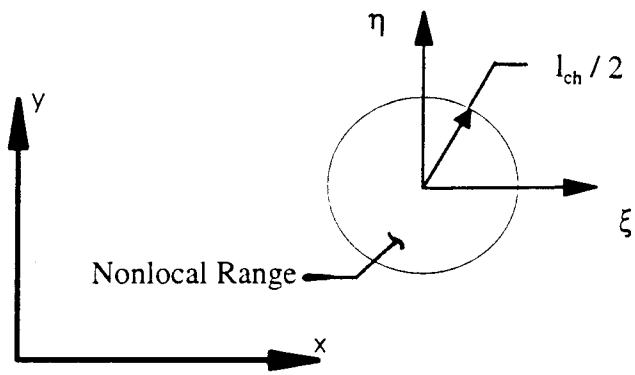


Figure 4.1 Nonlocal Range for Each Material Point.

The function $\omega(\xi\text{-}x, \eta\text{-}y, l_{ch})$ defines the weight or influence that a distant material point $(\xi,\eta)$ has in contributing to the nonlocal strain of the material focal point (x,y). The characteristic length parameter, $l_{ch}$, establishes the range size and is

considered a material property. Function $\omega(\xi\text{-}x, \eta\text{-}y, l_{ch})$ could simply represent a constant weighting applicable to a range of finite size defined by the characteristic length $l_{ch}$. However, a smooth variation of weight from the region of influence to that of none, has been shown to improve solution convergence in numerical analysis (Bazant & Cedolin, 1991). The nonlocal range could be of any shape but a circular range is assumed which suggests isotropy of directional influence. A more complex nonlocal range configuration, such as elliptical, would require experimental determination of additional parameters. The weight function chosen for the analysis herein is of a smooth bell-shape form, as suggested by Bazant & Cedolin (1991), and defined as

$$\omega(\xi - x, \eta - y) = \left\{ 1 - \left[ \frac{(\xi - x)^2 + (\eta - y)^2}{(0.9086 * l_{ch})^2} \right] \right\}^2 \qquad (4\text{-}2)$$

The profile of this weight function is illustrated in Figure 4.2. The term $0.9086 * l_{ch}$ in the denominator of equation (4-2) represents the maximum radius of the smooth nonlocal range. Its value was identified by forcing the total integrated weight of equation (4-2) to equal to that of a unit weight function (i.e., $\omega = 1$) integrated over a circular nonlocal range of diameter $l_{ch}$.

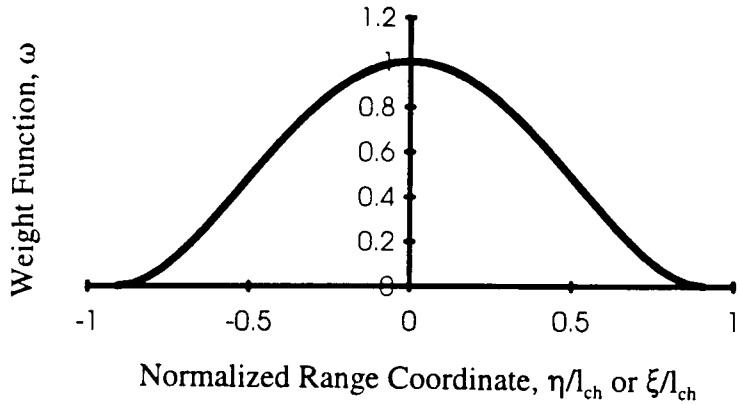


Figure 4.2 Profile of Nonlocal Weight Function.

Function $A_r(x,y)$ equals the total integrated weight; i.e.,

$$A_r(x,y) = \iint_A \omega(\xi - x, \eta - y)\, d\xi\, d\eta \tag{4-3}$$

used to normalize the nonlocal integration of equation (4-1). As mentioned above, the total weight of equation (4-2) is equal to that of the unit weight function over an circular area of diameter $l_{ch}$. Therefore $A_r$ of equation (4-3) is equal to $\pi(l_{ch}/2)^2$ so long as the full nonlocal range is contained by the plate structure of interest.

Finally, nonlocal curvature $\bar{K}_{ij}$ was defined in the same manner as that defined above. It was assumed that the same characteristic length would apply to both nonlocal mid-plane strain and curvature.

## 4.2 Simple Damage Kinetics for Non-flexural Conditions

The damage kinetics developed in this section assumes that curvature effects are insignificant, and as such no damage gradient evolves. Such conditions include the common case of in-plane loading of symmetric laminate. Extension to conditions of significant curvature is made in Section 4.3. Unless otherwise stated, the following sections 4.2 and 4.3 always refer to the nonlocal treatment of strain and refer to the principal laminate basis.

The following simple damage growth scheme includes a shear strain criterion and a set of criteria corresponding to principal strain aligned with principal laminate basis. This later set will be developed below followed by the shear strain criterion. These criteria are exclusive of each other in that either shear governs damage growth or the extensional strain in the principal laminate directions do. As such, either the nonlocal shear strain or the diagonal strain component act as the force behind damage growth.

For conditions of insignificant shear, the diagonal components of mid-plane damage are made dependent upon their respective counterparts of nonlocal strain

$$D_{11}^{0} = f_1\left(\bar{\varepsilon}_{11}^{0}\right) \tag{4-4a}$$

$$D_{22}^{0} = f_2\left(\bar{\varepsilon}_{22}^{0}\right). \tag{4-4b}$$

Although a specific definition of these functions is not necessary for the development of the following damage kinetics, a specific functional form is presented as follows to assist concept clarity. It is also the form utilized later for experimental damage characterization of laminates. The specific form of the mid-plane damage growth function utilized in this analysis is shown in Figure 4.3.

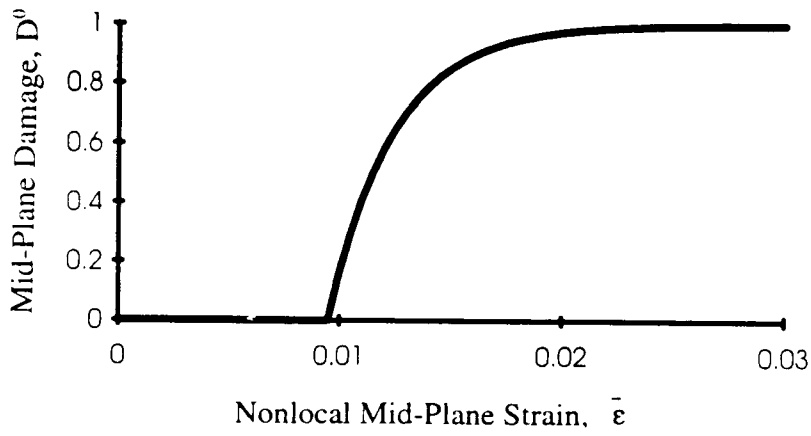


Figure 4.3 Uniaxial Damage Growth Function.

This function assumes that no damage develops below a strain corresponding to failure in a uniaxial stress test. The damage would then evolve from a value of zero to unity, the later of which represents total laminate degradation and failure.

The uniaxial damage growth functions, $f_1$ and $f_2$, are assumed independent and were represented herein by the exponential relation

$$D_{ii}^{0} = 0 \qquad \text{for: } \bar{\varepsilon}_{ii}^{0} < \varepsilon_{ii}^{cr} \tag{4-5a}$$

$$D_{ii}^{0} = f_i\left(\bar{\varepsilon}_{ii}^{0}\right) = 1 - \left[\frac{\varepsilon_{ii}^{cr}}{\bar{\varepsilon}_{ii}^{0}} e^{-a_i\left(\bar{\varepsilon}_{ii}^{0} - \varepsilon_{ii}^{cr}\right)}\right]^{1/2} \qquad \text{for: } \bar{\varepsilon}_{ii}^{0} \geq \varepsilon_{ii}^{cr} \tag{4-5b}$$

the form of which is represented in Figure 4.3. In equation (4-5), subscript "i" refers to the major or minor principal laminate direction 1 or 2; no tensor component summation is intended in the relations. The term $\varepsilon_{ii}^{cr}$ refers to the critical uniaxial failure strain. Constant "$a_i$" is the sole parameter governing the rate of damage accumulation in equation (4-5) and is considered a material property. Many forms of the damage growth function have been presented in the literature. No attempt is made herein to determine the best functional form. Equation (4-5) is a single parameter function which simplified the search for optimal material damage characterization.

Substitution of equation (4-5) into the effective in-plane stiffness relation of equation (3-19a) and simplification to a plate condition of initial isotropy results in the stress-strain softening behavior

$$\sigma_{11} = \frac{E}{1 - \nu^2} \varepsilon_{11}^{0} \qquad \text{for: } \bar{\varepsilon}_{ii}^{0} < \varepsilon_{ii}^{cr} \tag{4-6a}$$

$$\sigma_{11} = \frac{E}{1 - \nu^2} (1 - f_1(\bar{\varepsilon}_{11}^{0}))^2 \bar{\varepsilon}_{11}^{0} = \frac{E}{1 - \nu^2} \varepsilon_{11}^{cr} e^{-a_1\left(\bar{\varepsilon}_{11}^{0} - \epsilon_{11}^{cr}\right)} \qquad \text{for: } \bar{\varepsilon}_{ii}^{0} \geq \varepsilon_{ii}^{cr} \tag{4-6b}$$

which is plotted in Figure 4.4 for three examples of the damage accumulation parameter $a_{ii}$. The inverse of the above conversion would also be possible; that is, given the stress-strain softening function, the damage-strain relation could be determined.

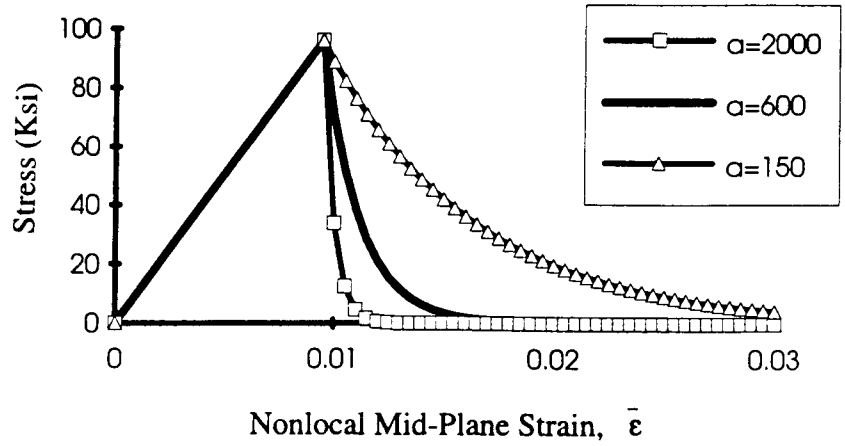


Figure 4.4 Example Stress-Strain Softening Behavior.

For conditions in which shear is dominant, damage is assumed to evolve according to a state of pure shear deformation. Pure shear strain in the principal laminate basis can be resolved by a 45 degree coordinate axis rotation to its principal bi-axial strain basis. As shown in Figure 4.5, the sign of the shear strain determines which of the principal strain components is tensile and which is compressive.

With respect to the principal strain basis of the pure shear condition, only that component of damage coincident with the tensile strain is assumed to evolve. Note that the condition of coincidence between principal damage and pure shear strain principal basis is upheld. Being a second order tensor, the above uniaxial damage can easily be transformed back to the principal laminate basis according to the transformation law

$$[D^0]_{1,2} = [Q]^T [D^0]_{x,y} [Q] \tag{4-7}$$

in which Q represents the orthogonal rotation tensor whose matrix components correspond to directional cosines relating the two axis systems (Lai et al., 1978).

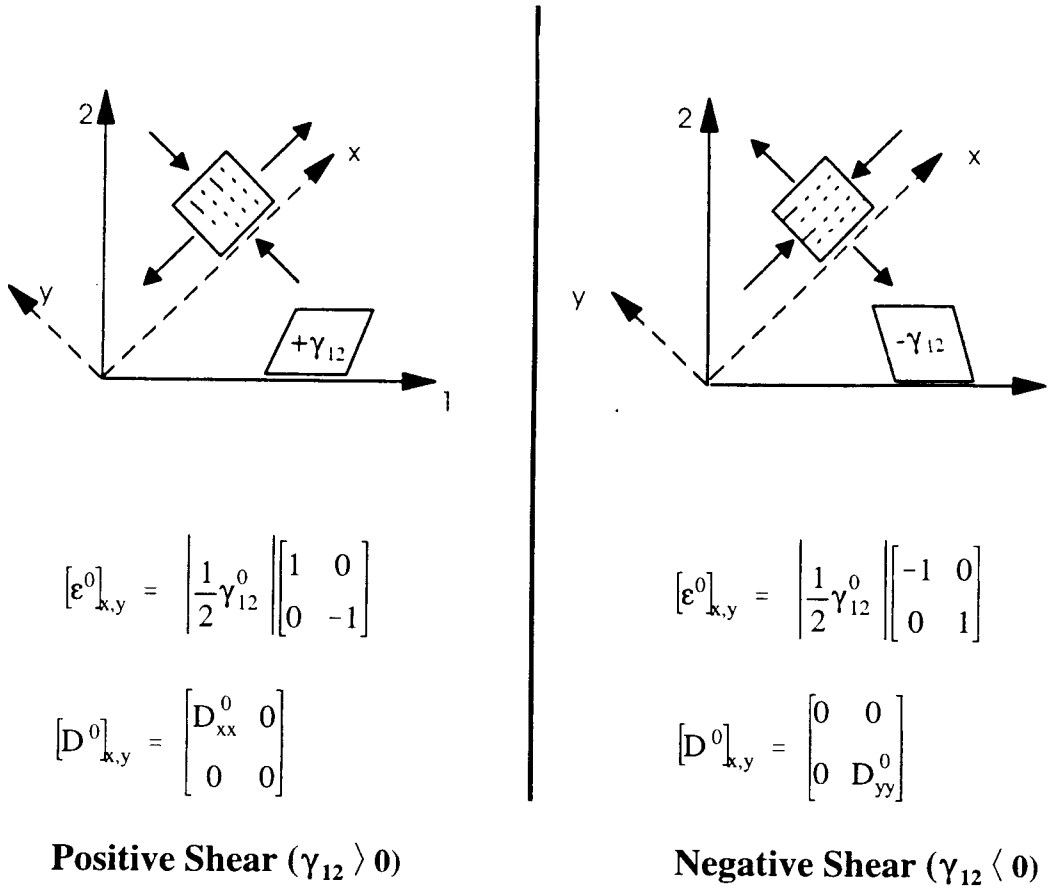


Figure 4.5 Principal Strain and Proposed Damage for Pure Shear Condition.

For positive shear strain, transformation of the induced uniaxial damage to the principle laminate basis results in the matrix

$$[D^0]_{1,2} = \tfrac{1}{2} D^0_{xx}\begin{bmatrix}1 & 1\\ 1 & 1\end{bmatrix} \tag{4-8a}$$

For negative shear strain, the corresponding transformed damage is

$$[D^0]_{1,2} = \tfrac{1}{2} D^0_{yy}\begin{bmatrix}1 & -1\\ -1 & 1\end{bmatrix} \tag{4-8b}$$

Obviously all transformed terms are of equal absolute value and are assumed to evolve uniformly relative to the nonlocal shear strain. A single growth function for the uniaxial damage component can be constructed relative to the nonlocal laminate shear strain. A check on the sign of the shear strain enables the appropriate transformation to equations (4-8a) or (4-8b). The kinetics of shear based damage have thus been established. The function

$$D_{xx}^{0} = f_3\left(\bar{\gamma}_{12}^{0}\right) = 1 - \left[\frac{\gamma_{12}^{cr}}{\bar{\gamma}_{12}^{0}} e^{-a_{12}\left(\bar{\gamma}_{12}^{0} - \gamma_{12}^{cr}\right)}\right]^{1/2} \tag{4-9}$$

was chosen for this analysis, to represent damage evolution under conditions of positive shear. The same function, $f_3$, and associated parameters would apply to negative shear induce damage, $D_{yy}^{0}$. Consistent with the definition of damage functions $f_1$ and $f_2$ of equation (4-5), equation (4-9) employed the critical pure shear failure strain, $\gamma_{12}^{cr}$ , and a unique damage accumulation parameter $a_{12}$ that serves as a material property.

Input of either equation (4-8a) or (4-8b) into the effective in-plane shear stiffness component $\tilde{A}_{66}$, detailed in Appendix A, results in the same relation; that is

$$\tilde{A}_{66} = A_{66}\left\{\frac{(1+\nu)}{(1-\nu)}(D_{xx}^{0})^2/4 + (2 - D_{xx}^{0})^2/4\right\} \tag{4-10}$$

According to equation (4-10) the effective shear stiffness evolves from the nominal (no damage) value to a third of this value corresponding to complete shear induced damage. From pure shear tests, ultimate specimen failure would indicate that the effective shear stiffness should eventually vanish. The resultant finite value of the derived effective shear stiffness represents a material saturated with cracks of + or -45 degree orientation (depending on the sign of imposed shear). Assuming infinitesimal strain and linear material behavior, such a medium would exhibit considerable shear stiffness in the 0/90 degree basis (Jones, 1975). Thus the above realized residual of effective stiffness is a

product of the proposed model of damage kinetics under pure shear conditions and not a result of the derived relation for the damage effective stiffness, equation (3-18).

For the shear stiffness to vanish, a state of isotropic damage must evolve. Considering the biaxial compressive plus tensile nature of the principal strain associated with pure shear conditions shown in Figure 4.5, the compressive strain component would be required to induce damage equal that of the tensile component. It is possible that the compressive component of strain could induce softening of a compressive instability nature. However, the theory developed herein has assumed only fracture or void induced softening which is less probable under compressive loading. Therefore, instead of imposing isotropic damage kinetics on the pure shear strain condition, the proposed uniaxial damage model was put forward as being true to the intent of damage mechanics. Its lack of complete stiffness degradation is noted and further study is encouraged to resolve the issue.

Both extensional damage modes, characterized by equations (4-4a & b), can develop independently without conflict. However according to equation (4-8), the uniaxial shear damage is represented by the same damage components as that of the extensional mode. Thus conflict arises over control of such damage components should both damage modes realize their threshold strain values. Although such conditions were not realized in the simulations reported upon herein, the following protocol is proposed for completeness. Should the shear threshold strain be realized first, it should maintain control of the damage components, for that material point, for the duration of the simulation. Otherwise, the two extensional damage modes (equations (4-4a & b)) should exercise complete control of the mid-plane damage components. This protocol locks in place whichever damage mode is registered first. Neighboring material points can be controlled by different damage modes. Such a protocol is offered for its simplicity and is recognized as being far from complete.

## 4.3 Damage Kinetics for Conditions of Combined Extension + Curvature

Considering the novelty of the proposed linear plate damage function, $D(z) = D^0 + z\,\alpha$, and the uncharted waters of damage induced by curvature, a rigorous functional development of the kinetics of such damage is justified. For non-curvature condition, the damage growth shown in Figure 4.3 was assumed with considerable confidence due to the large body of literature applied to strain softening under in-plane load conditions. No such wealth of experience is available for damage growth under conditions of plate curvature.

In laminated plate, damage resistance is expected to vary from ply to ply through the thickness. A general functional relation between uniaxial damage and strain can be formulated as

$$D(z) = g(z, \varepsilon(z)) \tag{4-11}$$

The coordinate z appears explicitly in equation (4-11) to account for the variability of the damage - strain relation from layer to layer. Strain $\varepsilon(z)$ is included in equation (4-11) because it has been established as the basic force behind damage growth. It is expected that actual damage would be highly variable or even erratic through the plate thickness. The damage model developed herein, however, assumed a simple linear variation of damage (equation (3-2)). Therefore the linear damage parameters $D^0$ and $\alpha$ must represent the best linear fit of what actually transpires. Thus, mid-plane damage, $D^0$, was defined as

$$D^0 = \frac{1}{t} \int_{-t/2}^{+t/2} g(z, \varepsilon(z))\, dz \tag{4-12}$$

representing the average value of damage through the plate thickness.

Similarly, the damage gradient parameter, $\alpha$, was defined as

$$\alpha = \frac{1}{t}\int_{-t/2}^{+t/2}\left[\frac{dg(z,\varepsilon(z))}{dz}\right]dz \tag{4-13}$$

representing the average derivative of damage with respect to position through the plate thickness. Being defined as averaged values, such parameters would be considered representative of the bulk laminate. The damage gradient can be expanded to reveal a dependency upon curvature, K.

$$\alpha = \frac{1}{t}\int_{-t/2}^{+t/2}\left[\frac{\partial g(z,\varepsilon(z))}{\partial z} + \frac{\partial g(z,\varepsilon(z))}{\partial \varepsilon(z)}\cdot K\right]dz \tag{4-14}$$

If $g(z,\varepsilon(z))$ were defined according to a general family of functions, then the functional relationships between the bulk damage coefficients and plate strain could be established. The general damage function, $g(z,\varepsilon(z))$, can be expanded in a power series fashion. To maintain complete generality, an infinite number of series terms would be required. Instead, a limited number of terms are proposed

$$g(z,\varepsilon(z)) = a + b\cdot\varepsilon(z) + c\cdot(\varepsilon(z))^2 + d\cdot(\varepsilon(z))^3 \tag{4-15}$$

where coefficients a, b & c are quadratic in z; i.e. $a = a_0 + a_1 z + a_2 z^2$, $b = b_0 + b_1 z + b_2 z^2$, $c = c_0 + c_1 z + c_2 z^2$. For simplicity, the coefficient d is made constant; i.e. $d = d_0$. Although equation (4-15) represents a limited functional family, the inclusion of higher powered terms were found to generate terms of higher order products of curvature and strain which were not necessary for identifying a basic functional form. In rationalizing the possible variations of damage, no damage should exist under zero strain conditions; therefore coefficient a(z) must be zero for all values of z (i.e. $a_0 = a_1 = a_2 = 0$). For symmetric laminates, damage resistance should also be symmetric, and thus coefficients $b_1$ and $c_1$ must be zero.

Substituting equation (4-15) into equation (4-12) yields the relation of equation (4-16) as the bulk mid-plane damage parameter.

$$D^0 = \left( b_0 + b_2 \frac{t^2}{12} \right) \varepsilon^0 + \left( c_0 + c_2 \frac{t^2}{12} \right) (\varepsilon^0)^2 + d_0 (\varepsilon^0)^3 + \left( c_0 \frac{t^2}{12} + c_2 \frac{t^4}{80} \right) K^2 + \left( d_0 \frac{t^2}{12} \right) 3\varepsilon^0 K^2 \tag{4-16}$$

The first three terms of equation (4-16) represent mid-plane damage in the absence of curvature and thus can be replace by a general functional relation developed in the previous section (Section 4.2) and generally expressed as $D^0 = f(\varepsilon^0)$. The remaining terms are common in their relation to the square of curvature. Had higher order terms been included in equation (4-15), additional higher even powers of curvature would have appeared in equation (4-16). Equation (4-16) can therefore be simplified as

$$D^0 = f(\varepsilon^0) + \sum h_i(\varepsilon^0) K^{2i} \tag{4-17}$$

The apparent dependence of mid-plane damage, $D^0$, on curvature, K, makes physical sense considering that even for mid-plane strain below the damage threshold value, $\varepsilon_{ii}^{cr}$, the presence of curvature could increase tensile strain in one-half of the plate thickness to levels sufficient to cause damage. Such a lop-sided damage profile would contribute to the averaged sense of the mid-plane damage.

For purposes of analysis, a specific functional form is proposed as shown in Figure 4.6 for characterizing mid-plane damage growth due to conditions of combined tension plus flexure.

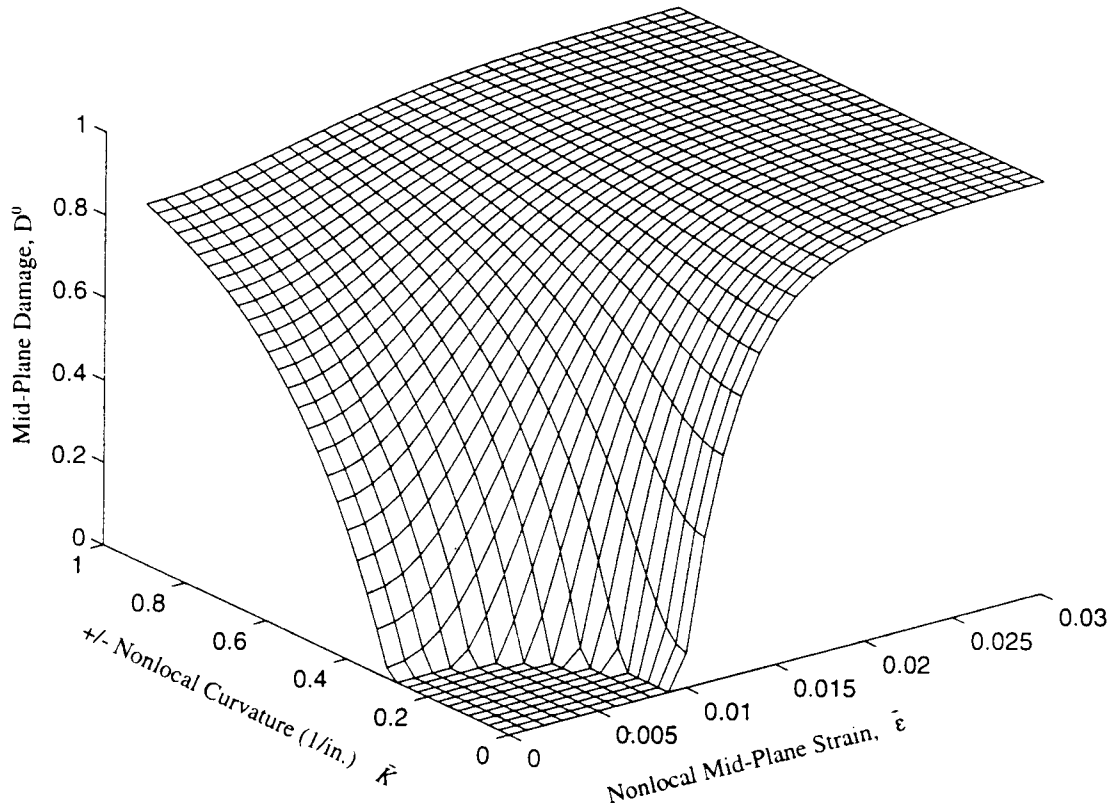


Figure 4.6 Proposed Mid-Plane Damage Growth Function Due to Extension + Curvature (only One quadrant of Damage Surface Shown).

For zero curvature, the above surface reduces to the curve shown in Figure 4.3. The initial damage growth threshold is assumed to be of an elliptical interaction between the critical mid-plane strain value and a critical pure curvature value. The damage accumulation rates are distinctly different for pure in-plane strain versus pure curvature conditions. Between these extremes, the damage growth rate varies sinusoidally such that its peak and minimum values correspond to the conditions of pure strain and pure bending. The proposed function was formulated as

$$D_{ii}^{0} = 0 \qquad \text{for: } 0 < \bar{z}_{ii} < 1 \qquad (4\text{-}18a)$$

$$D_{ii}^{0} = f_i(\bar{z}_{ii}) = 1 - \left[ \frac{1}{\bar{z}_{ii}} e^{-a_i \varepsilon^{cr} (z - 1)} \right]^{1/2} \qquad \text{for: } \bar{z}_{ii} > 1 \qquad (4\text{-}18b)$$

$$\text{where:} \quad \bar{z}_{ii} = \left[ \left( \frac{\bar{\varepsilon}_{ii}^{0}(1-c)}{\varepsilon_{ii}^{cr}} \right)^2 + \left( \frac{\bar{K}_{ii}(1-c)}{K_{ii}^{cr}} \right)^2 \right]^{1/2} + c \qquad (4\text{-}18c)$$

$$c = \frac{d}{2} ( \cos( 2\eta - \pi ) + 1 ) \qquad (4\text{-}18d)$$

$$\eta = \tan^{-1} \left( \frac{\bar{K}_{ii}/K_{ii}^{cr}}{\bar{\varepsilon}_{ii}^{0}/\varepsilon_{ii}^{cr}} \right) \qquad (4\text{-}18e)$$

This formulation reduces to equations (4-6) or (4-9) for conditions of no curvature. The combined effect of strain and curvature upon mid-plane damage growth is assumed to vary in an elliptical manner according to equation (4-18c). The damage growth rate varies according to equation (4-18d).

Since uniaxial pure bending tests of a laminate may reveal damage growth over a significant range of increasing curvature, the threshold value, $K_{ii}^{cr}$, is assumed in equation (4-18) to equal that curvature associated with damage initiation. Such a value could be determined from test results corresponding to the initial loss of linearity between applied moment versus resultant curvature. Analytically, such a value could be associated with first ply failure according to some ply failure criterion. Parameter "d" relates the damage accumulation rate parameters for pure bending versus the pure tension load conditions. For d = 0, their parameters are equal and successive cross-sections of the damage surface, at varying levels of damage, would generate concentric ellipses. The surface of Figure 4.6 is based upon d = 0.7 (for purpose of example only) and its successive cross-sections start as elliptical and subsequently deviate as shown in the damage contour plot of Figure 4.7.

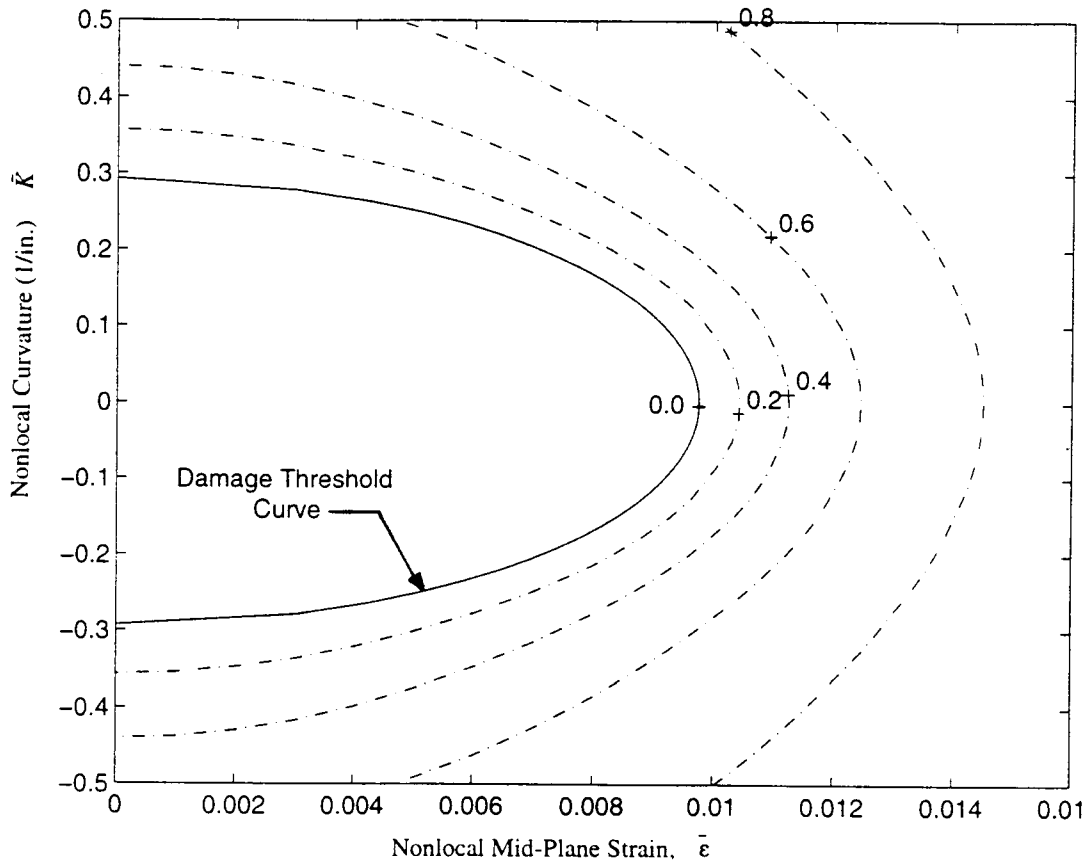


Figure 4.7 Damage Contours for Proposed Damage Function.

Definition of damage gradient growth is assisted by the concept of damage compliance; i.e.,

$$S = \frac{dD^0}{d\varepsilon^0} = \left( b_0 + b_2 \frac{t^2}{12} \right) + 2\left( c_0 + c_2 \frac{t^2}{12} \right)(\varepsilon^0) + 3\, d_0 (\varepsilon^0)^2 \qquad (4\text{-}19)$$

Relative to the particular damage function of Figure 4.3, the damage compliance takes the form shown in Figure 4.8.

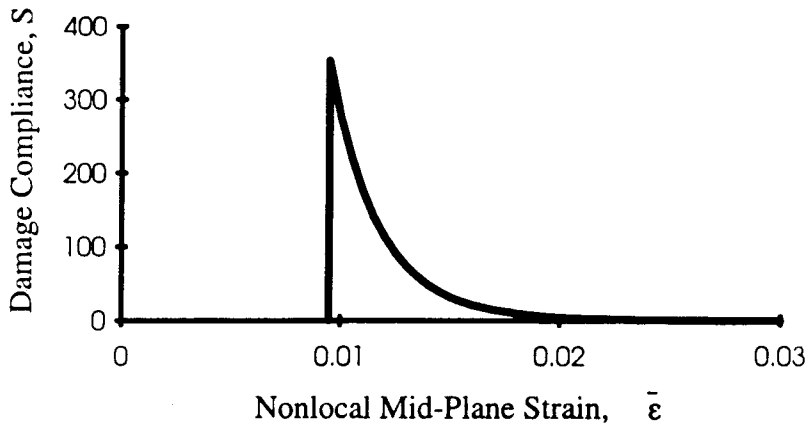


Figure 4.8 Example Damage Compliance (for: $\varepsilon^{cr} = .0095$, $a = 600$)

Expansion of the bulk damage gradient, defined in equation (4-14), using the series of equation (4-15), integrating through the plate thickness and recognizing the relation of equation (4-19), the damage gradient relation can be formulated as

$$\alpha = 2K\left[S + t^2 T(\varepsilon^0)\right] + K^3(2d_0) \tag{4-20a}$$

where $$T(\varepsilon^0) = \frac{b_2}{12} + 2 \cdot \frac{c_2}{12}\varepsilon^0 + \ldots \tag{4-20b}$$

The last term of $\alpha$, being cubic in curvature, should be of relative insignificance and was neglected. Had higher order terms of the power series been considered, their resultant contribution to the bulk damage gradient would also have been neglected for the same reason.

The bulk mid-plane damage, $D^0$, reflects an averaged value according to equation (4-12). Under flexural conditions, however, the near-surface damage compliance should be more influential upon the evolution of damage gradient than should the damage compliance of material at the mid-plane. Function $T(\varepsilon^0)$, defined in equation (4-20b), can be shown to represent the difference between the averaged through thickness damage

compliance, S, and that of material specific to the mid-plane. Of greater physical significance, however, is the influence of near-surface damage compliance over the averaged value, S. Assuming that this influence evolves in a manner similar to that of the averaged damage compliance, it could then be approximated as equal to S multiplied by an experimentally determined constant, v; i.e.,

$$T = v \cdot S(\varepsilon^0) \tag{4-21}$$

The damage gradient is then a product of the damage compliance, S, curvature, K, and the factor, $1 + vt^2$, the later of which represents the influence of near-surface compliance variation from S; i.e.,

$$\alpha = 2KS\left[1 + vt^2\right] \tag{4-22}$$

Constant v would be determined from tests in which both extension and flexure transpire.

For two dimensional plate continuum, no coupling is assumed to exist between extensional and twist related damage gradient terms. Also, no coupling is assumed between the two orthogonal extensional damage terms. The resultant matrix of plate damage gradient would be expressed as

$$\begin{Bmatrix} \alpha_{11} \\ \alpha_{22} \\ \alpha_{12} \end{Bmatrix} = 2\begin{bmatrix} S_{11}\left[1 + v_{11}t^2\right] & 0 & 0 \\ 0 & S_{22}\left[1 + v_{22}t^2\right] & 0 \\ 0 & 0 & S_{12}\left[1 + v_{12}t^2\right] \end{bmatrix} \begin{Bmatrix} K_{11} \\ K_{22} \\ K_{12} \end{Bmatrix} \tag{4-23}$$

The damage compliance, $S_{ij}$, and material constant, $v_{ij}$, in equation (4-23), do not cause damage to develop, this role is held solely by nonlocal curvature, **K**. Rather they filter the influence of curvature on the growth of a damage gradient.

Damage compliance, $S_{ij}$, is of zero value both before the initiation of damage, $D_{ij}^0$, and as damage approaches unity (complete failure). Therefore, according to equation (4-22), the same must be true for the damage gradient. This feature makes

physical sense considering the limits, placed on the damage gradient, that are necessary to maintain values of damage, D(z), within the range of zero to unity. This issue was discussed in Section 3 and the permissible range of damage gradient versus mid-plane damage is shown in Figure 3.1. Consequently, the damage gradient, $\alpha$, should rise and fall as curvature increases but remain within the confines of the permissible range defined by Figure 3.1.

The bulk mid-plane damage, $D^0$, evolves according to the uniaxial damage-strain relation of equation (4-18). Damage is a dissipative phenomena, thus the increments of mid-plane damage were not allowed to contract. No attempt is made herein to model the possible return of stiffness associated with compressive closure of cracks.

Damage gradient, $\alpha_{ij}$, is linearly dependent upon the corresponding components of curvature, $K_{ij}$ (equation (4-23)). As with the mid-plane damage strain dependency, the effect of curvature upon growth of a damage gradient is also of a non-contracting dissipative nature. No critical threshold of curvature is assumed for damage gradient growth; rather, its initiation is controlled by the damage compliance term S which in turn is a derivative of mid-plane damage $D^0$. Therefor $\alpha$ can not develop until $D^0$ does. But once $D^0$ has been initiated, $\alpha$ will be initiated by any degree of curvature. Finally, parameter $v_{ij}$ should be identified experimentally from a range of values so as to correlate simulation to experimental results and such that the permissible range of damage, shown in Figure 3.1, is not violated.

# 5. Finite Element Analysis

The finite element analysis (FEA) method was utilized for simulation of fracture tests which included notched uniaxial specimens and a large notched section of fuselage. For this purpose, an available FEA program was modified to incorporate the damage theory presented in Section 3 and 4. A detailed description of the original program can be found in Figueiras & Owen (1984). An 8-node, isoparametric, quadrilateral shell element was employed. Each node exhibited 5 degrees of freedom, 3 translations and 2 rotations; nodal rotation about the shell normal direction did not apply. Transverse shear deformation effects were included as well as geometric nonlinearity due to large deflections.

The modified program was capable of modelling strain softening of the stiffness degradation type according to the damage model presented in Section 3 and 4. Gaussian integration was employed for efficient computation of element stiffness. In support this computation, nonlocal strains were computed at each Gauss point for purposes of computing damage. Therefore, a nominally uniform shell element can develop non-uniform stiffness due to a variation of damage among its Gauss points.

The original program was constructed for implicit layered analysis of plasticity effects. Implicit layering defines a plate element as the sum of multiple layers each of which could plastically yield, or in this case damage, independently of the others and contribute a variable degree of stiffness to the total plate behavior. This construction was retained for analysis of progressive damage so as to minimize programming efforts; however, such an approach significantly compromised the potential efficiency of the damage theory. That is, the proposed damage theory defined damage and the effective $[\tilde{A}\tilde{B}\tilde{C}]$ stiffness on the basis of a bulk laminate representation. Such definition offers benefits with regard to computational efficiency and reduced memory requirements. It might be expected that layered FEA, defined for a single layer, would reduce to such a bulk representation; but such is not the case due to its lack of flexural stiffness definition

within any single layer. Rather it relies upon the in-plane stiffness of stacked layers to generate such stiffness. Many finite element programs have been formulated for bulk representation of laminated plate behavior using the well known [ABC] stiffness matrix. However such programs were not available as a source for modification.

Thirteen layers were defined for the plate element which corresponds to the 13 plies of the subject laminate. Such layering insured that the resultant element stiffness would be consistent with the [ABC] stiffness, derived using CLPT, which a cornerstone of the proposed damage theory. Plate damage, defined by terms of mid-plane damage $D^0$ and damage gradient $\alpha$, was translated into layer damage according to

$$D_{ij}(z_k) = D_{ij}^{0} + z_k \alpha_{ij} \tag{5-1}$$

where coordinate $z_k$ refers to the position of the $k^{th}$ layer (ply) relative to that of the laminate mid-plane. The damage effective ply stiffness was thus determined by substitution of equation (5-1) into

$$\tilde{\mathbf{Q}} = \mathbf{N}_D^T : \bar{\mathbf{Q}} : \mathbf{N}_D \tag{5-2}$$

where

$$\left[N_D\right] = \begin{bmatrix} 1-D_{11}(z_k) & 0 & -D_{12}(z_k)/2 \\ 0 & 1-D_{22}(z_k) & -D_{12}(z_k)/2 \\ -D_{12}(z_k) & -D_{12}(z_k) & 1-\dfrac{\left(D_{11}(z_k)+D_{22}(z_k)\right)}{2} \end{bmatrix} \tag{5-3}$$

where $\bar{\mathbf{Q}}$ refers to the ply stiffness transformed to the principal laminate basis. Equation (5-2) is a suitable simplification of the effective stiffness equation (3-18a). Since damage is still defined by the damage terms $D^0$ and $\alpha$ and since each ply is represented as

an independent layer, accurate representation of the effective bulk laminate stiffness, equation (3-17), is assured. It should be stressed that the above layered definition of damage and effective stiffness is an artifact of the original FEA program and proper FEA programming of the damage theory would be of a non-layered bulk representation.

## 5.1 FEA Theory

Theoretical development of the finite element method, used herein, can begin with the basic constitutive relation between stress and strain for the damaged material.

$$\{\sigma\} = [\tilde{Q}]\ \{\epsilon\} \tag{5-4}$$

In finite element formulation, the principal laminate basis may be orientated at some angle $\theta$ relative to the global coordinates x and y. We can transform stresses and strains through the usual transformation relations (Jones, 1975) to get

$$\{\sigma\} = [T_\sigma]\ \{\sigma'\} \tag{5-5}$$

and

$$\{\epsilon\} = [T_\epsilon]\ \{\epsilon'\} \tag{5-6}$$

where, the prime basis refers to global coordinate system; and,

$$\{\sigma'\}^T = [\sigma'_x\ \sigma'_y\ \tau'_{xy}] \tag{5-7}$$

$$\{\varepsilon'\}^T = [\varepsilon'_x\ \varepsilon'_y\ \gamma'_{xy}] \tag{5-8}$$

$$[T_\sigma] = \begin{bmatrix} \cos^2\theta & \sin^2\theta & 2\sin\theta\cos\theta \\ \sin^2\theta & \cos^2\theta & -2\sin\theta\cos\theta \\ -\sin\theta\cos\theta & \sin\theta\cos\theta & \cos^2\theta - \sin^2\theta \end{bmatrix} \tag{5-9}$$

$$[T_\epsilon] = \begin{bmatrix} \cos^2\theta & \sin^2\theta & \sin\theta\cos\theta \\ \sin^2\theta & \cos^2\theta & -\sin\theta\cos\theta \\ -2\sin\theta\cos\theta & 2\sin\theta\cos\theta & \cos^2 - \sin^2\theta \end{bmatrix} . \tag{5-10}$$

Combining equations (5-4), (5-5), and (5-6) gives the constitutive relation in the global coordinate basis; that is,

$$\{\sigma'\} = [\tilde{C}'] \{\epsilon'\} \tag{5-11}$$

where

$$[\tilde{C}'] = [T_\sigma]^{-1} [\tilde{C}] [T_\epsilon] . \tag{5-12}$$

To develop a finite element formulation for progressive damage analysis, we begin with the principle of virtual work (Bathe, 1982)

$$\int_V \{\hat{\epsilon}'\}^T \{\sigma'\} dV = \int_S \{\hat{u}\}_S^T \{f\} ds \tag{5-13}$$

where $\{\hat{\epsilon}'\}$ is the strain associated with the virtual displacement $\{\hat{u}\}$, $\{\hat{u}\}_S$ is the virtual displacement of the surface of the body, and $\{f\}$ is the traction on the surface of the body. We will develop this analysis for an 8-node quadrilateral shell element. Using the usual shape functions of this element (Figueiras & Owen, 1984), we can express the displacement $[u]_m$ within an element "m" in terms of the nodal displacement $\{U\}$ as

$$\{u\}_m = [L]_m \{U\} . \tag{5-14}$$

Applying the strain-displacement relations to equation (5-14), we arrive at the following relation (Hinton & Owen, 1977) between strain and nodal displacement

$$\{\epsilon'\}_m = [B]_m \{U\} . \tag{5-15}$$

Substituting equation (5-14) and (5-15) into equation (5-13) gives

$$\sum_m \int_{V_m} [B]_m^T \{\sigma'\}_m \, dV_m = \sum_m \int_{S_m} [L]_{S_m}^T \{f\}_m \, dS_m . \tag{5-16}$$

Substituting equation (5-11) into equation (5-16) gives

$$\left( \sum_m \int_{V_m} [B]_m^T [\tilde{C}']_m [B]_m \, dV_m \right) \{U\} = \sum_m \int_{S_m} [L]_{S_m}^T \{f\}_m \, dS_m . \tag{5-17}$$

We now set

$$[K] = \sum_m \int_{V_m} [B]_m^T [\tilde{C}']_m [B]_m \, dV_m , \tag{5-18}$$

$$\{R\} = \sum_m \int_{S_m} [L]_{S_m}^T \{f\}_m \, dS_m . \tag{5-19}$$

Thus

$$[K] \{U\} = \{R\} \tag{5-20}$$

where [K] is the stiffness matrix and {R} is the generalized nodal load matrix. After damage initiates, equation (5-20) represents a nonlinear system of algebraic equations because [K] is a function of the nodal displacement vector U due to strain induced damage. Equation (5-20) can be solved iteratively using the Newton-Raphson method (Bathe, 1982). It was found that convergence difficulties arose for materials whose stress-strain curves had softening regimes with steep slopes. To overcome these difficulties, the viscous relaxation technique was called upon (Webster, 1980). A small

amount of viscous damping was introduced into the analysis and the problem was treated as being dynamic (without inertia effects) so that equation (5-20) was replaced by

$$[C_d]\{\dot{U}\} + [K]\{U\} = \{R\} \tag{5-21}$$

where $[C_d]$ is the damping matrix and $\{\dot{U}\}$ is the time derivative of $\{U\}$. To solve the above differential equations numerically, we used the trapezoidal rule of time integration (Bathe, 1982), that is,

$$^{t+\Delta t}\{U\} = {}^{t}\{U\} + \Delta t\,(\,{}^{t}\{\dot{U}\} + {}^{t+\Delta t}\{\dot{U}\})/2 \tag{5-22}$$

where the superscript in front of the variable indicates the time at which it is evaluated. For the damping matrix we employed Rayleigh damping, i.e.,

$$[C_d] = \beta\,[K]\,. \tag{5-23}$$

A damping value of $\beta = 0.01$ sec$^{-1}$ for a time step $\Delta t = 1$ sec eliminated the convergence problems and also reproduced results that were within a fraction of a percent of previous static calculations.

The FEA employed an 8-node Serendipity shell element and reduced 2x2 Gaussian integration. Literature indicated that higher order elements exhibit greater nonlinear material influence whereas lower order elements (4-node) tend to exhibit brittle behavior (Dopker et al., 1994). A reduced 2x2 integration was employed, rather than 3x3 integration, to avoid the potential problem of artificial stiffening associated with 3x3 integration applied to thin shells (Hinton & Owen, 1977). 2x2 integration is also less computationally expensive. Subsequent examination of this option indicated no problems with 3x3 integration for the conditions analyzed. 3x3 integration actually conveyed greater nonlinear behavior and produced slightly higher fracture strengths given the same material properties.

## 5.2 Nonlocal Strain Computation

Local strain values were determined for each Gauss point within the finite element model using conventional Gaussian integration. Nonlocal strains were also evaluated for each Gauss point based upon a summation of local strains within its nonlocal region. The summation represented a discrete form of the integration defined in equation (4-1). The nonlocal summation utilized a weighting matrix analogous to the weighting function of equation (4-2) and depicted in Figure 4.2. Construction of the weighting matrix required determining which Gauss points lay within the nonlocal range of each and every Gauss point. The size of the nonlocal range depended upon the size of the characteristic length $l_{ch}$ which was considered a material property. Weight values were then assigned, according to equation (4-2), for each component of the weight matrix. Nonlocal strain was thus determined for each Gauss point based upon a summation of the weighted local strains.

The above nonlocal summation required two cases of special treatment: where a Gauss point's nonlocal range reached beyond the structures edge and also were the range reached across a model's symmetry boundaries. The first condition was easily addressed by accepting the limited range defined by the limits to the structural geometry. In this case, the value of the total integrated weight, defined in equation 4-3, was reduced accordingly.

Nonlocal treatment across a symmetry boundary was made possible by establishing a dummy mesh across the boundary. This mesh was assigned zero stiffness and its nodes were fully constrained; therefore, it made no physical contribution to the solution. However, for purposes of determining nonlocal strain for Gauss points within the main body of the model, the local strain of the main body were assigned to the dummy Gauss points using a symmetry protocol. The dummy mesh needed to be of a span no greater than the outer radius of the nonlocal region. Its Gauss points were included in defining the weight matrices and thus their geometric positions were

significant. Thus the dummy mesh needed to be an exact mirror reflection of the mesh with which it shared the symmetry boundary.

The above dummy mesh method, or some other method, is needed only if symmetry boundary conditions are utilized. Given sufficient resources, all problems can be modelled without resorting to the symmetry technique; and many problems are such that symmetry can not be assumed. However, the technique does serve to make many important computations affordable. It is unlikely that the proposed dummy mesh approach seriously compromises the benefit of taking advantage of symmetry in structural modelling. The dummy mesh method was utilized because of its simplicity. Other methods of nonlocal treatment across a symmetry boundary are possible which could be more eloquent and efficient.

# 6. Experimental Characterization of Damage Growth

For a specific laminate, damage growth may be characterized by experiment to quantify the nonlocal characteristic length, damage threshold strains and damage rate parameters proposed in Section 4. Threshold strains, $\varepsilon_{ij}^{cr}$ and $K_{ij}^{cr}$ are determined from uniaxial tension and pure bending (4 point bend) tests. Testing for the damage accumulation rate parameters, $a_{ij}$, $d_{ij}$ and $v_{ij}$, is complicated by the tendency for strain softening materials to experience localization of the damage phenomenon. Such behavior, in a simple uniaxial tension test, is interpreted as brittle failure. The resultant strength is sensitive only to the threshold of damage initiation and not the body of the damage function itself. Fracture, however, exhibits damage nucleation at the crack tip and subsequent growth prior to gross failure. Simulation of such behavior is sensitive to all of the damage parameters of concern. By performing multiple fracture tests and subsequent simulations, a best fit selection of the nonlocal characteristic length and damage growth rate parameters can be attained. This approach is referred to as the Inverse Method and was discussed in the literature review of Section 2.3.

Damage is characterized, herein, for the graphite/epoxy laminate which served as skin to the large transport aircraft fuselage developed under the Advanced Technology Composite Aircraft Structure (ATCAS) program as directed by the National Aeronautical and Space Administration (NASA). Specifically, damage tolerance analysis of the fuselage crown (upper quadrant) was the purpose behind this damage theory. The laminate (designated as Crown-3 within the ATCAS program) consists of 13 plies of [45/-45/90/0/60/-60/90/-60/60/0/90/-45/45] layup and .096 inch nominal thickness. Lamination utilized the tow process in which narrow strips of the graphite/epoxy tape (tows) are placed using computer controlled tooling. The 0 degree ply corresponds to the fuselage axial direction. The critical damage tolerance condition is specified as a large axially aligned crack that grows due to loading in the circumferential (hoop) direction. The hoop direction is designated the 2-axis of the

principal laminate basis. Thus, characterization of the damage growth $D_{22}^{0}$ = function( $\varepsilon_{22}^{0}$ , $K_{22}$ ) and $\alpha_{22}$ = function ($K_{22}$) was critical.

Each ply consisted of AS4 graphite fibers and 938 epoxy resin constituents constructed in a tape form. The resin is of 350 degree Fahrenheit cure had no toughening additives. The cured laminate exhibited approximately 57% fiber volume (Walker et al., 1991). Resultant ply stiffness properties were $E_1$ = 19.62 Msi, $E_2$ = 1.36 Msi, $G_{12}$ = 0.72 Msi, and $v_{12}$ = 0.32.

An initial attempt at characterizing damage, for non curvature conditions, was not successful. It employed a technique that has so far been demonstrated only on concrete (Bazant & Pijaudier-Cabot, 1989, Mazars et al., 1989b). Using a simple tension specimen, strain localization can be prevented and damage constrained to distribute uniformly over the entire specimen length, by sandwiching the specimen between material layers of greater elastic strain capability. As damage grows, the specimen material softens, and load is supported by the outer sandwich layers. In this way, catastrophic failure is prevented upon the onset of damage. Application to the above Crown-3 laminate was unsuccessful due to inadequate suppression of damage localization. Considering the potential of the technique however, the experience is described in Section 6.1. Further efforts along this avenue are warranted. It should be recognized that no such method has been identified in the literature for flexural conditions.

Using the Inverse Method, damage will first be characterized for non-curvature conditions in Section 6.2. Such conditions enable the determination of the nonlocal characteristic length, threshold mid-plane strain and extensional damage rate parameters. Relevant strength and fracture tests were performed by the Boeing Company and Oregon State University. Simulation was performed using the nonlinear finite element analysis (FEA) defined in Section 5.

Curvature conditions are subsequently considered in Section 6.3, using the Inverse Method, to evaluate the remaining rate parameters, $d_{ij}$ and $v_{ij}$. Parameter $d_{ij}$ relates the mid-plane damage growth to curvature while $v_{ij}$ relates the damage gradient

growth to curvature. A novel fracture test was developed which involved both tension and curvature. As rationalized in Section 4, curvature should influence growth of both the mid-plane $D^0$, and the damage gradient, $\alpha$. It is not possible to experimentally differentiate between these aspects of damage. In other words, only one damage parameter can be determined from a single test method. Since two damage parameters require quantification, each were evaluated assuming the absence of the other damage effect. Results should indicate the relative influence that these two aspects of damage growth have upon fracture. This qualitative characterization of damage will impose a degree of uncertainty upon the analysis of fuselage damage tolerance. In the future, however, the growth of these two aspects of damage, $D^0$ and $\alpha$, may be related by recognizing their mutual dependence upon the damage resistance of a laminate's outer plies.

## 6.1 Experiment - Direct Measurement of Stress-Strain Softening

Direct measurement of strain softening was attempted using the experimental technique demonstrated by Bazant & Pijaudier-Cabot(1989) and Mazars et al. (1989b) in application to concrete. Application of the technique, to the Crown-3 laminate, failed to prevent strain localization and results were useless. However, experimentation on yet another graphite/epoxy laminate yielded results of interest. Considering the technique's potential for direct characterization of damage growth, further efforts are warranted.

The technique was based upon the simple tension test. To avoid the usual mode of specimen failure, in which strain and damage localize to a narrow band and load resistance is lost in an apparent brittle manner, the specimen was sandwiched by a two laminates of greater elastic deformation capability. That is, the usual catastrophic loss of load transfer is prevented by the integrity of the sandwich face laminates. In these experiments, a graphite/epoxy (gr/ep) laminate is sandwiched between two laminates of glass/epoxy (gl/ep). As damage initiates, at some point within the gr/ep laminate, the

point softens and load is shunted around the point and into the gl/ep. In this way, damage is constrained to develop uniformly over the specimen length. The gl/ep laminate was selected because of its greater elastic strain capability and its thickness was selected to ensure sufficient stiffness. Eventually, the gr/ep laminate would attain complete and uniform failure.

The stress-strain softening behavior of the gr/ep laminate would be extracted from the total specimen behavior by subtracting the predictable linear elastic behavior of the gl/ep sandwich face laminates. Ideally, surface mounted strain gages could be used to measure the sandwich strain. However, an extensometer spanning a significant section of the sandwich specimen length is preferred so as to maximize the measured effects of strain softening and to avoid sensitivity to any localized anomaly.

Experimentation on the Crown-3 laminate failed to constrain damage localization and the usual brittle nature of failure prevailed. The 1.0 inch wide specimen was sandwiched between two laminates of gl/ep which offered greater elastic strain capability. The combined stiffness of the gl/ep laminate was equal to that of the nominal Crown-3 laminate in its hoop direction. The sandwich was bonded uniformly using a general purpose, good strength, aerospace grade epoxy (Scotch-Weld 2216 by 3M). The gl/ep was intended to be of uniaxial fiber orientation, however, the delivered product contained 15% lateral fiber orientation. Such was not desired because the resultant lateral stiffness could restrain lateral deformation of the gr/ep and cause something other than uniaxial load conditions within it. Although undesired, this aspect was not a likely cause of the experimental failure. Rather it was expected that the initiation of damage, within the sandwiched Crown-3 laminate, was too energetic and caused failure of the epoxy bond.

A second laminate of gr/ep was tested which, due to its lower stiffness and lower damage threshold strain, was expected to release less energy during its damage process. This laminate was also sandwiched using the same gl/ep laminate and epoxy adhesive as described above. Tension testing of the sandwich specimen again resulted in insufficient suppression of damage localization some results are of interest. By subtracting the

elastic behavior of the gl/ep face laminates from the total specimen stress-strain behavior, the stress-strain softening of the gr/ep laminate was determined. However, the best example of its resultant stress-strain softening behavior is shown in Figure 6.1. The test employed displacement control. The mechanism involved in the abrupt loss of load is not known but it seems safe to assume that constraint of damage and strain localization was not of the desired uniformity.

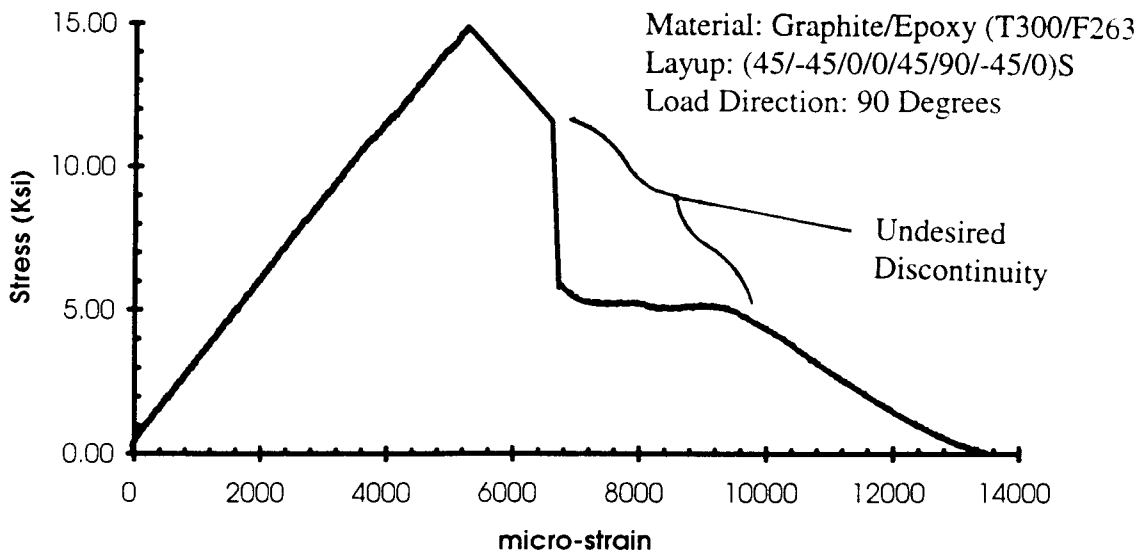


Figure 6.1 Example Stress-Strain Softening via Sandwich Tension Test.

## 6.2 Damage Characterization for Non-Curvature Conditions

According to the damage kinetics of Section 4, no damage gradient can develop in the absence of curvature (i.e. $\alpha_{ij} = 0$ ). Also, mid-plane damage, $D^0$, would be a function of only mid-plane strain as defined by equation (4-5) or (4-8) (depending on whether or not shear is dominant). To completely characterize damage, the threshold

strains, $\varepsilon_{11}^{cr}$, $\varepsilon_{22}^{cr}$ and $\gamma_{12}^{cr}$, nonlocal characteristic length, $l_{ch}$, and damage accumulation rate parameters $a_{11}$, $a_{22}$ and $a_{12}$ require quantification. The extensional threshold strains $\varepsilon_{11}^{cr}$ and $\varepsilon_{22}^{cr}$ are determined as the failure strains derived from uniaxial 0 and 90 degree tension tests of the laminate. Several tests could be employed to determine the shear threshold strain, $\gamma_{12}^{cr}$; the cheapest but possibly less accurate of which would be a uniaxial, off-axis (possibly 45 degree off-axis), tension test. Similarly, it is proposed that the rate parameters, $a_{11}$, $a_{22}$ and $a_{12}$, as well as the characteristic length, $l_{ch}$, be determined from 0, 90 and 45 degree fracture tests, respectively.

### 6.2.1 Test Results

Results from a limited number of tests were made available from the NASA directed ATCAS program. Test results refer to the "Crown-3" graphite/epoxy laminate which served as skin to the fuselage developed under the ATCAS program. No further tests could be performed due to a lack of stock laminate.

Uniaxial strength and fracture test results were made available by the Boeing Company, a participant in the ATCAS program. Specifically, no-notch and notched fracture strength test results were made available for the axial and hoop directions of the laminate. No off-axis tests were performed and therefore no shear damage characterization was possible. Although the finite data set made characterization of shear damage impossible, such was not needed in determining the damage tolerance of the subject fuselage crown panel. This was because the fuselage damage tolerance load condition was one of pressure which induced a state of bi-axial tensions and no shear. Shear does develop due to the presence of a notch. But analysis suggested a magnitude insufficient to cause damage. In addition, post-test examination indicated that damage did not develop in the area of maximum shear. Had damage tolerance of the fuselage side quadrant been the issue, shear damage characterization might be critical due to the significant shear realized during aircraft maneuver conditions. A complete list of tests

performed by the Boeing Company, for the Crown-3 laminate as well as others, can found in Walker et al. (1996). Results utilized herein are shown in Table 6.1. The S6 and S7 laminates will be referred to in later discussion.

| Detail | None | | Notched | | | | | | |
|---|---|---|---|---|---|---|---|---|---|
| Notch Length (in.) | NA | NA | 0.25 | 0.75 | 0.88 | 0.88 | 2.00 | 2.50 | 12.00 |
| Width (in.) | 1.00 | 2.00 | 1.00 | 3.00 | 3.50 | 4.00 | 8.00 | 10.00 | 60.00 |
| Length (in.) | 10.00 | 12.00 | 12.00 | 12.00 | 12.00 | 8.00 | 24.00 | 30.00 | 150.00 |
| W/2a | NA | NA | 4.00 | 4.00 | 4.00 | 4.57 | 4.00 | 4.00 | 5.00 |
| Laminate | Strength (Ksi) | | | | | | | | |
| Crown 3 - Hoop | | 83.67 | 65.45 | 50.88 | 51.98 | | 42.06 | 38.90 | 22.51 |
| Crown 3 - Axial | | 58.03 | 35.03 | | 30.03 | | | | |
| S6 - Hoop | 90.42 * | | | | | | | 31.10 | |
| S7 - Hoop | | | | | | 42.31 * | | 25.70 | |

* Tests performed by Oregon State University
NA = Not Applicable

Table 6.1 Experimental Crown-3 Laminate Uniaxial Strengths (Ksi).

### 6.2.2 Simulation - Nonlinear Finite Element Analysis

Nonlinear finite element analysis (FEA) was programmed, as defined in Section 5, to simulate the various fracture tests. Simulation results were dependent upon the values given to the various damage parameters. Multiple simulations then enabled identification of the best set of parameters for correlating the theory to test results. To this end, a one-quarter symmetric model of the center-notched fracture specimen was created as shown in Figure 6.2. The model is shown in a state of deformation due uniaxial extension. The known symmetry of the induced deformation was taken advantage of in order to reduce the model size and computational expense. The area of mesh shown below the lateral symmetry boundary represents the dummy mesh added for

the sole purpose of calculating nonlocal strains (discussed in Section 5.2). The dummy mesh was given zero stiffness and was fully constrained; it therefore made no direct contribution to the solution. No dummy mesh was added to the longitudinal symmetry boundary because conditions for damage do not develop in this area.

The analysis employed displacement control of the specimen ends to generate tension. To achieve solution accuracy at minimum cost, a series of mesh densities were exercised in search of acceptable solution convergence. For example, three mesh densities were analyzed for the 2.5 inch notch fracture and their load versus displacement results for are shown in Figure 6.3. Apparently, reducing the damage zone element size from .156 inches to .078 inches only effected the results by 1.05 percent. In this case, it was decided that costs associated with computation of the finest mesh were not justified by a 1.05 percent solution refinement. Thus the .156 inch element size was carried forward in all calculations of the 2.5 inch notch fracture. Similarly, the 0.875 inch notch and 12.0 inch notch fracture models resulted in damage zone element size selection of 0.1094 inch and .1875 inch respectively.

### 6.2.3 Damage Parameter Selection

A method for evaluating a laminate's damage parameters (threshold strains, characteristic length and damage growth rate) is presented below with application to the Crown-3 laminate. Damage threshold strain was simply determined from uniaxial no-notch tension testing. The nonlocal characteristic length and damage rate parameters were determined from fracture tests. The effort focused on laminate hoop directed parameters because of their significance in analysis of fuselage tolerance to a large notch of axial alignment.

Simulation of hoop fracture, caused by hoop directed loading of an axial notch, registered only hoop directed damage, $D_{22}^{0}$. Likewise, only axial damage developed for an axially loaded fracture. Therefore, for a given fracture test loaded in the i-direction

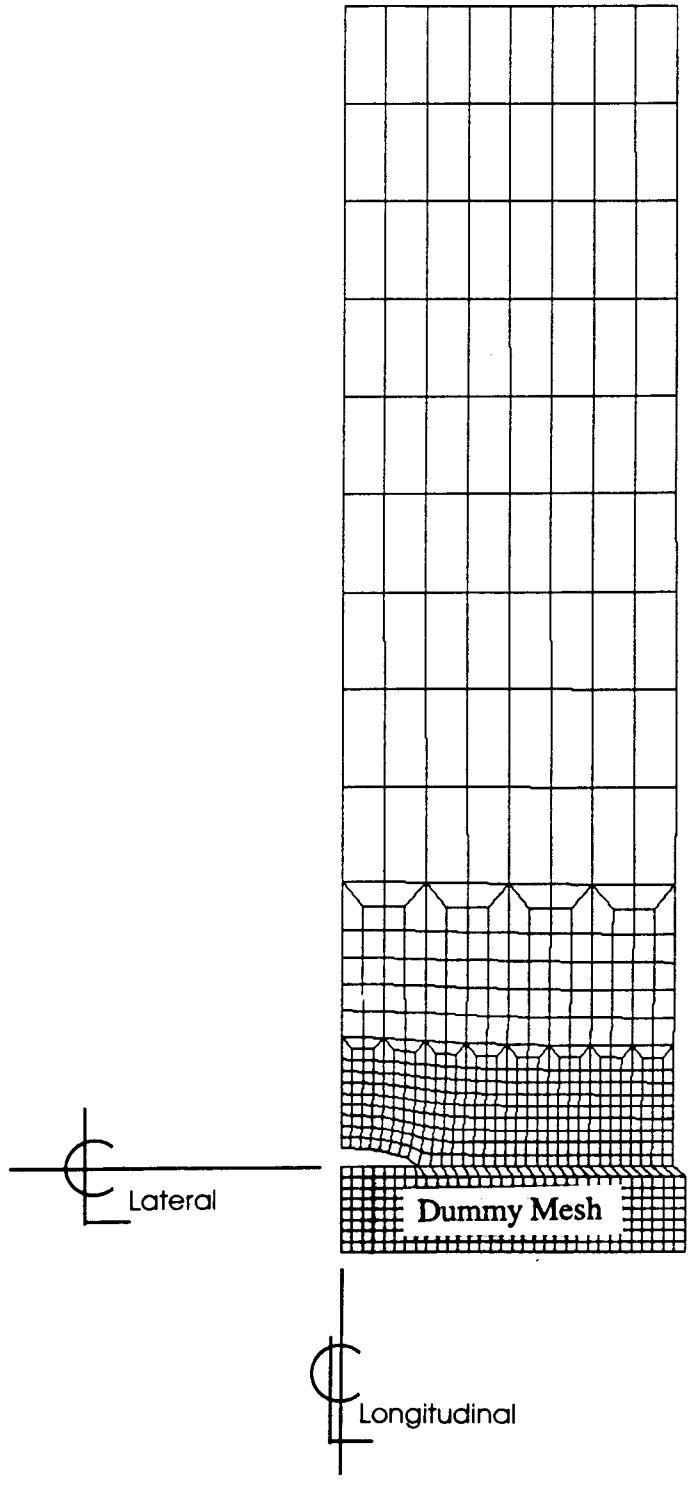


Figure 6-2 Quarter Symmetry Finite Element Model of Fracture Specimen - Deformed Shape.

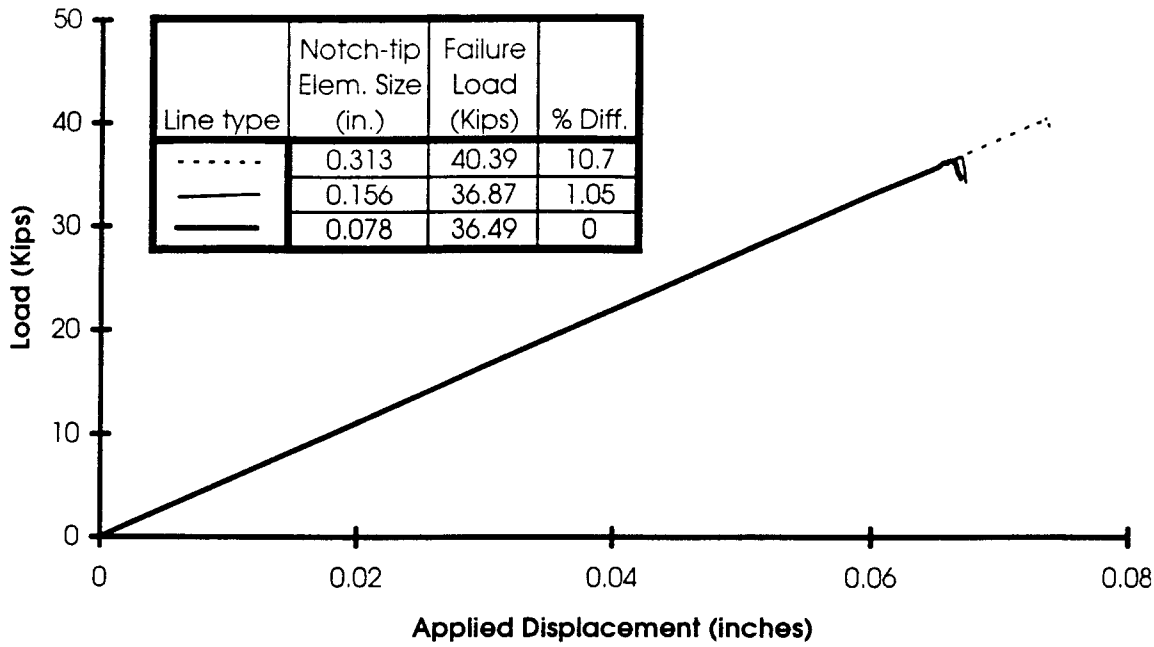


Figure 6.3 Displacement Controlled Simulation of 2.5 inch Notch Fracture - Results for Three Mesh Densities.

and associated threshold strain, $\varepsilon_{ii}^{cr}$, the corresponding simulated fracture strength can be plotted as a surface over the field of damage parameters $l_{ch}$ and $a_{ii}$. Correlation of the surfaces, with test results, enables the selection of a set of damage parameters $l_{ch}$ and $a_{ii}$ that apply to all conditions of fracture in the i-direction.

The damage threshold strain values are determined from the no-notch test values of Table 6.1. The uniaxial test, loaded in the hoop direction, can be expressed by the undamaged bulk-laminate in-plane compliance matrix,[S], i.e.,

$$\begin{Bmatrix} \varepsilon_{11}^{0} \\ \varepsilon_{22}^{0} \\ 0 \end{Bmatrix} = \begin{bmatrix} S_{11} & S_{12} & 0 \\ S_{12} & S_{22} & 0 \\ 0 & 0 & S_{33} \end{bmatrix} \begin{Bmatrix} 0 \\ \sigma_2 \\ 0 \end{Bmatrix} \tag{6-1}$$

where stress $\sigma_2$ is tensile, strain $\varepsilon_{11}^0$ is compressive and $\varepsilon_{22}^0$ is extensional. Strain $\varepsilon_{22}^0$ can be expected to become critical long before $\varepsilon_{11}^0$ because Poissons' ratio ensures a much lesser compressive strain. Also, literature has shown any compressive damage threshold to be significantly greater than the extensional counterpart. Thus the laminate failure stress, reported in Table 6.1, can be directly related to a corresponding threshold strain of the same direction. Laminate compliance components $S_{12}$ and $S_{22}$ are determined from inversion of the [ABC] matrix (Jones, 1975). Such analysis of the no-notch tests resulted in threshold strains of $\varepsilon_{11}^{cr} = 0.01101$ and $\varepsilon_{22}^{cr} = 0.00948$ (laminate axial and hoop directions respectively).

The remaining damage parameters were determined from correlation of simulation with results of fracture tests. Variation of the nonlocal characteristic length, $l_{ch}$, and damage rate parameters, $a_{ii}$, allow a surface of strength to be defined via simulation. An example of such a surface is shown in Figure 6.4 corresponding to the 2.5 inch hoop fracture simulation. This surface must satisfy conditions on strength for limit values of $l_{ch}$ and $a_{22}$. A zero value of the rate parameter $a_{22}$ results in a never decreasing stress-strain relation, according to equation (4-6), which is similar to ideal plasticity. Such a condition would eventually result in a uniform variation of stress, across the notched section of the specimen, equal to the no-notch strength $\sigma^0$. Specimen notch strength would then depend upon its width to notch length ratio. A ratio of four was incorporated into the fracture specimens which would translate into a notched failure stress of $0.75 * \sigma^0$ for $a_{22} = 0$. The same would result from an infinite characteristic length, which would effectively eliminate the influence of the local notch stress riser. A zero $l_{ch}$ and infinite rate parameter represents an ideally linear brittle material which would have no fracture strength at all. The surface of Figure 6.4 satisfies these conditions and is shaped to fit (least square criterion) simulations based upon intermediate coordinates of the damage parameters, ($l_{ch}$, $a_{22}$).

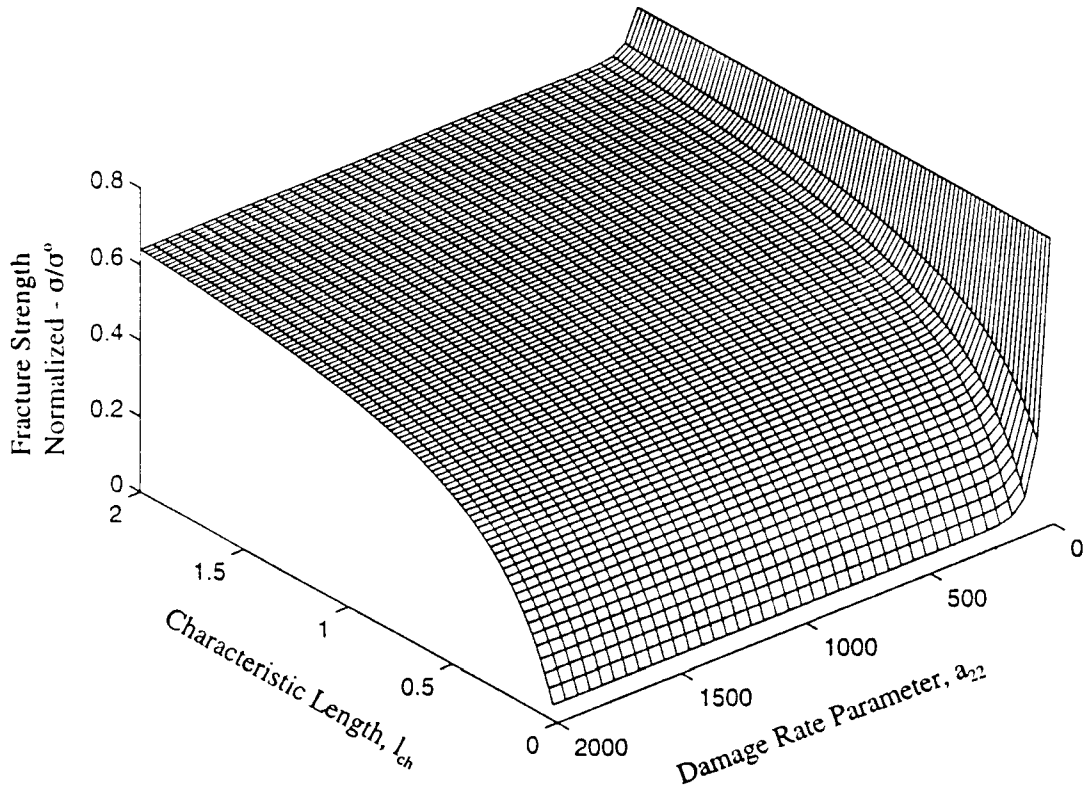


Figure 6.4 Fitted Surface of Simulated Strengths.

The surface of Figure 6.4 was based upon a least square fit of a nonlinear function to simulation results. It conveys a global effect of damage parameter selection on specimen fracture strength. However the fit was not considered sufficiently accurate for use in selecting the best parameter pair for all fracture conditions. Therefore a limited range of the damage parameter coordinate was considered and a linear strength function was selected to exactly correlate with three strategically selected simulation results. The range $[0.0 < l_{ch} < 0.8$ inch and $150 < a_{ii} < 2000]$ was identified to capture a broad range of strengths and to include strain softening behavior reported upon in the

literature. The range of the damage rate parameter is shown in Figure 4.4 in terms of its effect on the stress-strain softening relation. Although the linear surface function is fully characterized by correlation to three simulation results, its correlation with intermediate simulations has been demonstrated to be good as shown in the section plots of Figure 6.5 ad 6.6. It is apparent from these figures that simulated strength is much more sensitive to variation of the characteristic length than it is to the damage rate parameter greater than a value of 150. The divergence of the simulated and fitted strength of Figure 6.5, for small $l_{ch}$ values, is an artifact of element size in simulation. The finite element size in simulation was unable to reflect effects of vanishing $l_{ch}$.

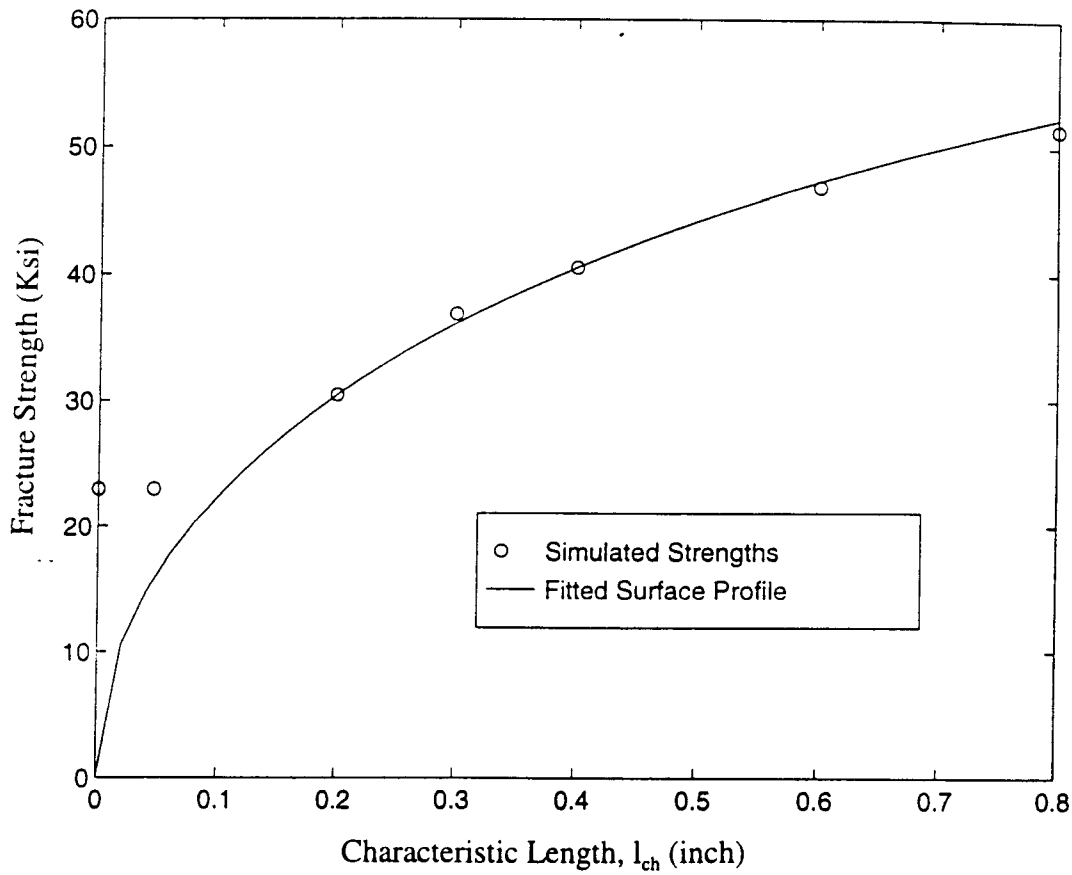


Figure 6.5 Simulated Strength Surface Fit to Variation of Nonlocal Characteristic Length, $l_{ch}$.

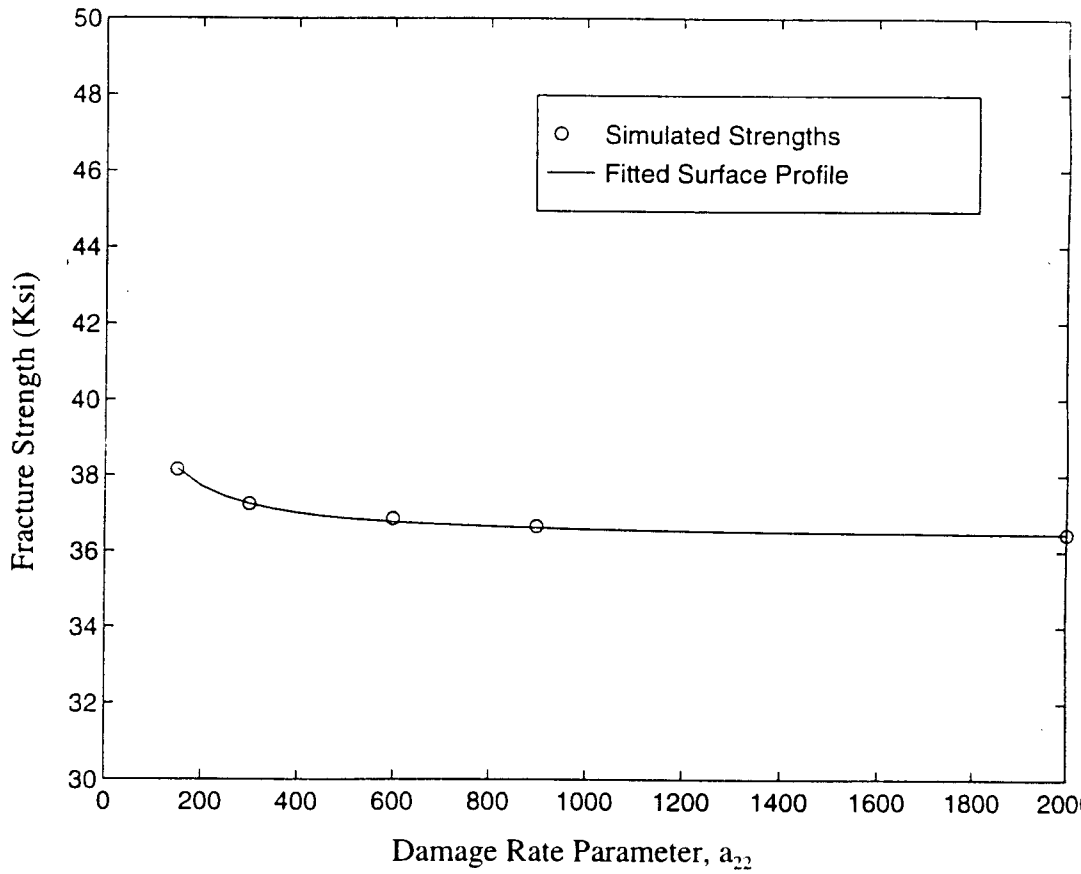


Figure 6.6 Simulated Strength Surface Fit to Variation of Damage Rate, $a_{ii}$.

In the context of the above simulated strength surface, a fracture test result would be represented by a level plane. These surfaces are shown in Figure 6.7. The intersection of these surfaces is a curve whose damage parameters equate simulation to test results. This method was applied to the 0.875, 2.5 and 12.0 inch notched hoop-fracture tests and a 0.875 inch notched axial-fracture test. Resultant parameter solution curves are shown in Figure 6.8. It is apparent, from these solution curves, that no single characteristic length value will exactly correlate with all test results.

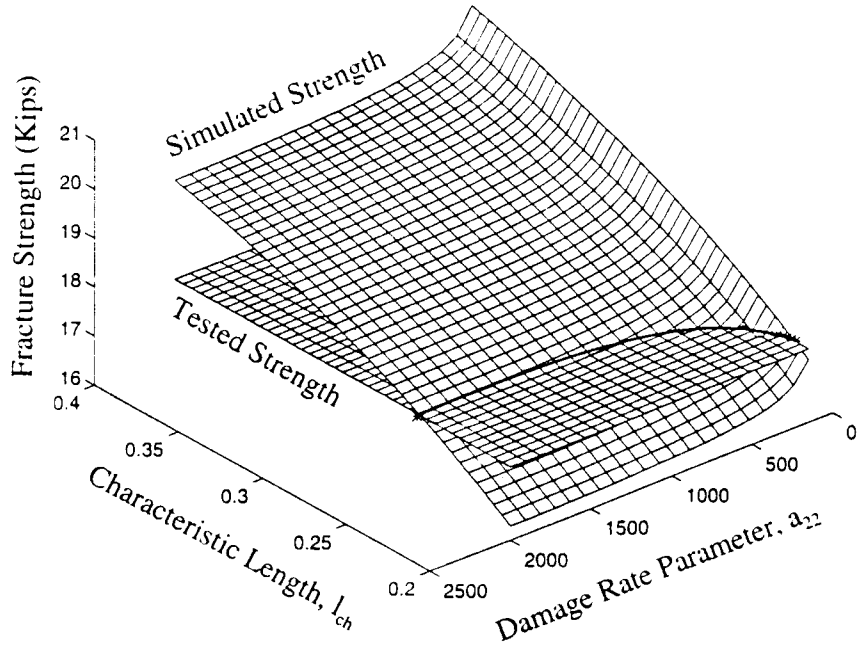


Figure 6.7 Parameter Solution Curve Defined by Surface Intersection.

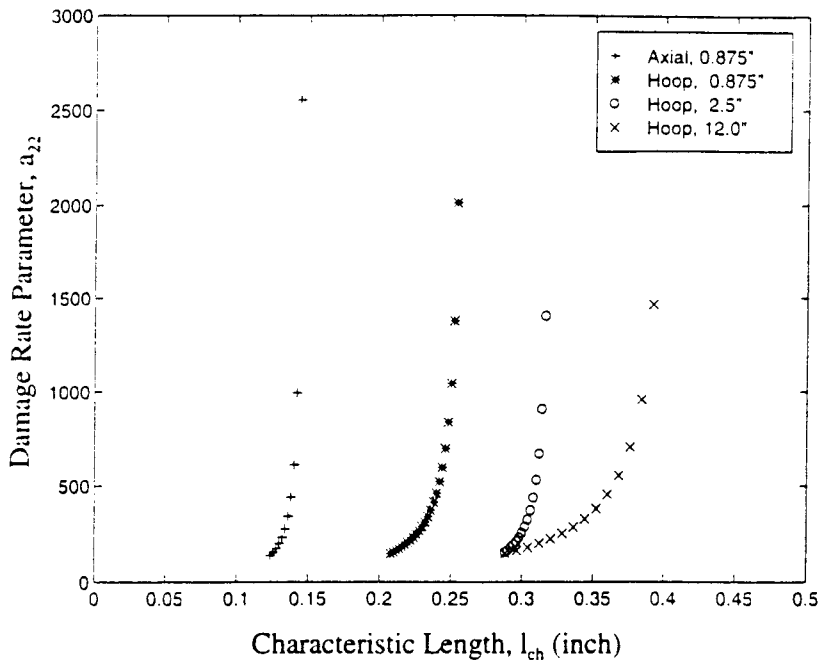


Figure 6.8 Parameter Solution Curves for each Fracture Test.

It is not clear, from the curves of Figure 6.8, which parameter set best correlates to the various test results. Since the determination of fuselage damage tolerance is the objective, the analysis should focus on the hoop fracture results. Therefore, disregarding the axial fracture curve, two combinations of $l_{ch}$ and $a_{22}$ were chosen. One combination ($l_{ch}$ = .285, $a_{22}$ = 150) can be selected as the only identifiable intersection between the established solution curves (2.5 and 12.0 inch notched hoop fracture curves). This parameter pair is likely the best selection for extending the analysis to the 22.0 inch notched fuselage panel. Another parameter pair could be rationalized on the basis of using only the 0.875 and 2.5 inch notched fracture curves. It is desirable, from the perspective of economy, to minimize the size and number of the fracture tests. Larger sized notches require larger test specimens which require larger, ever more expensive, test facilities and material supplies. If limited to the smaller two fracture test results, a combination ($l_{ch}$ = .3, $a_{22}$ = 600) can be selected. This parameter pair was selected to roughly match the larger 2.5 inch notched result while minimizing the error associated with the 0.875 inch notch. Assuming availability of only the two smaller notched fracture test data, this parameter pair is likely the best selection for extending the analysis to the 22.0 inch notched fuselage panel. It is recognized that this selection process is somewhat arbitrary. Hopefully future tests of the type described in Section 6.1 will make this process unnecessary.

As mentioned earlier, simulated fracture was assumed to coincide with the peak load associated with specimen resistance to extension. It was found that, for the damage parameter set ($l_{ch}$ = .3, $a_{22}$ = 600), peak load was realized with little area of damage for the smaller notched tests. However, the 12 inch notch test realized a significant area of damage at peak load as shown in Figure 6.9. The damage zone, as represented in Figure 6.9, is of a length that is roughly twice its width (approximately 2 x 0.8 inches). In either case, however, only a small increase in load was realized during damage growth. This is not to say that damage mechanics has little effect on fracture strength; rather, it has significant effect especially thru the nonlocal characteristic length parameter which dictates that a significant area of material must be elevated above the threshold strain

value before damage can initiate. After damage has initiated, the acute strain softening, represented by $a_{22}$ = 600, results in a somewhat rapid loss of load within the damage zone. A lower damage rate value would produce tougher results because, for the same nonlocal strain profile, greater resistance would be retained within the damage zone.

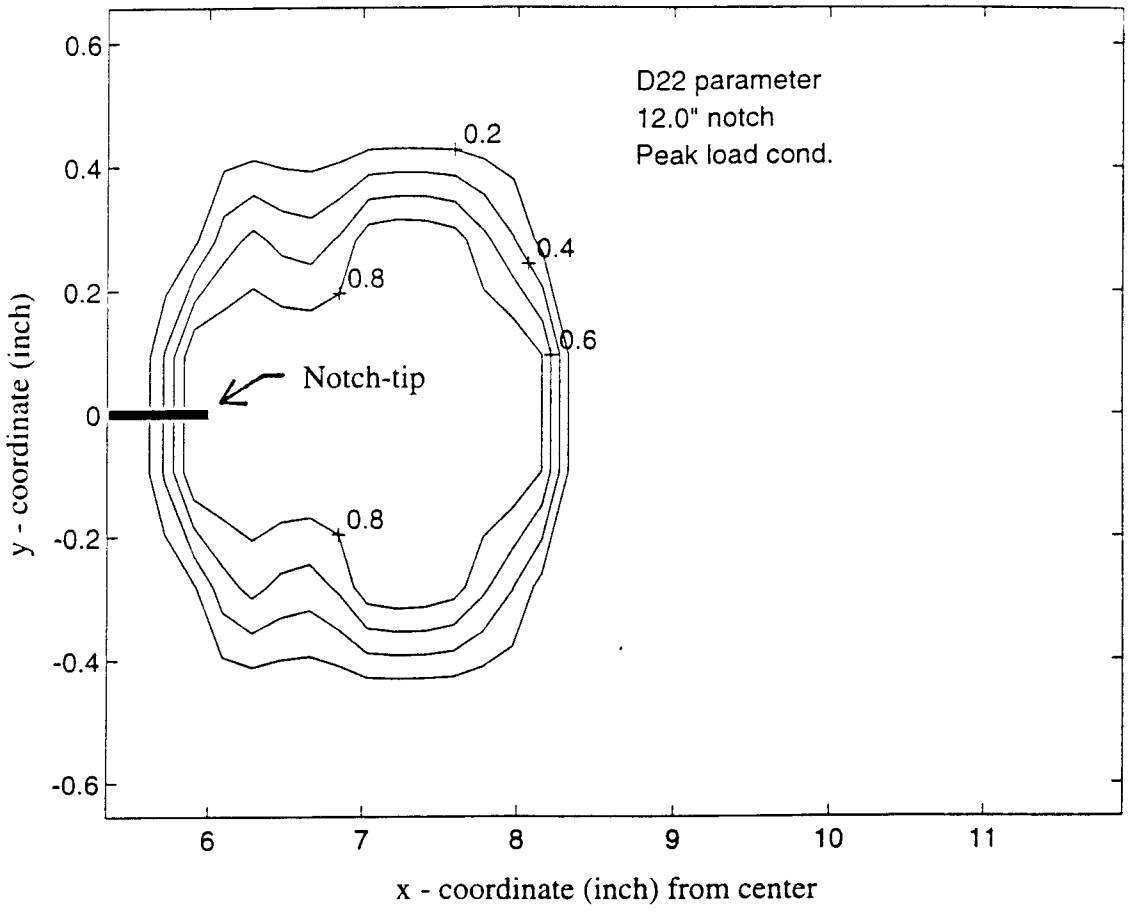


Figure 6.9 Damage Zone Contour Plot - Fracture of 12 inch Notch Specimen.

Predicted fracture strengths are plotted, against crack size and test results, in Figure 6.10. The damage model, based upon the parameter set ($l_{ch}$ = .285, $a_{22}$ = 150), shows good correlation with test results. Correlation of simulation to test results is quantified in Table 6.2.

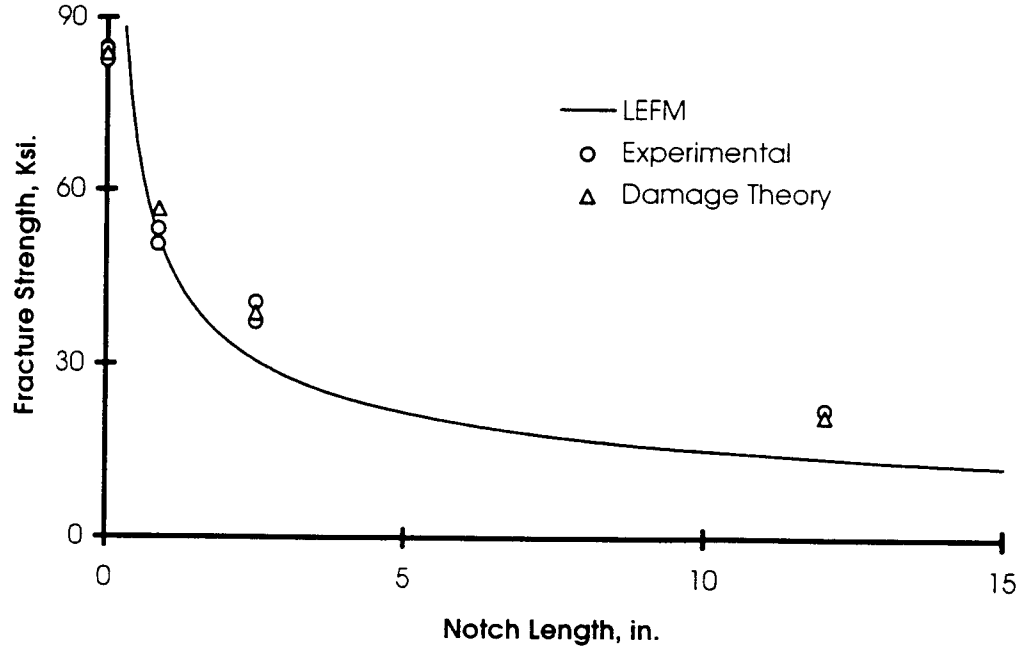


Figure 6.10 Predicted Fracture Strengths versus Test Results - Crown-3, Hoop Direction.

| | Damage Parameters | | Notch Length (inches) | | | |
|---|---|---|---|---|---|---|
| | $l_{ch}$ | $a_{22}$ | 0.00 | 0.88 | 2.50 | 12.00 |
| Damage Theory | 0.285 | 150 | 83.60 | 56.62 | 38.89 | 21.14 |
| Damage Theory | 0.300 | 600 | 83.60 | 54.76 | 38.33 | 19.78 |
| LEFM | NA | NA | Infinity | 51.90 | 30.57 | 13.95 |
| Test Average | NA | NA | 83.63 | 51.90 | 38.99 | 22.25 |

NA = Not Applicable

Table 6.2 Simulated and Tested Fracture Strengths.

Having established the characteristic length in favor of hoop simulation accuracy, the axial damage rate parameter can be selected on the basis of minimizing the error associated with axial-fracture simulation. A value of $a_{11} = 2000$ was identified.

## 6.3 Damage Characterization for Extension + Curvature Conditions

It was proposed, in Section 4.3, that curvature be the force behind growth of both the bulk mid-plane damage, $D^0$, and damage gradient, $\alpha$. Their functional relationships were proposed in equations (4-18) and (4-23), respectively. These functions introduced two new parameters, "$d_{ij}$" and "$v_{ij}$" respectively, that were intended to enable the correlation of simulation and tension plus flexural fracture (T+FF) test results. However, two such parameters cannot both be determined from a test in which their respective aspects of damage are indistinguishable. Nevertheless, the relative influence of each aspect can be qualitatively studied. Fracture simulation which suppresses the influence of curvature on the growth of $D^0$ would enable an influence study of the damage gradient and its parameter "$v_{ij}$". Likewise, suppression of the damage gradient would enable study of the $D^0$ dependence on curvature and its parameter "$d_{ij}$". Such an approach is presented below. It is expected that future efforts will relate the influences that curvature has on both the mid-plane damage and damage gradient such that only one rate parameter is needed to characterize the influence of curvature upon damage.

Fracture tests were again employed, to characterize damage under conditions of curvature, because unlike simple strength testing, fracture strength was expected to be sensitive to all aspects of damage growth. A pure bending strength test was expected to identify the threshold of curvature associated with damage initiation. This threshold value was utilized in equation (4-18) to define mid-plane damage, $D^0$, dependence on curvature. A direct measurement of curvature induced softening, like the sandwich tension technique of Section 6.1, is desirable. However, no such test method has been identified that can prevent localization of damage under flexural conditions and thereby induce a distributed failure of heightened sensitivity to damage characteristics. Instead, the T+FF test was developed that generated a broad field of uniform extension and curvature within a notched laminate. Such a test incorporated nonlinearities of both

material and geometric nature. No reference to this type of test has been identified in literature. Further description of the test can be found below in Section 6.3.1 with reference to further detail in Appendix B.

Unfortunately, no Crown-3 laminate was available for experimentation. However, two laminates, of very close relation to the Crown-3 laminate, were made available. These laminates, which are referred to as S6 and S7 laminates (consistent with ATCAS program designation), are of the same material batch, cure and layup as the Crown-3 laminate. However, differences in strength were realized and attributed to a reduction in laminate resin content (reduced thickness). The S6 and S7 laminates were subjected to conventional 2.5 inch center-notched hoop fracture tests by the Boeing company. The severed halves of these failed specimens were the laminate that was made available for further testing. Pulse echo, nondestructive examination, identified no internal delamination that could compromise further testing. S6 and S7 laminate strengths are listed in Table 6.1 for uniaxial tension loading. Results of the T+FF test of these laminates are presented below in Section 6.3.1. Unfortunately, no pure bending test was performed for determining a damage initiation threshold curvature. And no tension plus flexure strength test (no-notch test) was conducted which might have validated the assumed elliptic shape of the threshold interaction curve as defined in equation (4-18).

As explained above, simulation looked at the effects of curvature induced mid-plane damage growth separate from the investigation of effects of curvature induced damage gradient growth. Both simulations utilized the nonlocal definition of curvature which was calculated using the characteristic length $l_{ch}$ that was determined from results of the tension-only fracture tests. The influence of nonlocal curvature on mid-plane damage growth showed greater influence on fracture strength than did the influence on damage gradient. This is to be expected because mid-plane damage significantly effects both extensional and flexural stiffness within the damage zone while the damage gradient significantly effects only the extension-bending coupling stiffness, as discussed in Section 3. The influence of curvature on mid-plane damage, $D^0$, was principally

effected by the shape of the assumed elliptical threshold interaction curve. Results of these simulations are detailed in Sections 6.3.3 and 6.3.4.

Simulation of the T+FF test was based upon the nonlinear Finite Element Analysis (FEA) developed in Section 5. Unlike the tension-only fracture simulations however, simulation of the T+FF test incorporated a significant geometrically nonlinear effect. As shown in Figure 6.14, the simulation tracked very well the test's nonlinear load progressions.

Correlation between simulation and test results was made difficult by a deficit of fracture tests. Only two tests were performed on the S7 laminate: a tension-only 0.875 inch center-notched fracture test and a T+FF 0.875 inch center-notched fracture test. The T+FF test induced a far-field strain, about the notch, that was tensile through-out the laminate thickness so as to avoid crack closure complications. At failure, one surface strain was about twice that of the other. The T+FF test failed at an axial load 95.9% that of the tension-only test for the S7 laminate.

Three T+FF fracture tests were performed on the 0.875 inch center-notched S6 laminate specimens. The average failure of the T+FF test was 96.6% that of the tension-only test for the same specimen configuration. Simulation that modeled damage gradient growth could not account for this reduction in strength. Simulation of curvature induced mid-plane damage growth produced results similar to that of the tests and exact correlation could be possible if given the test support necessary to quantify the damage parameters.

### 6.3.1 Test Results

The Boeing Company had provided experimental strengths of the S6 and S7 laminates for tension-only fracture as listed in Table 6.1 (Walker et al., 1996). Boeing further provided to Oregon State University the severed halves of these failed specimens from which 0.875 inch notched fracture specimens and uniaxial tension strength

specimens were manufactured. The tension-only strength and fracture results are listed in Table 6.1. Based upon the experimental data of Table 6.1, a comparison of S6 and S7 fracture strengths with that of the Crown-3 laminate indicates that the S6 laminate and especially the S7 laminate were significantly less damage tolerant. Both the S6 and S7 laminates were intended to duplicate the Crown-3 laminate but due to differences in layup machinery, prepreg age and resultant laminate resin content, exact duplication was not achieved. The material batch, layup and cure process were identical for all three laminates.

A novel tension plus flexure fracture (T+FF) test was developed and tests were performed on the S6 and S7 laminates. The test utilized the conventional center-notched fracture specimen design. Specifically, the specimens incorporated a 0.875 inch notch and a width of 4 inches. A simple illustration of the T+FF test is shown in Figure 6.11. Specimen extension was forced using an Instron screw-drive test machine. Specimen curvature was generated via the common 4-point bend approach using the transverse load and bridge structure shown in Figure 6.11. This load was generated by a small hydraulic actuator and monitored using a custom made, ring type, load cell. The transverse load was introduced to the test specimen through a platform which contacted the specimen using two rods separated by one inch, which spanned the specimen notch.

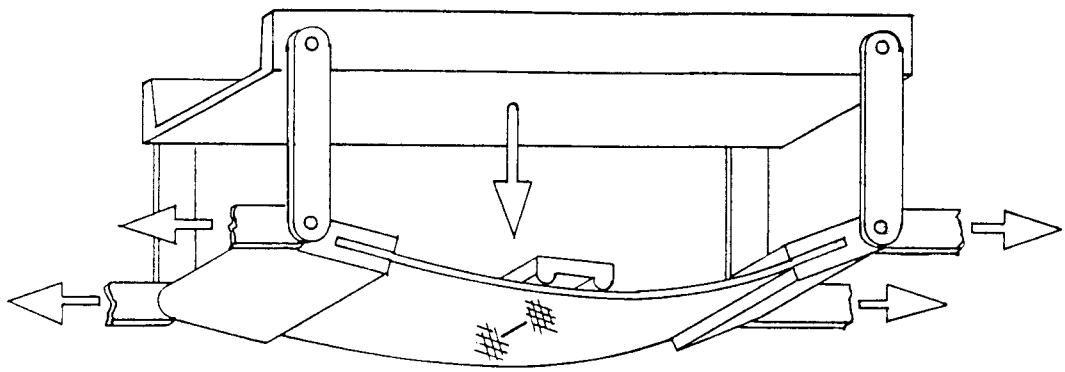

Figure 6.11 Illustration of Combined Tension Plus Flexure Fracture (T+FF) Test.

Such a 4-point bend approach, and simultaneous Instron machine control, generated a uniform field of combined tension plus flexure (no transverse shear) across the specimen notch area. A photograph of the test assembly is shown in Figure 6.12.

It was desired to generate a tension dominant state of strain within the specimen such that flexure was not so great as to induce compression and associated crack closure. Such a load condition is relevant to that realized by fuselage crown structure. Two methods of load control were experimented with; the more simple approach also required less performance of the load actuator system. This test was conducted upon three S6 fracture specimens to produce the nonlinear curvature versus mid-plane strain trajectories shown in Figure 6.13. A summary of the S6 laminate test results are listed in Table 6.3. The test was also performed on a single S7 laminate specimen. Additionally, a tension-only fracture test was performed on an identical S7 specimen and simple uniaxial tension strengths were tested for both laminates. A summary of these test results as well as load cell and strain gage data plots can be found in Appendix B.

As suggested by the strain trajectories shown in Figure 6.13, the T+FF test included two load intervals. First tension-only load was applied up to approximately 75% of the specimens fracture strength. At this point, the Instron cross-head position was fixed and the transverse hydraulic load was actuated. The resultant curvature was coupled with increasing tension due to the nonlinear geometric effects associated with such loading of an axially constrained plate. As indicated in Figure 6.13, some curvature developed in the specimen during the initial interval of axial loading. This effect, although not detrimental to meaningful test results, was not desired. The cause of such drift is thought to be associated with the use of single-shear grips for holding the specimen's ends. Single shear clamps lack the self-aligning property of double-shear grips. For this reason, double-shear grips are typically used. The bolted single shear grip assembly included shimming for attaining the desired axial load alignment; but this proved cumbersome and was likely insufficient. The single-shear grip was used because it could be fashioned in a more compact design for use in the limited work space offered by the Instron machine.

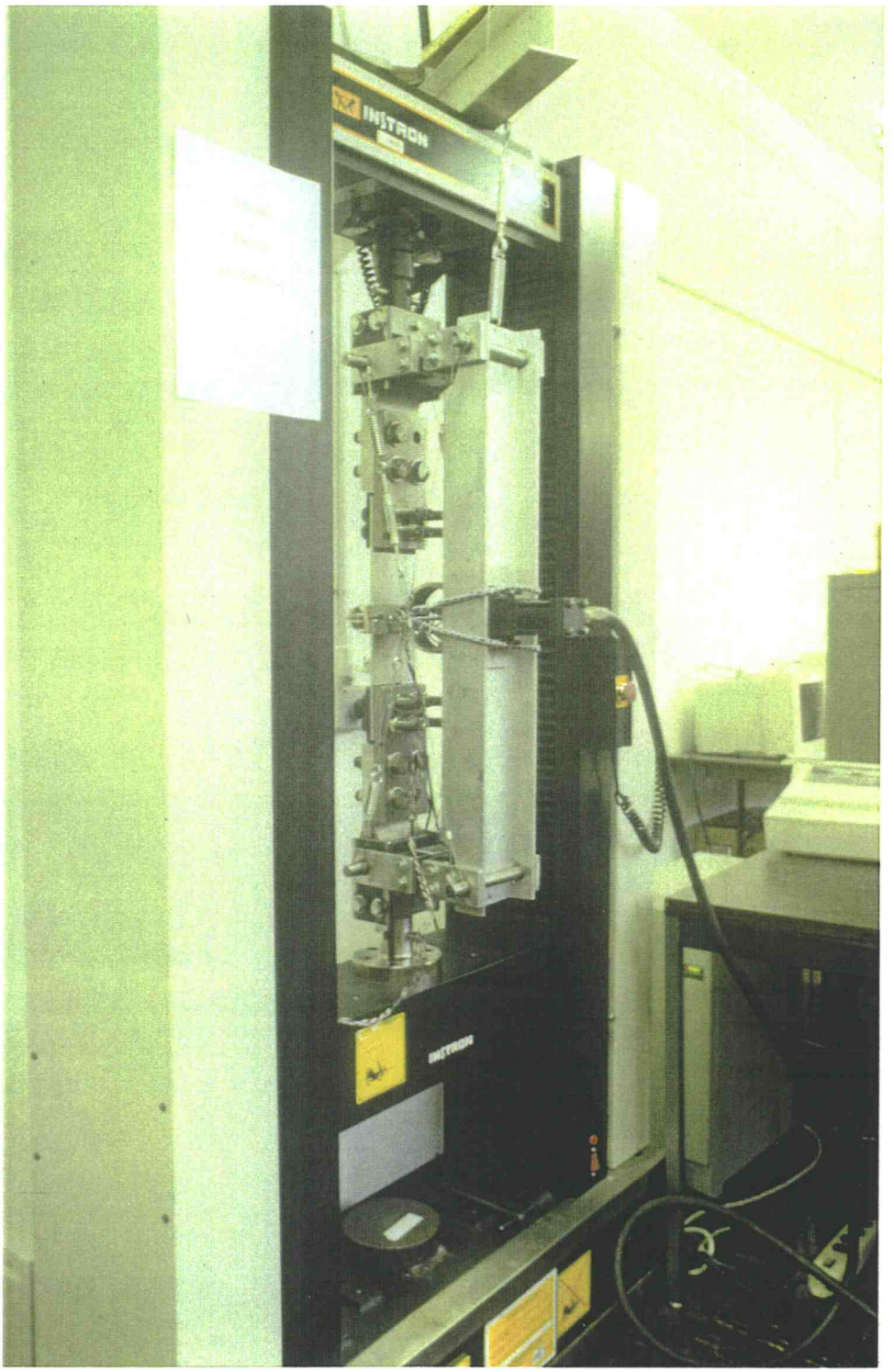


Figure 6.12 Photo of Tension plus Flexure Fracture (T+FF) Test Assembly.

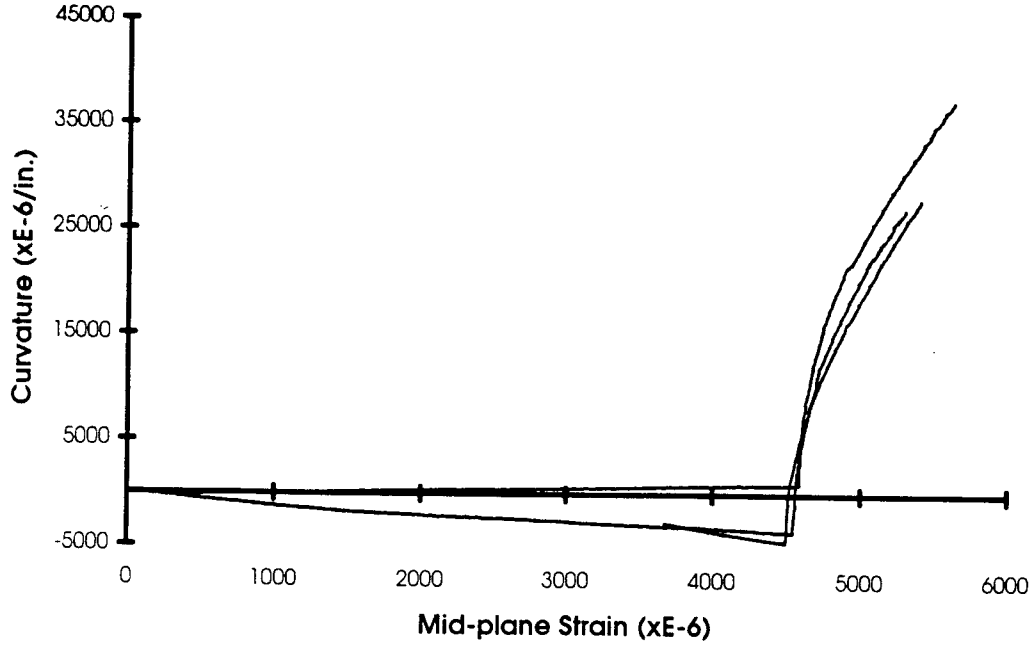


Figure 6.13 Far-field Strains Generated by three Tension plus Flexure Fracture (T+FF) Tests (S6 Laminate).

| Laminate Coupon | Notch Length (in.) | Width (in.) | Thickness (in.) | First Audible Damage Load (Kips) | Cross-head Lock Load (Kips) | Axial Failure Load (Kips) | Trans. Failure Load (Kips) | Far-field Mid-plane Failure Strain (xE-6) | Far-field Failure Curvature (xE-6/in.) |
|---|---|---|---|---|---|---|---|---|---|
| S6-2 | 0.862 | 3.970 | 0.093 | 11.60 | 14.00 | 16.21 | 1.48 | 5290. | 27050. |
| S6-5 | 0.862 | 3.970 | 0.093 | 10.30 | 14.00 | 16.92 | 1.70 | 5390. | 27960. |
| S6-6 | 0.863 | 3.960 | 0.093 | 11.30 | 14.00 | 16.95 | 1.81 | 5620. | 37350. |
| S7-1 | 0.864 | 3.987 | 0.090 | 11.40 | 12.05 | 15.41 | 1.73 | 5030. | 37244. |

Table 6.3 Summary of S6 Laminate T+FF Test Results.

Another load control approach was tested which proved both more complicated and required greater stroke length than was available in the hydraulic actuator. It also began by axially loading the specimen up to some high percentage of its fracture strength. However, in this approach the cross-head position is controlled, while the transverse load was applied, in order to maintain a constant axial load. That is, the Instron cross-head position was adjusted to negate the nonlinear interaction noted in the other test approach. Such a control required somewhat sophisticated feedback control of the Instron machine. This was accomplished by a program based upon the LabView symbolic simulation and control software. This test control approach also required greater stroke length of the transverse load actuator in order to fail the specimen. The small actuator employed offered only a 1.0 inch stroke. Such a compact actuator was needed to minimize the weight and size of the T+FF test assembly so as to render its frequent installation and removal form the Instron machine a manageable job for one person.

### 6.3.2 Simulation - Nonlinear Finite Element Analysis

The T+FF test was simulated using the nonlinear finite element analysis (FEA) defined in Section 5. A model was developed which expanded upon that used for simulating the tension-only test. Specifically, geometric nonlinearity was addressed and the compliance of the axial load introduction assembly also had to be modeled. As before, displacement control was employed and failure was associated with a reduction of resistance to deformation.

Transverse loading of an axially constrained plate is a classic problem of geometric nonlinearity. Should transverse deformation exceed one-tenth of the plate thickness, the problem is considered geometrically nonlinear. The transverse deformation in the T+FF test was on the order of 100 times that. Being axially constrained, the imposition of curvature must also impose a simultaneous stretch. To

address this aspect of the problem, total Lagrangian formulation, of the deformation relations, was employed to account for large deflections and moderate rotations. FEA results, for a simple geometrically nonlinear pin-pin beam problem, compared very well to solutions using the commercial FEA program COSMOS/M.

The axial deformation of the fracture specimen was controlled by movement of the Instron cross-head. Linkages joined the T+FF test assembly, of Figure 6.11, to the Instron cross-head above and to its foundation below. These linkages ensured that no moment load was introduced to the test assembly and that a single line of action existed between the assemblies attachment to the Instron foundation and cross-head. However, the linkages introduce compliance into the system such that the locking of the cross-head position does not lock the axial separation between the hinges of the T+FF test assembly. Rather, some small axial displacement is possible. This compliance had to be modelled in order to simulate the nonlinear interaction between the applied transverse load and induced axial tension.

The same finite element mesh, shown in Figure 6.2, was used to represent the fracture specimen. This mesh was expanded to model the specimen grips which connected the specimen to the hinge. Details of the grip, such as fasteners and its single shear load transfer, were not considered critical. The grip stiffness was large and was modeled as such. The mesh was further extended to model the axial linkage assembly and its compliance. The actual stiffness of the linkage assembly was not known. Instead, its stiffness was varied until the simulated nonlinear load response matched that of the test. Such a correlation is only possible prior to the initiation of damage and associated material nonlinearity. The excellent match between simulation and test is evident in Figure 6.14.

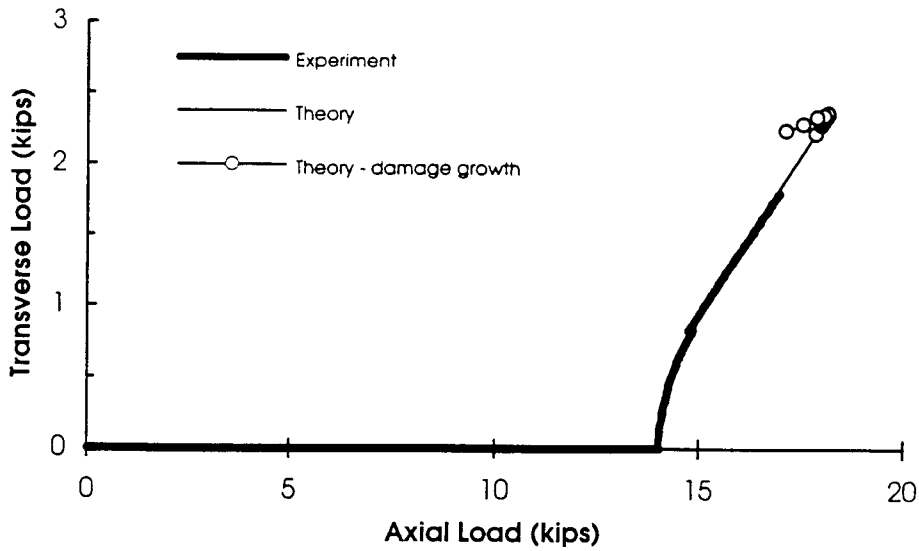


Figure 6.14 Simulated and Tested Transverse versus Axial Load Path - Tension plus Flexure Fracture Test.

### 6.3.3 Results of Simulation Study

Simulation was performed only for fracture tests of the S6 laminate. First the laminate stiffness and tension-only fracture properties had to be established using the method detailed in Section 6.2. The S6 laminate hoop stiffness and the damage threshold hoop strain, $\varepsilon_{22}^{cr}$, were obtained from uniaxial tension tests (see Appendix B). The resultant threshold hoop strain was found to be $\varepsilon_{22}^{cr} = 0.00975$. Simulation of the tension-only fracture test enabled characterization of the nonlocal characteristic length, $l_{ch}$, and mid-plane damage rate parameter, $a_{22}$ as defined in Section 6.2. Correlation of simulation with test results, for the 2.5 inch center-notched specimen, enabled the definition of a parameter solution set represented by a single curve in the space of $l_{ch}$ and $a_{22}$. Such a solution set does not suggest any single parameter pair as being best. Therefore, the rate parameter was selected as being equal to that of the Crown-3 laminate and the corresponding characteristic length was then quantifiable. The S6 laminate tension-only damage parameter pair was thus established as ($l_{ch}$ = .226 inches, $a_{22}$ = 600).

It is desirable to compare results of the T+FF test to that of the tensile-only test using the same specimen size. The T+FF test was performed on a specimen of S6 laminate, having a 0.875 inch notch and a 4 inch width. Unfortunately, no tension-only fracture test was performed for this notch size. The simulated 0.875 inch notch tension-only fracture strength was 18.12 kips based upon damage parameters determined from the 2.5 inch notch fracture test results. It is likely that this value of strength would over-predict an experimentally determined 0.875 inch notch fracture strength. This expectation relates to the over-prediction of strength realized in Section 6.2 for the 0.875 inch notch specimen of Crown-3 laminate as listed in Table 6.2. If a similar trend is assumed for the S6 panel, a tension-only fracture test, of the 0.875 inch center-notched specimen, would have resulted in a strength of 17.28 kips. For the same specimen, the average T+FF fracture strength was 96.6% of this value. Both the T+FF and the tension-only test conditions were tested for the S7 laminate and a 95.9% retention of tensile strength was realized.

As previously stated, the effects of curvature, upon the growth of mid-plane damage and the growth of damage gradient, must be considered separately. Therefore, a simulation of the T+FF test was conducted using a model for which curvature affected only the mid-plane damage growth according to equation (4-18). No damage gradient was allowed to evolve. The damage threshold curve, defined in the space of nonlocal mid-plane strain and curvature, was assumed elliptical and defined using $\varepsilon_{22}^{cr}$ and $K_{22}^{cr}$ as its axis intercepts. As mentioned above, $\varepsilon_{22}^{cr}$ was determined from a uniaxial tension test. No uniaxial pure bending test were conducted to quantify $K_{22}^{cr}$. Rather, an estimate was made of $K_{22}^{cr}$ corresponding to that curvature which induced a fiber strain equal to $\varepsilon_{22}^{cr}$ according to Classical Laminated Plate Theory (Jones, 1975). This equated to a damage threshold curvature of $K_{22}^{cr}$= +/- 0.2928 (1/inch).

After exceeding the elliptical threshold interaction curve, simulated growth of the mid-plane damage is controlled by the damage rate parameter, $a_{22}$ = 600, and parameter "$d_{22}$" of equation (4-18). Parameter "$d_{22}$" represents the deviation of curvature damage rate from that of mid-plane strain damage rate. A value of zero refers to no difference.

A negative value refers to a higher curvature induced damage rate. Simulations of the T+FF test were performed in which the value of parameter "$d_{22}$" was varied. Results, listed in Table 6.4, show a simulated retention of 97.3% of tension strength, for the value $d_{22}$ = -.5. As shown in Figure 6.15, this value of "d" induced the greatest pure curvature damage growth rate. The mid-plane damage surface, corresponding to equation (4-18) but specific to the S6 laminate, is shown in Figure 6.16. The asterisk, identified on this surface, represents the damage and strain coordinate for a material point within the damage zone at the point of maximum load restraint (i.e. failure). The complete history of this material point is traced as the dashed line in Figure 6.17. This contour plot, of the mid-plane damage, shows the damage threshold ellipse as the solid line. Again, an asterisk identifies the point of specimen failure. Because the test condition was one of tension dominance, the damage rate corresponding to mid-plane strain was dominant; that is, parameter $a_{22}$ was dominant over $d_{22}$.

| Curv. Damage Param. d | Tension Damage Param. a | Characteristic Length l | Max. Tension Load (Kips)** | Max. Transverse Load (Kips) |
|---|---|---|---|---|
| 0.5 | 600 | 0.226 | 17.65 | 2.15 |
| 0 | 600 | 0.226 | 17.65 | 2.15 |
| -0.5 | 600 | 0.226 | 17.63 | 2.14 |

** Compare to simulated tension-only failure load = 18.12 Kips.

Table 6.4 Simulated T+FF Test Strengths - Curvature Induced Mid-Plane Damage, $D^0$, Modeled.

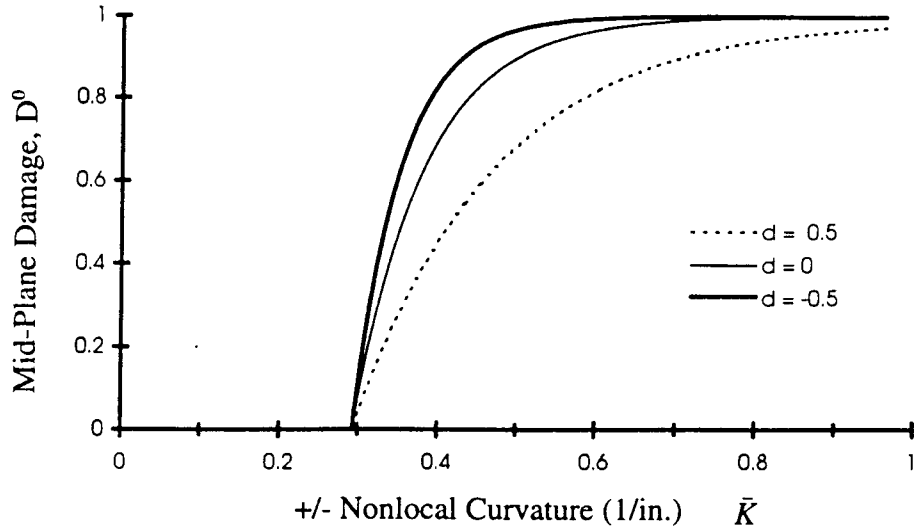


Figure 6.15 Effect of "$d_{22}$" on Pure Bending Mid-plane Damage Growth Function.

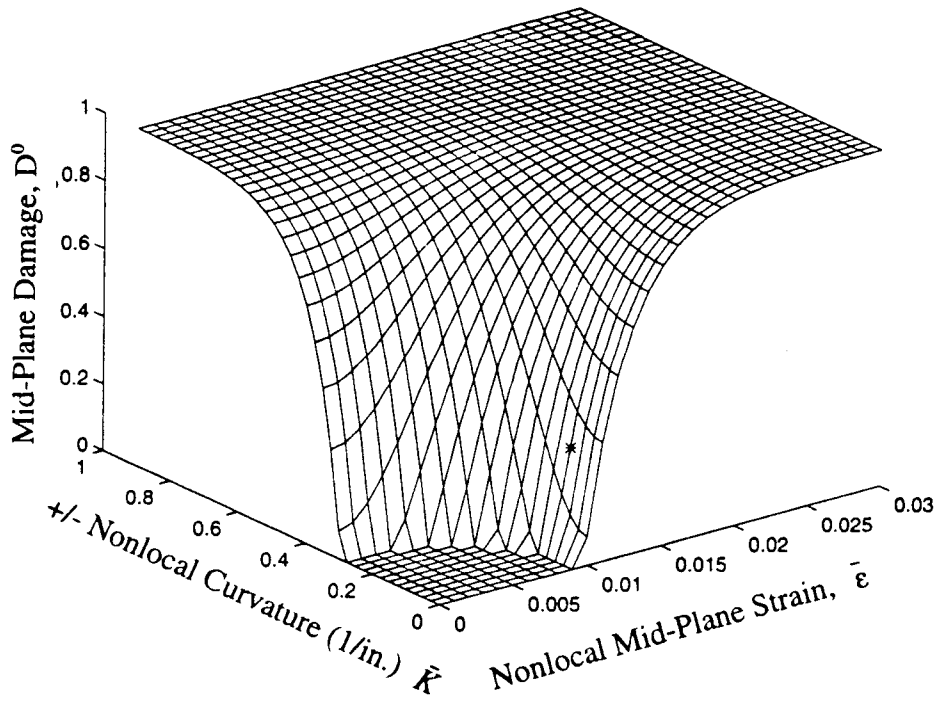


Figure 6.16 Mid-plane Damage Surface for the S6 Laminate (* = condition within Fracture Process Zone at failure)

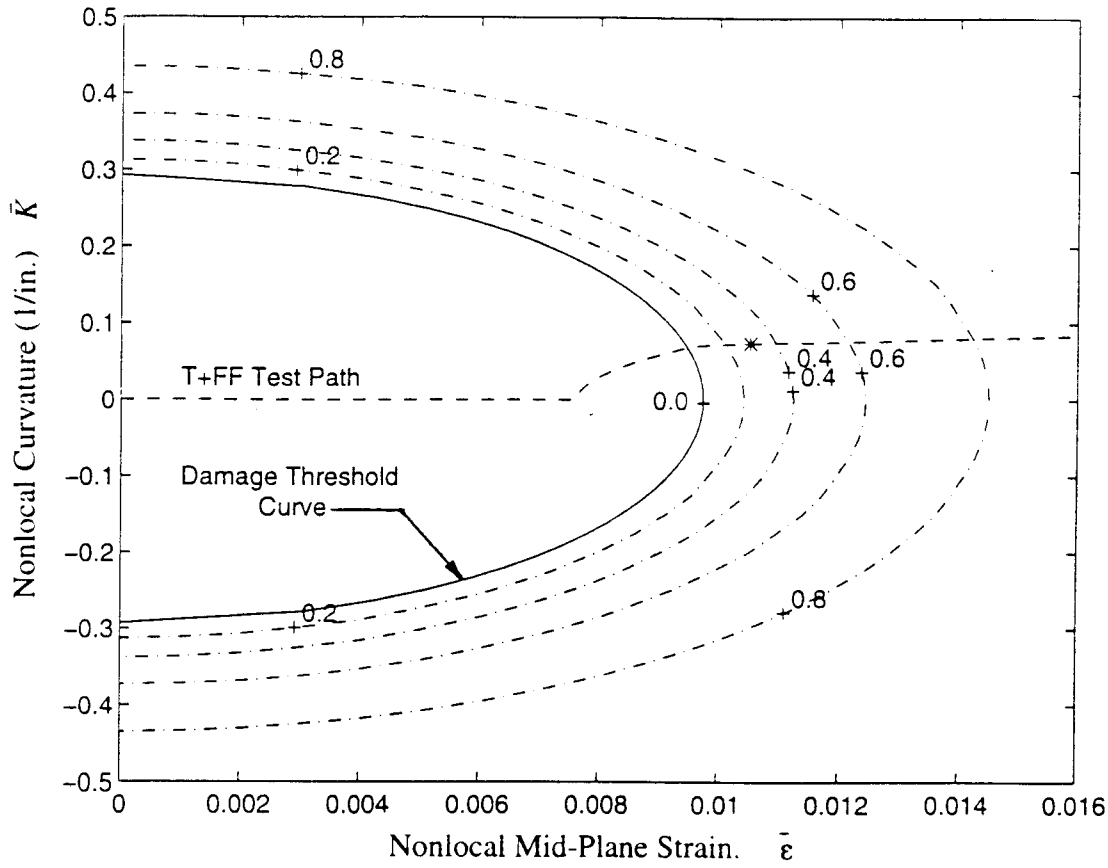


Figure 6-17 Panel S6 Mid-plane Damage Function and Simulated Trajectory of Material Point within Fracture Process Zone for T+FF Test Conditions (* = failure condition)

Simulation of damage gradient growth effects was also performed on the T+FF test. The gradient, $\alpha_{22}$, was simulated to grow relative to the state of curvature, $K_{22}$, and damage compliance, $S_{22}$ (see Figure 4.8), according to equation (4-23). No effect of curvature, upon mid-plane damage $D_{22}^{0}$, was allowed. Two values of parameter $v_{22}$ where utilized for simulation, $v_{22}$ = -100 and -85. Results, listed in Table 6.5, show little difference from the simulated tension-only fracture strength. Also, it turns out that the damage gradient, for material within the damage zone (i.e. fracture process zone), far exceed the permissible range defined by Figure 3.1. Damage growth trajectories are

plotted in Figure 6.18 for a sample point within the damage zone. It should be noted that although the permissible range of damage is initially violated, further growth corrects the problem. The suddenly high value of damage gradient is a result of the damage compliance term, S, shown plotted in Figure 4.8. A third simulation was conducted in which artificial control was imposed upon the gradient growth by not allowing it to exceeded the permissible region of Figure 3.1. Results of this "limit controlled" analysis are also plotted in Figure 6.18 and its fracture strength result is listed in Table 6.5.

According to the simulated T+FF results in Table 6.5, the effects of modeling a damage gradient are minor or non-existent, especially when constrained to comply with the permissible damage range of Figure 3.1. Maximum load (i.e. failure) corresponded to a damage zone in which the mid-plane damage ranged from 0.0 to 0.3 for the 0.875 inch notch test. Referral to Figure 6.18 shows that the corresponding range of damage gradient was very active within the damage zone at failure. Its corresponding effect upon the extension-bending coupling stiffness, $\tilde{B}_{22}$, is illustrated in Figure 3.3. Apparently the uncontrolled gradient simulations developed extension-bending coupling far in excess of what was permissible. The controlled simulation attained a coupling of about ⅔ the maximum permissible. Therefore all three simulations generated a significant damage gradient effect within the damage zone; however, its effect upon fracture strength was minimal. The simulated S6 laminate fracture represents behavior of a brittle material. For materials that exhibit slower damage growth, a larger active damage zone would develop prior to failure. The damage gradient would have a greater opportunity to affect fracture strength for such materials.

| Curvature Damage Gradient Parameter v | Gradient Control . | Tension Damage Param. α | Characteristic Length l | Max. Tension Load (Kips) ** | Max. Transverse Load (Kips) |
|---|---|---|---|---|---|
| -85 | None | 600 | 0.226 | 17.95 | 2.28 |
| -100 | None | 600 | 0.226 | 18.02 | 2.31 |
| -100 | Limit * | 600 | 0.226 | 18.13 | 2.36 |

* Gradient limited to permissible range detailed in Figure 3.1

** Compare to simulated tension-only failure load = 18.12 Kips

Table 6.5 Simulated T+FF Test Strengths - Curvature Induced Damage Gradient, α, Modelled.

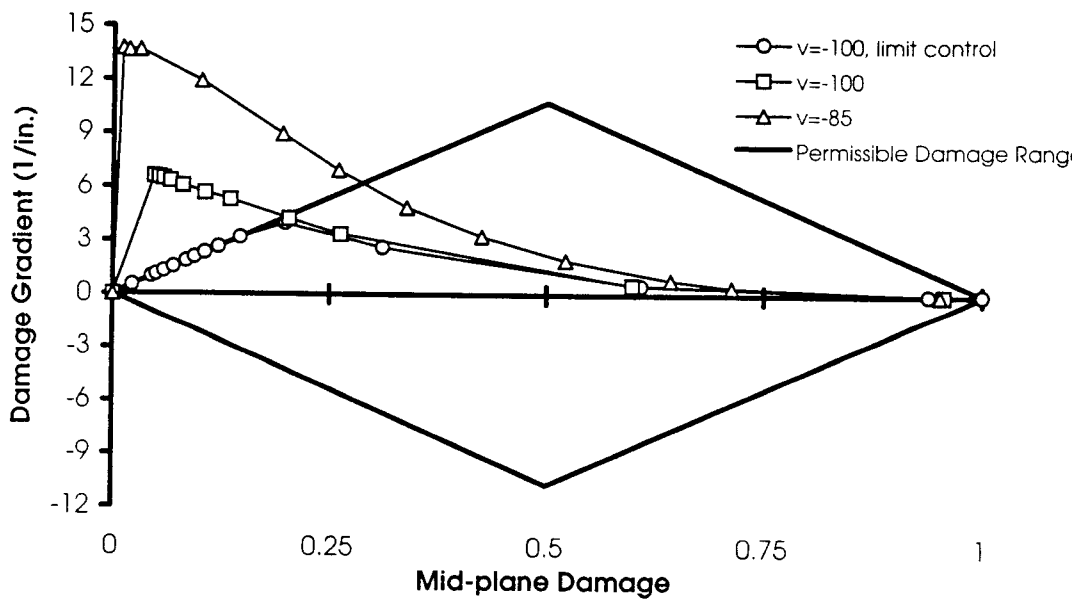


Figure 6.18 Damage Gradient versus Mid-plane Damage Growth, within the Fracture Process Zone, for Three Gradient Controls

# 7. Fuselage Damage Tolerance

A section of commercial airplane fuselage, shown in Figure 7.1, was analyzed and tested for hoop directed damage tolerance. Its design represented fuselage crown structure (top quadrant). Testing provided experimental data regarding the response of complex structure to progressive damage (Walker et al., 1996). Strain gage data suggests that significant notch-tip damage began at 83% of the final failure pressure. Post failure inspection revealed large-scale debonding of the skin from the frame members. Damage theory analysis, using the previously established damage parameters, predicted failure pressures that were between 8 and 10 percent below that of the test failure pressure.

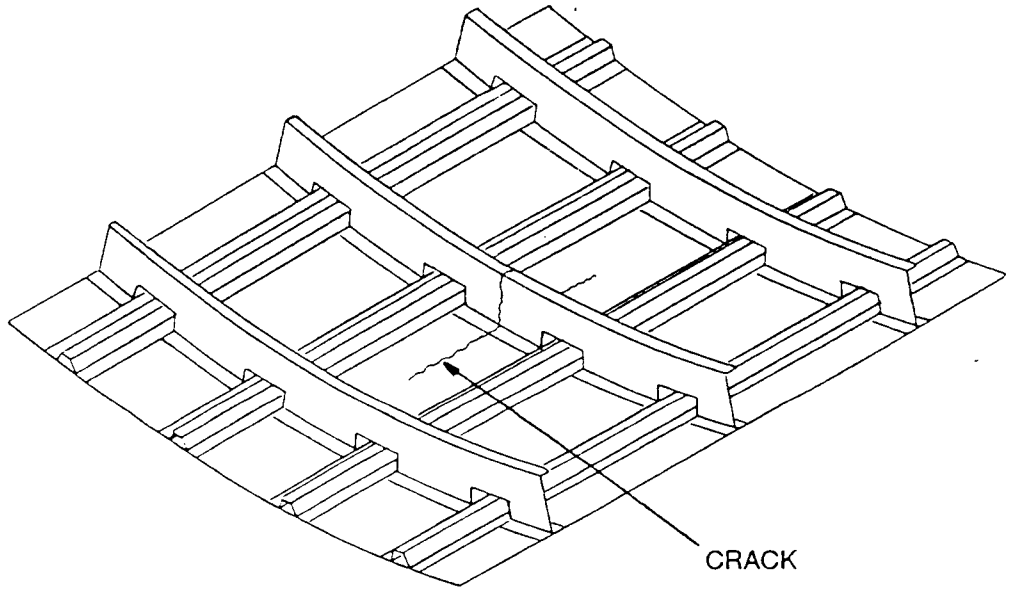


Figure 7.1 Fuselage Crown Panel Test Article.

The panel represents a section of large diameter fuselage (122 inch outer radius). The skin is reinforced with J-shaped frames running circumferentially and hat-shaped

stringers running axially. A 22 inch crack runs axially from the center of one bay to the center of its neighbor, severing both the skin and a frame member. The skin, referred to as the Crown-3 laminate, was previously defined in Section 6. The stringers are composed of a 15-ply laminate of graphite/epoxy (0.110 inch thick) with a [45/90/-45/0/45/-45/0/90/0/-45/45/0/-45/ 90/45] lay-up. Its lamina stiffness properties are $E_1$ = 19.6 Msi, $E_2$ = 1.36 Msi, $G_{12}$ = 0.72 Msi, and $v_{12}$ = 0.32. The frame members are composed of a woven graphite/epoxy with a thickness of 0.115 inch and moduli $E_1$ = 6.23 Msi, $E_2$ = 8.89 Msi, $G_{12}$ = 1.66 Msi, and $v_{12}$ = 0.144.

The panel was constrained in the circumferential direction but not longitudinally; so that when pressurized, no axial load developed. Such a condition was the most severe possible from the perspective of hoop fracture and represented fuselage pressure loading plus axial compression due to flight maneuver loading. The fuselage damage tolerance requirement, for such a condition, specified that 8.85 psi be supported (Walker, 1993).

Testing was conducted at NASA LaRC and utilized a pressurized box, the top of which was covered and sealed by the fuselage panel. Pressure was generated in a static manner except that once depressurization was sensed, the pressure control valve was fully opened to maintain as much pressure upon the failure process as possible. Such control should better represent the pressure capacity of the total large-diameter fuselage.

The crown panel failed at a pressure of 9.29 psi. Strain gage data had been collected from which a damage history can be surmised. Some doubt is healthy in interpreting such data because damage events can release energy sufficient to compromise strain gage integrity. Gage sensitivity and vulnerability was obviously greatest closest to the notch tip. Gages were placed ahead of both tips of the notch (designated tip A & B). Prior to any evidence of damage, strain gage data indicated that tip-A was only slightly more strained than tip-B. At 5 psi, the gage closest to tip-A (approx. 0.1 inch ahead of tip) registered a damage event. A second gage, 0.39 inches ahead of tip-A, registered its initial damage event at 7.1 psi. At 8.2 psi, damage was registered broadly in that tip-B showed damage in gages located at 0.10, 0.39 and 4.0 inches ahead of the tip. The gage 4.0 inches ahead of gage-A also registered its initial

damage event at 8.2 psi. Post-failure analysis suggested that a final damage zone of about 1.5 inches was developed at failure. Such analysis also identified large scale debonding of the circumferential frame members from the skin. The damage that originated at the notch tip was found to have traveled across and beyond the debonded frame members to the fasteners that attached the axial load introduction doublers at the panel edge. Examination of strain gage data suggests that the skin did not debond from the circumferential frames prior to failure. That is, the skin probably debonded from the frame during the dynamic advance of the notch. Such behavior is not desired since an attached frame can serve to arrest the notch growth. Loss of such a fail-safe feature suggests that fasteners are needed to join the skin laminate to frame members.

Simulation, of panel failure, incorporated both tension and flexural damage characteristics as developed in Section 6. Two sets of damage parameters were exercised as listed in Table 7.1. As described in Section 6.2.3, one set (case 1) was selected to best correlate with the two smaller and cheaper tension fracture tests; the other set (case 2) employed results of all three tension fracture tests. Both selections included a bias toward correlation with the larger notch size. Case-2 was expected to better simulate fuselage damage tolerance because it had the benefit of the largest, 12 inch notch, fracture test. Case-1, however, reflected a limited test data-base that is more typical of what could be afforded by a product development program. It is also indicated in Table 7.1 that the dependence of mid-plane damage upon curvature was not simulated. Rather, the curvature induced damage gradient was incorporated in both simulation cases using the limit control scheme described at the end of Section 6.3.3. This segregation of curvature induced damage effects followed the approach described in Section 6 and further discussion is reserved for the end of this section.

Simulation employed the nonlinear finite element method described in Section 5. The model, shown in Figure 7.2, defines only one-quarter of the panel by taking advantage of two axis of deformation symmetry. The complete upper half of the fuselage circumference was included in the analysis so at to minimize artificial edge effects upon simulated internal load distribution, deformation and damage growth. The

panel test was also designed to minimize edge effects but physical limitations were imposed by cost driven size considerations. The model does not attempt to represent the test hardware directly; but rather, it represents the actual fuselage which the test hardware attempts to mimic. Large deflection analysis capability was applied to the fuselage as suggested by Riks et al. (1989). As with the previous fracture tests, viscous-damping dynamic analysis enabled stable solution convergence. Simulation was controlled by a constant rate of increase in pressure load. Failure was assumed to occur at a pressure load corresponding to a sudden acceleration in radial deformation. This acceleration was experienced across the full length of the test model to varying degrees. Such an acceleration refers to a transition from static to dynamic crack growth. It was assumed that the onset of dynamic crack growth could be equated with panel failure. This assumption would not be valid if damage growth were arrested at its nearest circumferential frame member. However, such damage arrest was not identified in the test probably because the frame debonded from the skin (no fasteners were employed).

| | Nonlocal Characteristic Length (in.) | Tension Damage Rate Parameter a | Curvature Mid-plane Damage Parameter d | Curvature Damage Gradient Parameter v | Failure Pressure (psi) |
|---|---|---|---|---|---|
| Simulation Case - 1 | .300 | 600 | Not modelled | -100 | 8.34 |
| Simulation Case - 2 | .285 | 150 | Not modelled | -100 | 8.5 |
| Test Results | NA | NA | NA | NA | 9.29 |

NA = Not Applicable

Table 7.1 Simulation Case Parameters and Predicted versus Experimental Failure Pressure.

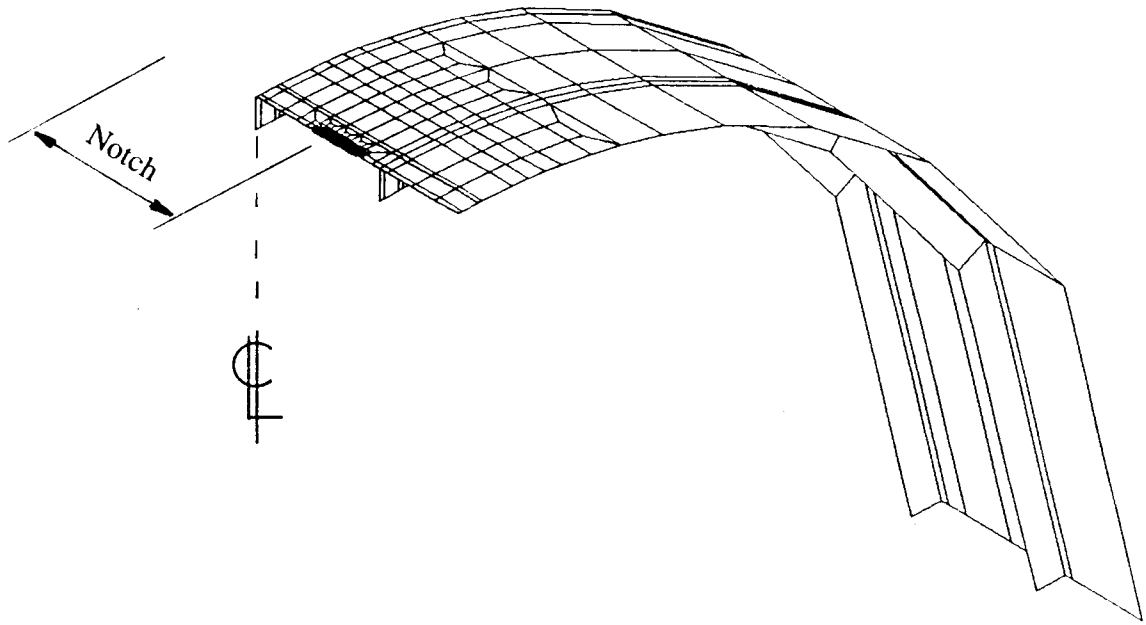


Figure 7.2 Finite Element Model - Fuselage Crown Panel.

Case-2 simulation resulted in radial acceleration at a pressure of 8.50 psi as shown in Figure 7.3. Case-1 registered failure at 8.34 psi in a similar manner. These results were 8.5 and 10.2 percent conservative respectively. The size of the damage zone at failure were 0.60 and 0.45 inches respectively. These sizes are relatively small in comparison to the 1.5 inch size reported by post-test examination and in comparison to the 2 inch size realized in simulation of the 12 inch fracture tests.

Strain was monitored during the test at several locations ahead of the crack tip. A comparison of measured strain on the outer surface of the panel and that of the case-2 simulation is available in Figure 7.4 for two locations (x) ahead of the notch-tip. Excellent agreement is evident between simulation and test prior to development of damage. This implies that the large deformation geometric nonlinearity was successfully modelled. Test damage may have begun at 5 psi for notch tip-A but tip-B waited until 8.2 psi. Simulation registered the initiation of damage at 8.3 psi, followed shortly thereafter by dynamic crack growth. Test failure was registered at 9.29 psi. The

developed theory does not pretend to model dynamic crack growth; instead, it signals the transition from static to dynamic behavior which is assumed to represent panel failure.

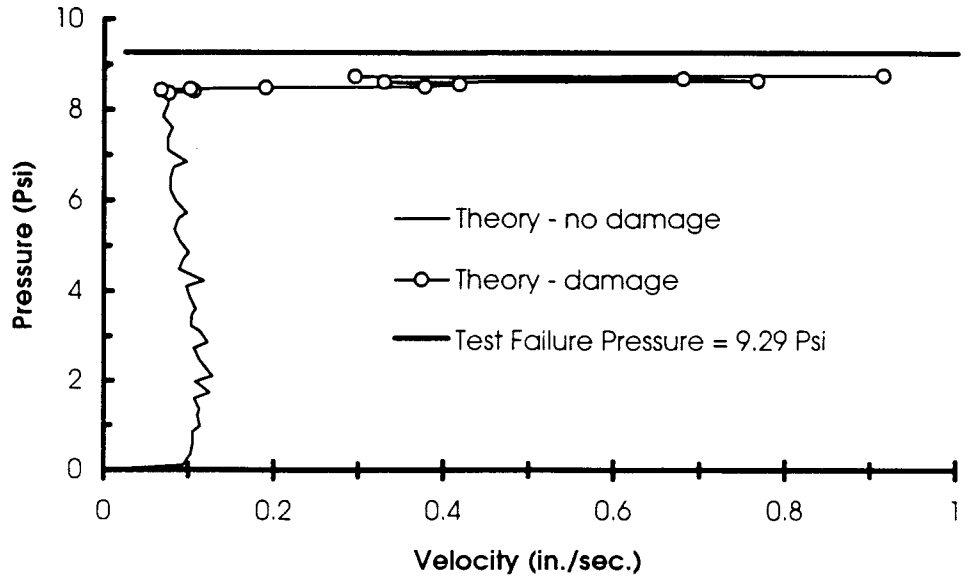


Figure 7.3 Pressure vs. Velocity Curve for Point on the Crack Surface.

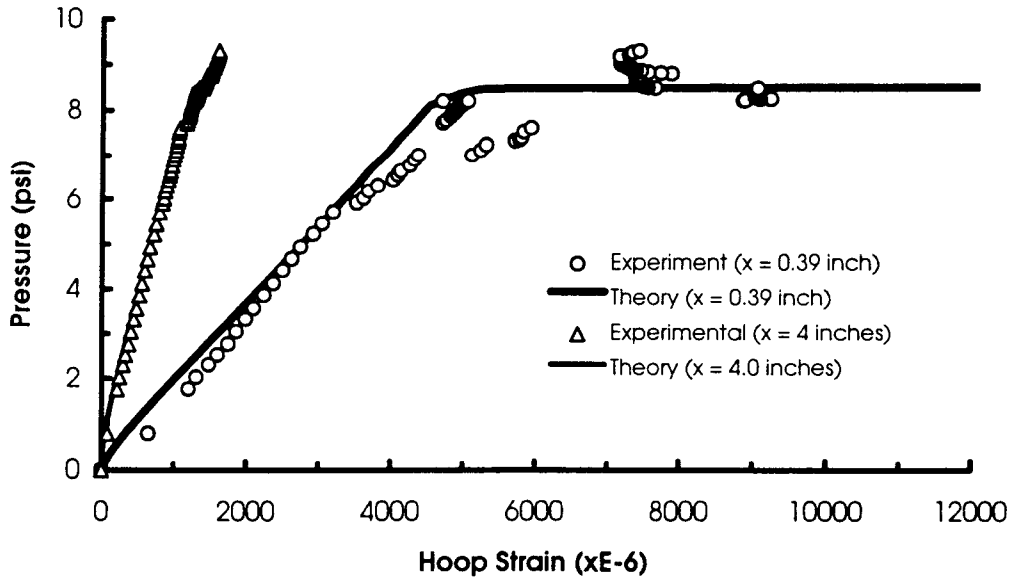


Figure 7.4 Pressure vs. Strain ahead of Notch-tip, Strain Gage Data versus Simulation.

As mentioned above, only one aspect of curvature induced damage was modeled, the damage gradient. It was characterized using the parameter $v_{22} = -100$ along with the limit-control scheme which was adopted from the results of the S6 laminate study of Section 6.3.3. The dependence of mid-plane damage upon curvature was not simulated. Results of Section 6 indicated that the modelling of damage gradient growth has negligible effect upon predicted fracture strength and therefore the predicted failure pressures were probably insensitive to the induced curvature. The tension plus flexure fracture testing of the S6 laminate showed curvature to reduce the tensile component of fracture strength by about 4%. The comparison of simulated nonlocal strains within the damage zone of the S6 laminate T+FF test with that of the Crown-3 panel pressure box test, shown in Figure 7.5, indicates that the panel realized about ⅔ the curvature of the T+FF test. It could thus be expected that the panel would realize a curvature induced fracture strength reduction of less than 4%. Section 6 indicated that the modelling of curvature induced mid-plane damage could account for such a strength reduction. Unfortunately, due to a lack of test support and time, the fuselage panel was not analyzed for curvature effect upon mid-plane damage growth.

The comparison of nonlocal curvatures shown in Figure 7.5 suggest that the T+FF test is suitable for fuselage design development since it can more than match the curvature realized within the panel's damage zone. The large nonlocal mid-plane strains, shown in Figure 7.5 for the Crown-3 panel, are associated with behavior of the fracture process zone for large notch sizes. Therefor, the large mid-plane strains of the 22 inch fuselage panel test can not be compared to the results of the 0.875 inch notched coupon test.

It should be noted that the proposed theory predicted that the panel would have failed prior to attainment of the 8.85 psi damage tolerance requirement. Had curvature effects upon mid-plane damage been modelled, even less pressure load capability would likely have been predicted. In reality, however, the panel was successful in supporting this requirement and more. Application of this theory would therefore have imposed a

conservative weight penalty upon the fuselage. Finally, the inability of the frame to arrest crack growth raises questions regarding the fail-safe capability of such a design.

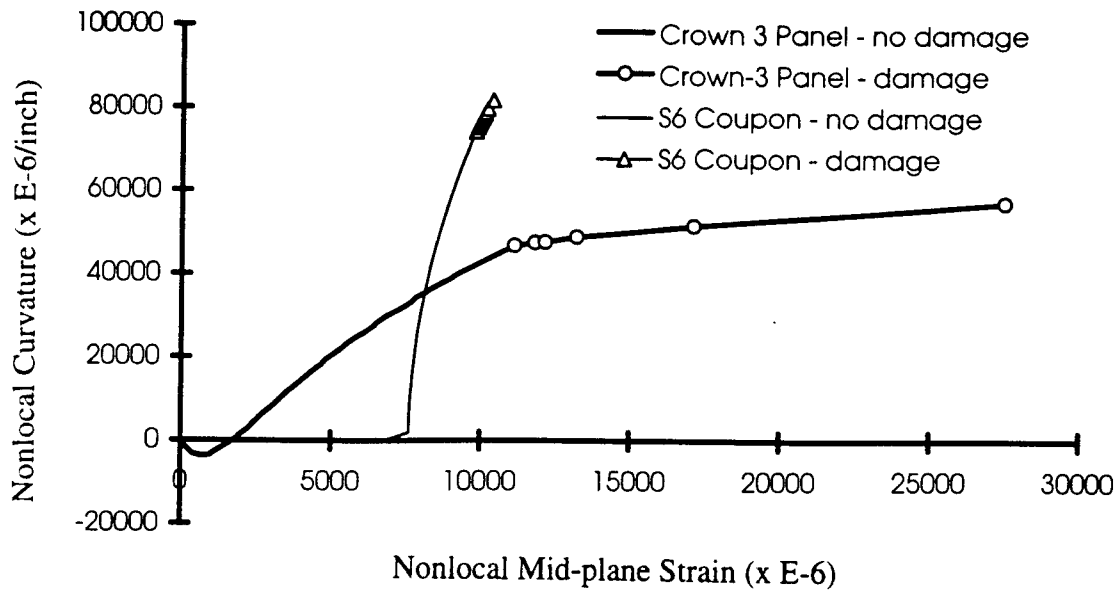


Figure 7.5 Damage Zone Nonlocal Strain Histories from Simulation of Crown Panel Failure and the S6 Laminate T+FF Test Failure

# 8. Discussion

The developed nonlocal damage theory sought to model the macroscopic stiffness degradation caused by an assortment of matrix cracking, fiber breakage, fiber pull-out, matrix-fiber splitting, small-scale delamination, etc.. In doing so it was expected that failure could be predicted for large complex structure made of laminated plate composites in which damage manifests itself as strain softening behavior. It has been demonstrated that such structure can indeed be successfully analyzed using moderate computational resources. Its inaccuracy in predicting large notch fracture was demonstrated to be as much as 11.1 percent conservative. Such inaccuracy could be considered acceptable; and steps can be suggested to improve upon this performance. However, other fracture theories are available which should be considered relative to the performance and computational expense of the proposed damage theory.

Several closed-form analytical fracture criteria were introduced in the literature review of Section 2. Being closed-form, they are computationally free for simple geometries. Three of these methods have been applied to the prediction of the Crown-3 laminate fracture strength as shown in Figure 8.1. All three methods were parametrically fitted to the results of the 0.875 inch notch fracture test. Results of the damage theory and experimental tests are also included. The damage theory performed consistently well in predicting failure with a maximum error of 11.1 percent conservative for the 12 inch notch test result. The Mar-Lin criterion also performed well except it predicts an infinite no-notch strength. Its prediction was 6.1 percent non-conservative for the 12 inch notch. The Linear Elastic Fracture Mechanics (LEFM) model performed poorly. The Point Stress criterion prediction was 25 percent conservative for the 12 inch notch fracture condition. Of these four predictive methods, the damage theory result is the most desirable in that is was the most accurate of the conservative predictions.

An economic study was not performed to ascertain the worth of the damage theory. If concern was limited to fracture of simple, flat, tension-loaded structure, the

Mar-Lin theory seems accurate and very affordable. For application to large complex structure, however, a finite element model is likely required irregardless of which fracture theory is employed. Furthermore, due to the common significance of geometrical nonlinear larger deformation behavior, incremental FEA is often required irregardless of the fracture theory. Therefore, closed-form solution methods loose much of their economy in application to analysis of complex structure. Also, flexure is common at the notch-tip which is not addressed by the closed-form methods. A method for extending the Mar-Lin criterion to general conditions of complex structural failure, such as that of the Crown panel test, has not been identified although Ranniger, et. al., (1995) presented a closed-form analytical method for standard shell geometries based upon the work of Folias (1965a & b). The Point Stress criterion could be applied to such structure; however, review of the stresses generated ahead of the fuselage panel notch indicate that the Point Stress criterion would predict failure at about half that actually attained in test. Therefore, for general complex structural failure, the closed-form criteria are not very attractive and can impose significant weight and material cost penalties upon a design.

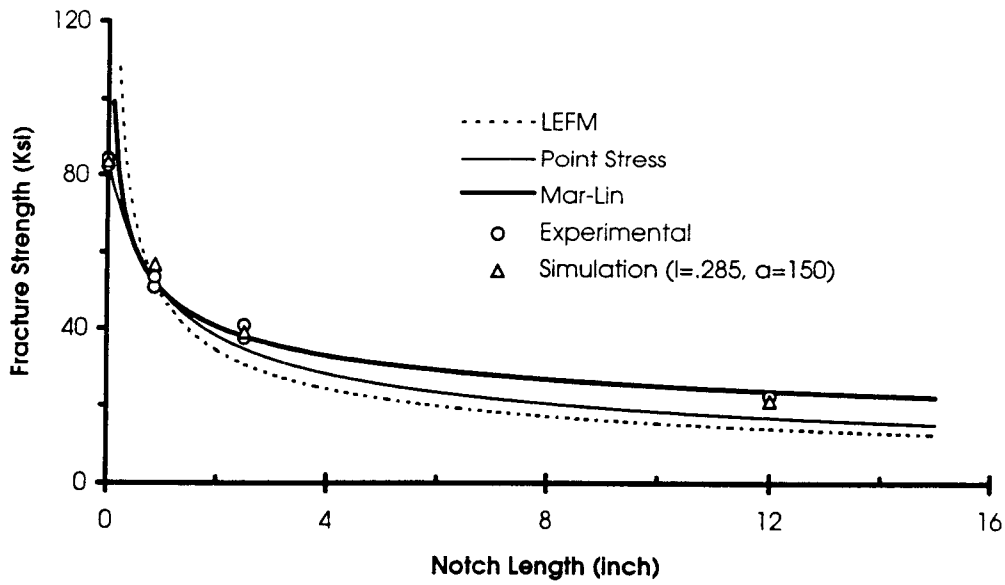


Figure 8.1 Fracture Strength Predictions of Closed-form Criteria versus Damage Theory.

Another analysis alternative would be to apply anisotropic plasticity theory to model the strain softening. This method has already been demonstrated (Dopker et al., 1994) with considerable success. From a computational perspective, the plasticity and damage theory methods are similar. Both require nonlocal treatment (or accept a fixed damage zone element size), incremental solution for treatment of both geometric and material nonlinearity, and an advanced solution path finding method such as the viscous relaxation technique employed herein. However, curvature induced effects would require a layered analysis for the plasticity solution method and the assumption of material homogeneity through the plate thickness. Layered analysis would impose additional computational costs over that of the damage theory analysis. Finally, plastic strain softening does not allow for reduction in stiffness. If the material actually exhibits reduced stiffness rather than permanent strain, then strictly speaking, the plastic solution method would be limited to conditions of monotonic loading.

The developed nonlocal damage theory represents an advancement in the modelling of curvature induced progressive damage effects. The theory is comprised of several parts, each of which can effect the accuracy, generality and efficiency of application. Section 3 detailed the development of the damage effective laminated plate stiffness matrix. In application of the resultant stiffness relation, no problems have been identified and it is offered with confidence as a valuable tool.

Section 4 detailed the kinetics of damage evolution due to growth in nonlocal strain. This area of damage theory has been recognized as being highly discretionary and open to creativity. The proposed damage kinetics was created in the image of the simple maximum strain strength criteria for composites and was thus presumed to represent a simple and physically intuitive basis for damage growth. Like the maximum strain strength criterion, however, the proposed damage kinetics is expected to show some inaccuracy in cases with biaxial load conditions. Additionally, damage growth was assumed to vary in an exponential manner with respect to nonlocal strain. Other researchers have used piece-wise linear functions with good success. Choice of a

functional family is very important for accurate characterization of a laminate, but such a choice is up to the discretion of the user and not an intrinsic element of the proposed damage theory.

Section 6 detailed the experimental method of characterizing a particular laminate according to the proposed damage theory. It was demonstrated that a desirable direct measurement of strain softening is difficult for in-plane load conditions and totally undeveloped for flexural conditions. Thus an indirect method using fracture tests was developed. For in-plane load conditions, no single set of strain softening parameters could be identified to match results of all test conditions. The resultant uncertainty and computational costs of the inverse method should be a strong motivation toward successful development of a direct method of measuring strain softening in laminated composite plate structure.

A possible limitation, in the demonstrated damage characterization, relates to the isotropic definition of the nonlocal treatment. The damage parameter solution curves of Figure 6.8 suggest that different characteristic lengths would apply to the hoop and axial directions of the fuselage laminate. The physical justification for a long-range nonlocal treatment has not been established, rather it is justified in that it rectifies what would be physically unreasonable analysis results otherwise. Therefor it could be proposed that an orthotropic nonlocal treatment be established without violating the basis of the nonlocal treatment. Such a treatment would be consistent with the stiffness and assumed damage behavior of a laminated plate and would not entail any further testing for complete characterization.

Section 6 also detailed the experimental characterization of damage growth due to a combination of tension and flexure. Curvature was theoretically identified to affect both the average level of damage (i.e., mid-plane damage) and its gradient through the laminate thickness. Separate functional relations and characteristic parameters were proposed for modelling the dependence of these two aspect of damage upon curvature. This assumed separation presents problems in experimental determination of their influence upon fracture strength since their influences are physically indistinguishable

from each other. However, both are related to the damage resistance of the outer layers of a laminated plate. Therefor it should be possible for their dependence upon curvature to be related by a single parametric characterization. Such a relationship has yet to be investigated. Instead, these two aspects of curvature induced damage were simulated independently of each other and compared to test results. Results indicate that the damage gradient is ineffectual and that the average mid-plane damage effect could potentially represent the total curvature induced reduction in fracture strength. Such testing required the development of a novel combined tension plus flexure fracture test.

Further application of the proposed theory is at a juncture in its treatment of flexural effects. One approach would assume that the damage gradient is ineffectual in general and to drop it from the proposed damage theory. The other approach would seek to identify a common parametric relation between the two aspects of curvature induced damage.

# 9. Conclusions

The proposed nonlocal damage theory is conceptually simple. This is partly a result of assuming that strain is the force behind damage growth rather than some thermodynamically derived entity. It is also a result of proposing damage growth kinetics modelled after the simple maximum strain strength criterion. Conceptual clarity was also advanced by the assumption that the principal direction of damage is at least approximately coincident with that of nonlocal strain. An isotropic definition of damage could have been developed and would have further simplified the theory. However, damage isotropy was considered too simplistic for characterization of highly directed composites. Instead, a second-order orthotropic definition of damage was put forward in lieu of the more complex fourth-order definition. Finally, the assumption that damage varies linearly through the thickness of a laminated plate enabled the concise definition of damage effective laminated plate stiffness per equation (3-17). Engineers experienced with composites are very familiar with this form of laminated plate stiffness. Such an approach avoids the layered finite element analysis approach which is computationally more expensive, complex and arguably over-simplified .

Incorporation of the proposed damage theory into finite element analysis enabled damage tolerance analysis of large complex structure. This conclusion is based upon the demonstrated analysis of a damaged fuselage panel as reported upon in Section 7. The computer resources necessary for such an analysis were moderate.

The proposed theory performed well in predicting damage tolerance for a large range of damage sizes. Fracture strength was predicted and compared to test results for notches ranging from 0 to 22 inches. The maximum error was 11.1 percent conservative. As discussed in Section 8 and demonstrated in Figure 8.1, damage theory prediction compared favorably with closed-form solutions. These closed-form solution techniques are much less suitable for large complex structural analysis. Plasticity analysis of such strain softening behavior has been demonstrated to also predict damage tolerance well.

However, for materials that actually exhibit stiffness degradation, such an approach can be argued to have limited potential.

It can be concluded that the simulated growth of thru-thickness damage gradient, $\alpha$, has little effect upon fracture strength for the conditions analyzed. It is not clear that such a result can be expected in general. It is speculated, for example, that the extension-bending coupling influence of the damage gradient would have a greater opportunity to influence the outcome strength if a larger active damage zone developed prior to failure. The active damage zone of the analyzed S6 laminate was small due to its acute strain softening. Less acute strain softening may realize a significant damage gradient effect.

The simulated growth of mid-plane damage, $D^0$, due to the combination of extension plus curvature, was not given adequate test support. Nevertheless, it can be concluded that this influence of curvature has the potential to fully account for the reduction in fracture strength realized under such conditions. Furthermore, the developed theory is able to reflect differences in curvature induced damage resistance expected from variation of a laminate ply stack sequence.

The developed tension plus flexure fracture (T+FF) test was affordable, performed well and revealed a fracture strength sensitivity to flexure. This test, represented in Figure 6.11 and shown photographed in Figure 6.12, is adaptable to a wide variety of commercially available test machines. Test induced extension and curvature can be varied to represent a wide range of plate load conditions. Simulation of the geometric nonlinearity that is inherent in this test was not difficult but did require some trial and error to adequately model extensional compliance of the test fixture.

Geometric nonlinearity, associated with large deflections, had a significant effect upon test results and was accurately simulated. Such modelling was successful in simulation of this nonlinear behavior for both the T+FF test and the fuselage crown panel pressure test. Initial concern with artificial stiffening associated with higher-ordered Gaussian integration under flexural condition was found to be unwarranted.

# 10. Recommendations

The proposed theory, or some derivative, should be incorporated into a non-layered finite element analysis program to realize its true efficiency. The theory application that has been reported upon herein was implemented by modifying a layered finite element analysis program. Labor conservation had dictated that this feature be maintained without compromising results. Thirteen layers were employed in the model, one for each ply. A measure of the relative computational efficiency would be interesting.

The curvature induced growth of mid-plane damage, $D^0$, and damage gradient, $\alpha$, are both related to damage resistance of the outer laminate plies. This commonality should enable their growth to be represented by a common material parameter incorporated into separate growth functions. Although the damage gradient has been shown to exhibit negligible influence upon fracture strength, it is not clear that this is generally true. The alternative is to drop the damage gradient form the damage model. However, by identifying the common parameter and associated damage growth functions, both aspects of curvature induced damage, $D^0$ and $\alpha$, may be modelled without ambiguity and without requiring any more testing and simulation than would be required if the damage gradient was dropped.

Testing is needed to determine the shape of the mid-plane damage, $D^0$, threshold curve for combined tension plus flexure conditions. Like the elliptical shape assumed in the analysis (defined in Section 4.3 and characterized in Section 6.3.3), it is hoped that few tests would be required to characterize any laminate according to the identified threshold curve. To identify the best curve shape, multiple test trajectories of combined tension plus flexure should be performed. Careful consideration should be given the interpretation of damage initiation under flexure dominant conditions where failure may be gradual. These no-notch tests could be performed using the developed tension plus flexure test hardware.

Only one trajectory of tension plus flexure was tested for fracture strength. Additional testing is recommended to better understand the influence of curvature upon fracture strength. Such testing, would use the same hardware and method described in Section 6.3.1 but the transverse load actuator should be replaced with one of greater stroke length. Such testing would better serve the characterization of a laminate's rate of damage growth due to curvature than did the test trajectory shown in Figure 6.13 and shown simulated relative to the assumed damage surface in Figure 6.17. Crack face closure and its influence upon fracture strength would eventually have to be considered for test trajectories of greater curvature component.

The proposed damage theory incorporated an isotropic definition for the nonlocal treatment of strain. That is, the spacial averaging of local strain to obtain the nonlocal strain was equal in all directions. The degree of nonlocal behavior was represented by a single material parameter, the characteristic length $l_{ch}$, which characterized the size of the circular nonlocal range. Correlation of simulation results to fuselage skin fracture tests, in both its hoop and axial directions, indicated that different values of characteristic length would control fracture in these directions. This indication is evident in Figure 6.8. Therefore it is recommended that an elliptical nonlocal range be employed which is defined using two characteristic lengths associated with the two principal laminate directions. This definition would be consistent with the orthotropic definition of damage and would improve simulation accuracy for general fracture conditions. And besides, it would not necessitate any further testing or simulation for characterization of a laminate's damage growth. Rather, it would be a simple way to obtain the flexibility needed to characterize damage tolerance for directional composites.

# Bibliography

Backlund, J. & Aronsson, C. 1986. Tensile Fracture of Laminates with Holes. *J. Composite Materials 20:259-307.*

*Barenblatt, G.I. 1962.* The Mathematical Theory of Equilibrium Cracks in Brittle Fracture. *Advances in Applied Mechanics,* Academic Press, 7:55-129.

Bathe, K.J. 1982. *Finite Element Procedures in Engineering Analysis*, Prentice-Hall.

Bazant, Z.P. & Kim, S.S. 1979. Plastic-Fracturing Theory for Concrete. *J. Eng. Mech.*, 105:407-428.

Bazant, Z.P. 1984a. Size Effect in Blunt Fracture: Concrete, Rock, Metal. *J. Eng. Mech.*, 110:4:518-35.

Bazant, Z.P., Belytshko, T.B. & Chang, T.-P. 1984b. Continuum Theory for Strain-Softening. *J. Eng. Mech*, 110:12:1666-92.

Bazant, Z.P. 1984c. Imbricate Continuum and its Variational Derivation. *J. Eng. Mech.*, 110:12:1693-1712.

Bazant, Z.P. & Chang T.-P. 1984d. Nonlocal Finite Element Analysis of Strain-Softening Solids. *J. Eng. Mech.*, 113:1:89-105.

Bazant, Z.P. & Lin, F-B. 1988a. Non-Local Yield Limit Degradation. *Int. J. for Numerical Methods in Engineering*, 26:1805-23.

Bazant, Z.P. & Lin, F.-B. 1988b. Nonlocal Smeared Cracking Model for Concrete Fracture. *J. of Structural Engineering*, 114:11:2493-2510.

Bazant, Z.P. & Pijaudier-Cabot, G. 1989. Measurement of characteristic length of nonlocal continuum. *J. Eng. Mech.*, 115:755-67.

Bazant, Z.P. & Cedolin, L. 1991. *Stability of Structures: Elastic, Inelastic, Fracture, and Damage Theories*, Oxford University Press, New York.

Bazant, Z.P. 1994. Nonlocal Damage Theory Based on Micromechanics of Crack Interactions. *J. Eng. Mech.*, 120:3:593-617.

Bazant, Z.P., Daniel, I.M. & Li, Z. 1995. *Size Effect and Fracture Characteristics of Composite Laminates*. Report 94-4/475s, Dept. of Civil Eng., Northwestern Univ..

Belytchko, T & Lasry, D. 1989. A Study of Localization Limiters for Strain-Softening in Statics and Dynamics. *Computers & Structures*, 33:3:707-15.

Brekelmans, W.A.M. 1993. Nonlocal Formulation of the Evolution of Damage in a One-Dimensional Configuration. *Int. J. Solids Structures,* 30:11:1503-12.

Carpinteri, A., Colombo, G., Ferrara, G. & Giuseppetti, G. 1987. Numerical Simulation of Concrete Fracture through a Bilinear Softening Stress-Crack Opening Displacement Law. *SEM/RILEM International Conf. on Fracture of Concrete and Rock*, Houston, 178-191.

Chaboche, J.L. 1990. On the Description of Damage Induced Anisotropy and Active/ Passive Damage Effect. *Damage Mechanics in Engineering Materials*, ASME, AMD-109/MD- 24:153-66.

Chen, Z. & Schreyer, H.L. 1994. On Nonlocal Damage Models for Interface Problems. *Int. J. Solids Structures*, 31:9:1241-61.

Chow, C.L. & Wang, J. 1987. An Anisotropic Theory of Elasticity for Continuum Damage Mechanics. *Int. J. Fracture,* 33, 3-16.

Chuang, T.-J. & Mai, Y.-W. 1989. Flexural Behavior of Strain-Softening Solids. *Int. J. Solids Structures,* 25:12:1427-43.

Copley, L. G. & Sanders. 1969. A Longitudinal Crack in a Cylindrical Shell under Internal Pressure. *J. L., Int. J. Fract. Mech.*, 5:2:117-31.

Cordebois, J.L. & Sidoroff, F. 1979. Damage Induced Elastic Anisotropy. Mechanical *Behavior of Anisotropic Solids*, Colloque Euromech 115, ed. Boehler, J.-P., Martinus Nijhoff Publishers, 761-74.

de Borst, R. & Muhlhaus, H.B. 1991. Continuum Models for Discontinuous Media. *RILEM Symposium on Fracture Mechanics of Brittle Disordered Materials*, Hoordwijk, June.

de Borst, R. & Muhlhaus, H.-B. 1992. Gradient-Dependent Plasticity: Formulation and Algorithmic Aspects. *Int. J. for Numerical Methods in Engineering*, 35:521-539.

de Vree, J.H.P., Brekelmans, W.A.M., & van Gils, M. 1995. Comparison of Nonlocal Approaches in Continuum Damage Mechanics. *Computers & Structures*, 55:4:581-88.

Dopker, B., Murphy, D.P., Ilcewicz, L. & Walker, T. 1994. Damage Tolerance Analysis of Composite Transport Fuselage Structure. *35TH AIAA/ASME/ASCE/AMS/ASC Structures, structural Dynamics and Materials Conf.*.

Dopker, B., Ilcewicz, L.B., Murphy, D.P., Biornstad, R. & McGowan, D. 1996. Composite Structural Analysis Supporting Affordable Manufacturing and Maintenance. *Sixth NASA/DOD/ARPA Advanced Composite Technology Conference*, NASA CP-3326.

DuBois, B. 1996. A Strain-Softening Discrete Crack Model for Predicting Failure of Notched Laminates. *MS Project Report*, Dept. of M.E., Ore. State Univ..

Dugdale, D.S. 1960. Yielding of Steel Sheets Containing Slits. *J. Mech. Phys. Solids*, 8:100-8.

Ehlers, R. 1986. Stress Intensity Factors and Crack Opening Areas for Axial Through Cracks in Hollow Cylinders under Internal Pressure Loading. *Eng. Fract. Mech.*, 25:1:63-77.

Erdogan, F. & Kibler, J.J. 1969. Cylindrical and Spherical Shells with Cracks. *Int. J. Fract. Mech.*, 5:3:229-36.

Erdogan, F. & Ratwani, M. 1972. Plasticity and the Crack Opening Displacement in Shells. *Int. J. Fract. Mech.*, 8:4:413-26.

Eringen, A.C. 1968. Theory of Micropolar Elasticity. *Fracture*, Vol. 2, Ed. by H. Lievowitz, Academic Press, 662-729.

Eringen, A.C. & Edelen, D.G. 1972. On Nonlocal Elasticity. *Int. J. Eng. Sci.*, 10:233-48.

Figueiras, J.A. & Owen, D.R.J. 1984. Analysis of elasto-plastic and geometrically nonlinear anisotropic plates and shells. *Finite Element Software for Plates and Shells*, Pineridge Press, Swansea, 235-396.

Folias, E. S. 1965a. A Finite Line Crack in a Pressurized Spherical Shell. *Int. J. Fract. Mech.*, 1:1:20-46.

Folias, E. S. 1965b. A Axial Crack in a Pressurized Cylindrical Shell. *Int. J. Fract. Mech.*, 1:2:104-13.

Folias, E. S. 1974. Fracture in Pressure Vessels. *Thin Sell Structures*, ed. Y.C. Fung and E.E. Sechler, Prentince Hall, Englewood Cliffs, 483-518.

Han, D.J. & Chen, W.F. 1986. On Strain-Space Plasticity Formulation for Hardening-Softening Materials with Elasto-Plastic Coupling. *Int. J. Solids Structures*, 22:8: 935-50.

Hansen, N.R. & Schreyer, H.L. 1994. A Thermodynamically Consistent Framework for Theories of Elastoplasticity Coupled with Damage. *Int. J. Solids Structures*, 31:3: 359-89.

Hillerborg, A., Modeer, M. & Peterson, P.E. 1976. Analysis of Crack Formation and Crack Growth in Concrete by Means of Fracture Mechanics and Finite Elements. *Cement and Concrete Research*, 6:773-82.

Hillerborg, A. 1983. Analysis of one Single Crack. *Fracture Mechanics of Concrete*, Ed. Wittmann, F.H., Publ. Elsevier Science, 223-49.

Hinton, E. & Owen, D.R.J. 1977. *Finite Element Programming*. Academic Press, New York.

Hollmann, K. & Backlund, J. 1988. Notch Sensitivity of Linearly Softening Materials Exhibiting Tensile Fracture. *Eng. Fract. Mech.*, 31:4:577-90.

Ilcewicz, L.B., Walker, T.H., Murphy, D.P., Dopker, B. & Scholz, D.B. 1993. Tension fracture of laminates for transport fuselage – part 4: damage tolerance analysis. *Fourth NASA Advanced Technology Conference*, NASA CP 3229, 264-98.

Irwin, G.R. 1958. Fracture, *Hadbuch der Physik, VI*, Springer-Verlag, Heidelberg, 551-90.

Jones, R.M. 1975. *Mechanics of Composite Materials*, Hemisphere Publishing Corp., New York, 147-56.

Ju, J.W. 1989. On Energy-based Coupled Elastoplastic Damage Theories: Constitutive Modeling and Computational Aspects. *Int. J. Solids Structures*, 25:7:803-33.

Kachonov, M. 1958. Time of the Rupture Process Under Creep Conditions. *Isv. Akad. Nauk. SSR*, Otd Tekh. Nauk. 8:26-31. (in Russian)

Kennedy, T.C. & Kim, J.B. 1987. Finite Element Analysis of a Crack in a Micropolar Elastic Material. *Computers in Engineering*, ed. Raghaven R. and Cokonis T.J., ASME, 439-44.

Kennedy, T. & Nahan, M. 1996. A Simple Nonlocal Damage Model for Predicting Failure of Notched Laminates. *Composite Structures*, 35:229-36.

Krajcinovic, D. 1984. Continuum Damage Mechanics. *Applied Mechanics Review*, 37:1:1-6.

Krajcinovic, D. 1985. Constitutive Theories for Solids with Defective Microstructure. *Damage Mechanics and Continuum Modeling*, ed. Stubbs, N. & Krajcinovic, D., ASCE, 39-57.

Kroner, E. 1967. Elasticity Theory of Materials with Long Range Cohesive Forces. *Int. J. Solids Structures*, 3:731-42.

Kwon, Y.W. 1993. Study of Crack Closure in Laminated Composite Shells. *Eng. Fract. Mech.*, 45:5:663-69.

Lai, M.W., Rubin, D. & Krempl, E. 1978. *Intro. to Continuum Mechanics*. Pergamon Press.

Lemaitre, J. 1971. Evaluation of Dissipation and Damage in Metals. *Proc. I.C.M.*, Vol. 1, Kyoto, Japan.

Lemaitre, J. 1984. How to Use Damage Mechanics. *Nuclear Eng. and Design*, 80:233-45.

Lemaitre, J & Dufailly, J. 1987. Damage Measurements. *Eng. Fract. Mech.*, 28:5/6:643-61.

Lemaitre, J. 1992. *A Course on Damage Mechanics*. Springer-Verlag.

Lee, H., Peng, K. & Wang, J. 1985. An Anisotropic Damage Criterion for Deformation Instability and its Application to Forming Limit Analysis of Metal Plates. *Eng. Fract. Mech.*, 21:5:1031-54.

Lesne, P.-M. & Saanouni, K. 1992. A New Formalism to Describe Irreversible Strains Due to Damage in Ceramic Matrix Composites. *Recent Advances in Damage Mechanics and Plasticity*. ASME, AMD-132/MD-30.

Li, V.C. 1990. Non-Linear Fracture Mechanics of Inhomogeneous Quasi-Brittle Materials. Nonlinear Fracture Mechanics, Wnuk, M.P. ed., Wpringer-Verlag, 143-91.

Llorca, J. & Elices, M. 1992. A Cohesive Crack Model to Study the Fracture Behavior of Fiber-reinforced Brittle-Matrix Composites. Int. J. Fracture, 54:251-67.

Lo, D.C., Allen, D.H. & Harris, C.E. 1993. Modeling the Progressive Failure of Laminated Composites with Continuum Damage Mechanics. Fracture Mechanics: Twenty-third Symposium, ASTM 1189, 680-95.

Mar, J.W. & Lin, K.Y. 1976. Finite Element Analysis of Stress Intensity Factors for Cracks at a Bi-material Interface. Int. J. Fracture, 12:521-31.

Mar, J.W. & Lin, K.Y. 1977. Fracture Mechanics Correlation for Tensile Failure of Filamentary Composites with Holes. Journal of Aircraft, 14:7:703-5.

Mazars, J. & Pijaudier-Cabot, G. 1989a. Continuum Damage Theory - Application to Concrete. J. Eng. Mech.,ASCE, 115:3.

Mazars, J., Ramtani, S. & Berthaud, Y. 1989b. An Experimental Procedure to Delocalize Tensile Failure and to Identify the Unilateral Effect of Distributed Damage. Cracking and Damage Strain Localization and Size Effect, eds. Mazars, J. & Bazant, Z.P., Elsevier, Amsterdam, 55-64.

Nuismer, R.J. & Whitney, J.M. 1975. Uniaxial Failure of Composite Laminates Containing Stress Concentration. Fracture Mechanics of Composites, ASTM STP 593, 117-42.

Pijaudier-Cabot, G. & Bazant, Z.P. 1987. Nonlocal Damage Theory. J. Eng. Mech., 113:2:1512-33.

Pipes, R.B., Wetherhold, R.C. & Gillespie, J.W. Jr. 1979. Notched Strength of Composite Materials. J. Composite Materials, 13:148-60.

Poe, C.C. 1983. A Unifying Strain Criterion for Fracture of Fibrous Composite Laminates. Eng. Fract. Mech., 17:2:153-71.

Ramtani, S., Berthaud, Y. & Mazars J. 1992. Orthotropic Behavior of Concrete with Directional Aspects: Modelling and Experiments. Nuclear Eng. Design., 113:997-111.

Ranniger, D.U., Lagace, P.A. & Graves, M.F. 1995. Damage Tolerance and Arrest Characteristics of Pressurized Graphite/Epoxy Tape Cylinders. Composite Materials: Fatigue and Fracture - Fifth Vol., ed. R.H. Martin, ASTM STP 1230, 407-26.

Reddy, Y.S.N., Moorthy, C.M.D. & Reddy, J.N. 1995. Non-Linear Progressive Failure Analysis of Laminated Composite Plates. Int. J. Non-Linear Mechanics, 30:5:629-49.

Rice, J.R. 1968. A Path Independent Integral and the Approximate Analysis of Strain Concentration by Notches and Cracks. J. Appl. Mech. 379-86.

Rice, J.R. 1977. The localization of Plastic Deformation. Theoretical and Applied Mechanics, Proc. 14th Int. Congr. Theoret. Appl. Mech. ed. Koiter, W.T., Amsterdam, 207-20.

Riks, E., Brogan, F.A. & Rankin, C.C. 1989. Bulging Cracks in Pressurized Fuselages: A Procedure for Computation. Analytical and Computational Models of Shells, ASME/CED-Vol. 3.

Schreyer, H.L. & Chen, Z. 1986. One-Dimensional Softening with Localization. J. of Applied Mechanics, ASME, 53:791-96.

Shahid, I., Sun, H.-T. & Chang, F.-K. 1995a. An Accumulative Damage Model for Tensile and Shear Failures of Laminated Composite Plates. J. Composite Materials, 29:7:926-71.

Shahid, I., Sun, H.-T. & Chang, F.-K. 1995b. Predicting Scaling Effect on the Notched Strength of Prepreg and Fiber Tow-Placed Laminated Composites. J. Composite Materials, 29:8:1063-95.

Sluys, L.J., de Borst & R., Muhlhaus, H.-B. 1993. Wave Propagation, Localization and Dispersion in a Gradient-Dependent Medium. Int. J. Solids Structures, 30:9:1153-71.

Stevens, D.J. & Krauthemmer, T. 1989. Nonlocal Continuum Damage/Plasticity Model for Impulse-Loaded RC Beams. J. of Structural Engineering, 115:9:2329-47.

Stromberg, L. & Ristinmaa, M. 1996. FE-formulation of a Nonlocal Plasticity Theory. Comput. Methods Appl. Mech. Engrg., 136:127-44.

Swift, T. June, 1987. Damage Tolerance in Pressurized Fuselages. 14$^{th}$ Symposium of the Int. Comm. on Aeronautical Fatigue (ICAF) New Materials and Fatigue Resistant Aircraft Design, Canada.

Valanis, K.C. 1991. A Global Damage Theory and the Hyperbolicity of the Wave Problem. J. A. Mech.,58:311-18.

Voyiadjis, G.Z., & Kattan, P.I. 1993. Damage of Fiber-Reinforced Composite Materials with Micromechanical Characterization. Int. J. Solids Structures, 30:20:2757-78.

Waddoups, M.E., Eisenmann, J.R. & Kaminski, B.E. 1971. Macroscopic Fracture Mechanics of Advanced Composite Materials. J. Composite Materials, 5:446-54.

Walker, T.H., Avery, W.B., Ilcewicz, L.B., Poe, C.C.& Harris, C.E. 1991. Tension fracture of laminates for transport fuselage – part 1: Material Screening. *Second NASA Advanced Technology Conference*, NASA CP 3154, 197-238.

Walker, T.H., Ilcewicz, L.B., Polland, D.R. & Poe, C.C. 1992. Tension fracture of laminates for transport fuselage – part 2: large notches. *Third NASA Advanced Technology Conference*, NASA CP 3178, 727-58.

Walker, T.H., Ilcewicz, L.B., Polland, D.R., Bodine, J.V. & Poe, C.C. 1993. Tension fracture of laminates for transport fuselage – part 3: structural configurations. *Fourth NASA Advanced Technology Conference*, NASA CP 3229, 243-64.

Walker, T.H., Flynn, B.W., Hanson, C.T., & Ilcewicz, L.B. 1995. *Monthly Technical Progress Report, Advanced Technology Composite Aircraft Structures, Boeing Commercial Airplane Group*, NAS1-18889 Report No. 77.

Walker, T., Scholz, Flynn, B., Dopker, B. D.B., Bodine, J., Ilcewicz, L.B., Rouse,M., McGowan, D., & Poe, C.Jr. 1996. Damage Tolerance of Composite Fuselage Structure. *Sixth NASA/DOD/ARPA Advanced Composite Technology Conference*, NASA CP-3326.

Webster, R.L. 1980. On the static analysis of structures with strong geometric nonlinearity. *Computers & Structures*, 11:137-45.

Wells, A.A. 1961. Unstable Crack Propagation in Metals: Cleavage and Fast Fracture. *Proceedings of the Crack Propagation Symposium*, Cranfield, UK., 1:84.

Whitney, J.M. & Nuismer, R.J. 1974. Stress Fracture Criterion for Laminated Composites Containing Stress Concentrations. *J. Composite Materials*, 8:253-65.

Xia, S., Takezono, S. & Tao, K. 1993. Nonlocal Elasticity Damage Near Crack Tip. *Int. Journal of Fracture*, 62:87-95.

Zhao, Y., Tripathy, A.K. & Pang, S.-S. 1995. Bending Strength of Composite Laminates with an Elliptical Hole. *Polymer Composites,* 16:1:60-69.

# APPENDICES

# Appendix A Expanded Matrices of Damage Effective Laminated Plate Stiffness

The stress-strain constitutive relation for progressively damaged laminated plate was developed in Section 3; producing a constitutive relation of a form identical to that developed using Classical Laminated Plate Theory. The new laminated plate stress-strain constitutive relation can be expressed as

$$\begin{Bmatrix} \mathbf{N} \\ \mathbf{M} \end{Bmatrix} = \begin{bmatrix} \tilde{\mathbf{A}} & \tilde{\mathbf{B}} \\ \tilde{\mathbf{B}} & \tilde{\mathbf{C}} \end{bmatrix} \begin{Bmatrix} \boldsymbol{\varepsilon}^0 \\ \mathbf{K} \end{Bmatrix} \tag{A-1}$$

The effective stiffness sub-matrices are fully expanded below. This expansion is limited to the special case of a nominally symmetric laminate for which the nominal interaction stiffnesses, $B_{ij}$ and $E_{ij}$, are null. The expansion is further limited to balanced laminates with respect to the principal laminate coordinate basis. This later condition results in nominal in-plane and bending stiffness components, $A_{13} = A_{23} = C_{13} = C_{23}$, equal to zero. Sub-matrices [A], [C], $[\tilde{A}]$ and $[\tilde{C}]$ are symmetric. Accounting for the special laminate just described, the relations expressing the effective stiffness sub-matrices can be reduced from equation (3-18) to

$$\tilde{\mathbf{A}} = \mathbf{N}_D^T : \mathbf{A} : \mathbf{N}_D + \mathbf{N}_\alpha^T : \mathbf{C} : \mathbf{N}_\alpha \tag{A-2a}$$

$$\tilde{\mathbf{B}} = -2\mathbf{N}_D^T : \mathbf{C} : \mathbf{N}_\alpha \tag{A-2b}$$

$$\tilde{\mathbf{C}} = \mathbf{N}_D^T : \mathbf{C} : \mathbf{N}_D + \mathbf{N}_\alpha^T : \mathbf{F} : \mathbf{N}_\alpha \tag{A-2c}$$

A detailed expansion of these sub-matrices follows.

$$
\left[\tilde{A}\right] = \begin{bmatrix}
A_{11}(1-D_{11}^0)^2 & A_{12}(1-D_{11}^0)(1-D_{22}^0) & -(A_{11}+A_{12})D_{12}^0(1-D_{11}^0)/2 \\
+A_{66}(D_{12}^0)^2 & +A_{66}(D_{12})^2 & -A_{66}(2-D_{11}^0-D_{22}^0)D_{12}^0/2 \\
+C_{11}(\alpha_{11})^2 & +C_{12}\alpha_{11}\alpha_{22} & -(C_{11}+C_{12})\alpha_{11}\alpha_{12}/2 \\
+C_{66}(\alpha_{12})^2 & +C_{66}(\alpha_{12})^2 & -C_{66}(\alpha_{11}+\alpha_{22})\alpha_{12}/2 \\
 & A_{22}(1-D_{22}^0)^2 & -(A_{12}+A_{22})D_{12}^0(1-D_{22}^0)/2 \\
 & +A_{66}(D_{12})^2 & -A_{66}(2-D_{11}^0-D_{22}^0)D_{12}^0/2 \\
 & +C_{22}(\alpha_{22})^2 & -(C_{12}+C_{22})\alpha_{12}\alpha_{22}/2 \\
 & +C_{66}(\alpha_{12})^2 & -C_{66}(\alpha_{11}+\alpha_{22})\alpha_{12}/2 \\
 & & (A_{11}+2A_{12}+A_{22})(D_{12}^0)^2/4 \\
\text{Symmetric} & & +A_{66}(2-D_{11}^0-D_{22}^0)^2/4 \\
 & & +(C_{11}+2C_{12}+C_{22})(\alpha_{12})^2/4 \\
 & & +C_{66}(\alpha_{11}+\alpha_{22})^2/4
\end{bmatrix}
$$

$$
\left[\tilde{B}\right] = 2* \begin{bmatrix}
-C_{11}(1-D_{11}^0)\alpha_{11} & -C_{12}(1-D_{11}^0)\alpha_{22} & -(C_{11}+C_{12})(1-D_{11}^0)\alpha_{12}/2 \\
+C_{66}D_{12}^0\alpha_{12} & +C_{66}D_{12}^0\alpha_{12} & +C_{66}D_{12}^0(\alpha_{11}+\alpha_{22})/2 \\
-C_{12}(1-D_{22}^0)\alpha_{11} & -C_{22}(1-D_{22}^0)\alpha_{22} & -(C_{12}+C_{22})(1-D_{22}^0)\alpha_{12}/2 \\
+C_{66}D_{12}^0\alpha_{12} & +C_{66}D_{12}^0\alpha_{12} & +C_{66}D_{12}^0(\alpha_{11}+\alpha_{22})/2 \\
+(C_{11}+C_{12})D_{12}^0\alpha_{11}/2 & +(C_{12}+C_{22})D_{12}^0\alpha_{22}/2 & (C_{11}+2C_{12}+C_{22})D_{12}^0\alpha_{12}/4 \\
-C_{66}(2-D_{11}^0-D_{22}^0)\alpha_{12}/2 & -C_{66}(2-D_{11}^0-D_{22}^0)\alpha_{12}/2 & -C_{66}(2-D_{11}^0-D_{22}^0)(\alpha_{11}+\alpha_{22})/4
\end{bmatrix}
$$

$$
\left[\tilde{C}\right] = \begin{bmatrix}
C_{11}(1-D_{11}^0)^2 & C_{12}(1-D_{11}^0)(1-D_{22}^0) & -(C_{11}+C_{12})\,D_{12}^0(1-D_{11}^0)/2 \\
+C_{66}(D_{12}^0)^2 & +C_{66}(D_{12})^2 & -C_{66}(2-D_{11}^0-D_{22}^0)\,D_{12}^0/2 \\
+F_{11}(\alpha_{11})^2 & +F_{12}\,\alpha_{11}\,\alpha_{22} & -(F_{11}+F_{12})\,\alpha_{11}\,\alpha_{12}/2 \\
+F_{66}(\alpha_{12})^2 & +F_{66}(\alpha_{12})^2 & -F_{66}(\alpha_{11}+\alpha_{22})\,\alpha_{12}/2 \\
 & C_{22}(1-D_{22}^0)^2 & -(C_{12}+C_{22})\,D_{12}^0(1-D_{22}^0)/2 \\
 & +C_{66}(D_{12})^2 & -C_{66}(2-D_{11}^0-D_{22}^0)\,D_{12}^0/2 \\
 & +F_{22}(\alpha_{22})^2 & -(F_{12}+F_{22})\,\alpha_{12}\,\alpha_{22}/2 \\
 & +F_{66}(\alpha_{12})^2 & -F_{66}(\alpha_{11}+\alpha_{22})\,\alpha_{12}/2 \\
 & & (C_{11}+2C_{12}+C_{22})(D_{12}^0)^2/4 \\
\text{Symmetric} & & +C_{66}(2-D_{11}^0-D_{22}^0)^2/4 \\
 & & +(F_{11}+2F_{12}+F_{22})(\alpha_{12})^2/4 \\
 & & +F_{66}(\alpha_{11}+\alpha_{22})^2/4
\end{bmatrix}
$$

# Appendix B: S6 & S7 Laminate Test Results

(Unnotched Tension, Tension Fracture and T+FF Tests)

## Summary: Panel S6 Laminate Fracture Test (Tension + Flexure)

**Laminate:** AS4/938 graphite/epoxy
Source = failed Boeing fracture panel S6
Stacking Sequence: 45/-45/90/0/60/-60/90/-60/60/0/90/-45/45

## Tests: Load Axial ... Lock Cross-head Position ... Load Transverse

Test Conditions: Uniaxial load direction = laminate 90 degree orientation (hoop)
Cross-head position locked at load of 14 kips followed by transverse loading
Cross-head rate = .03"/min.
Sample rate of 12.5/sec.
Room Temperature

| Coupon | Notch Length (in.) | Width (in.) | Thickness (in.) left/right | First Audible Damage Load (lbs.) | Axial Failure Load (lbs.) | Trans. Failure Load (lbs.) | Far-field Mid-plane Failure Strain (xE-6) | Far-field Failure Curvature (xE-6/in.) | Notes: |
|---|---|---|---|---|---|---|---|---|---|
| AS4-2 | 0.862 | 3.970 | .092/.093 | 11600. | 16210. | -1480. | 5290. | 27050. | 1, |
| AS4-5 | 0.862 | 3.970 | .093/.093 | 10300. | 16920. | -1700. | 5390. | 27960. | 2,3 |
| AS4-6 | 0.863 | 3.960 | .093/.093 | 11300. | 16950. | -1805. | 5620. | 37350. | 2, |

Notes: (1) Coupon cut from half of failed 10"x30" Boeing fracture panel S6-2b
(2) Coupon cut from half of failed 10"x30" Boeing fracture panel S6-1b
(3) Initial test run had cross-head position locked at load of 11.18 kips.
Specimen did not fail before limit of trans. load stroke.
Trans. load was removed and the axial load dropped to approx. 9 kips.
Cross-head lock load was reset at 14 kips.

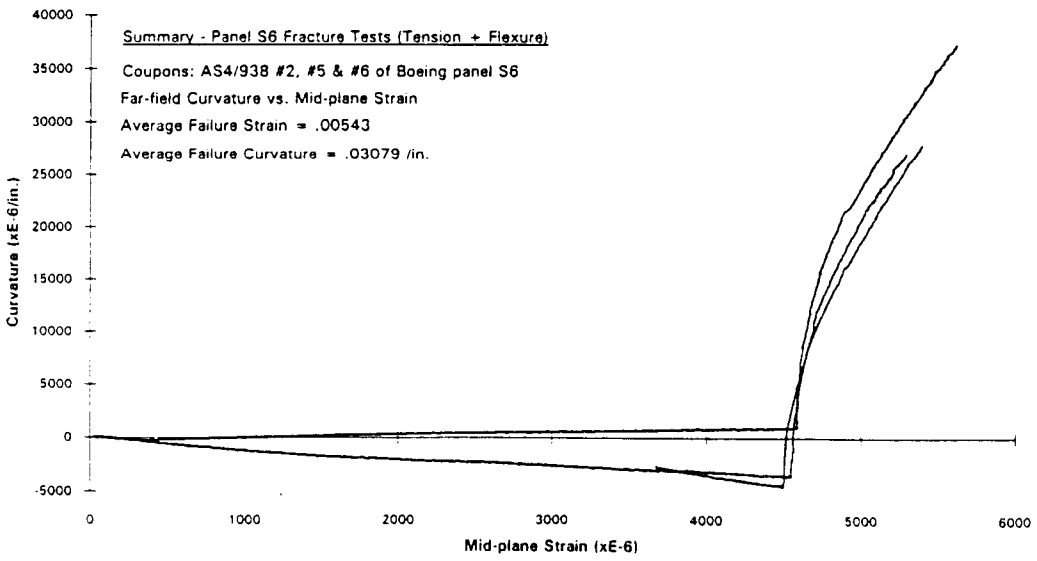

## Summary: Panel S6 Laminate Tension Modulus/ Unnotched Failure Tests

**Laminate:** AS4/938 graphite/epoxy
Source = failed Boeing fracture panel S6
Stacking Sequence: 45/-45/90/0/60/-60/90/-60/60/0/90/-45/45

**Test Conditions:** Load direction = laminate 90 degree orientation (hoop)
Cross-head rate = .03"/min.
Room Temperature
Sample rate of 12.5/sec.

| Coupon | Thick./Width | Mod. (Msi) | Failure Load | Notes: |
|---|---|---|---|---|
| H1 | .093"/.919" | 8.377 | 7886 lbs./in. | 1,2,3,6 |
| H3 | .092"/.861" | 8.762 | 7559 lbs./in. | 1,4,5,6 |
| Average | ------ | 8.570 | 7720 lbs./in. | |

Notes: 1- Test per ASTM D 3039
2- Coupon cut from half of failed 10"x30" Boeing fracture panel S6-2b
3- Maximum recordable strain reached (.0063) prior to failure
4- Coupon cut from half of failed 10"x30" Boeing fracture panel S6-1b
5- Maximum recordable strain reached (.0072) prior to failure
6- Modulus calculated from 1800 and 5600 micro-strain data samples.

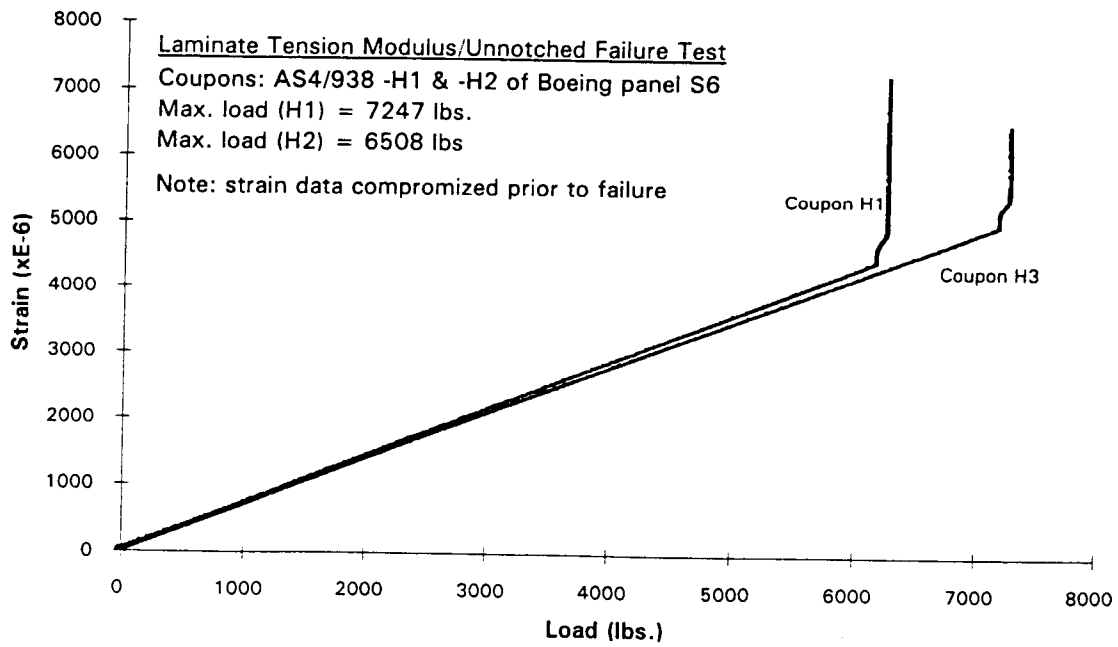

## Summary: Panel S7 Laminate Fracture Test (Tension + Flexure)

**Laminate:** AS4/938 graphite/epoxy
Source = failed Boeing fracture panel S7
Stacking Sequence: 45/-45/90/0/60/-60/90/-60/60/0/90/-45/45

### Test: Load Axial ... Lock Cross-head Position ... Load Transverse

Test Conditions: Uniaxial load direction = laminate 90 degree orientation (hoop)
Cross-head position locked at load of 12.05 kips followed by transverse loading
Cross-head rate = .03"/min.
Sample rate of 12.5/sec.
Room Temperature

| Coupon | Notch Length (in.) | Width (in.) | Thickness (in.) left/right | First Audible Damage Load (lbs.) | Axial Failure Load (lbs.) | Trans. Failure Load (lbs.) | Far-field Mid-plane Failure Strain (xE-6) | Far-field Failure Curvature (xE-6/in.) | Notes: |
|---|---|---|---|---|---|---|---|---|---|
| AS4-1 | 0.864 | 3.987 | .090/.089 | 11400. | 15414. | -1727. | 5030. | 37244. | 1,3 |

Notes: (1) Coupon cut from half of failed 10"x30" Boeing fracture panel S7-1b
(3) Cross-head lock load of 12.05 kips was 75% if measured tension-only fracture strength.

### Test: Axial Load Only (no flexure)

Test Conditions: Uniaxial load direction = laminate 90 degree orientation (hoop)
Cross-head rate = .03"/min.
Room Temperature
Sample rate of 12.5/sec.

| Coupon | Notch Length (in.) | Width (in.) | Thickness (in.) left/right | First Audible Damage Load (lbs.) | Axial Failure Load (lbs.) | Trans. Failure Load (lbs.) | Far-field Mid-plane Failure Strain (xE-6) | Far-field Failure Curvature (xE-6/in.) | Notes: |
|---|---|---|---|---|---|---|---|---|---|
| AS4-4 | 0.862 | 3.956 | .088/.088 | N/A | 16070. | N/A | N/A | N/A | 1, |

Notes: (1) Coupon cut from half of failed 10"x30" Boeing fracture panel S6-2b

## Coupon AS4-1 & Gage Layout

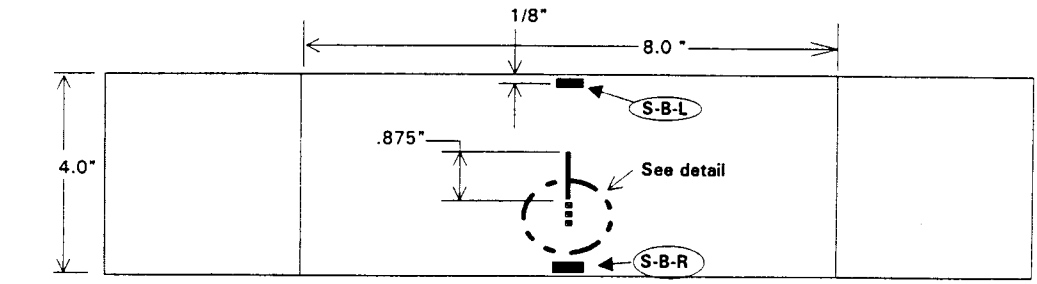


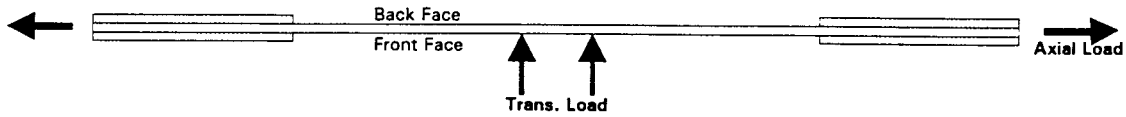


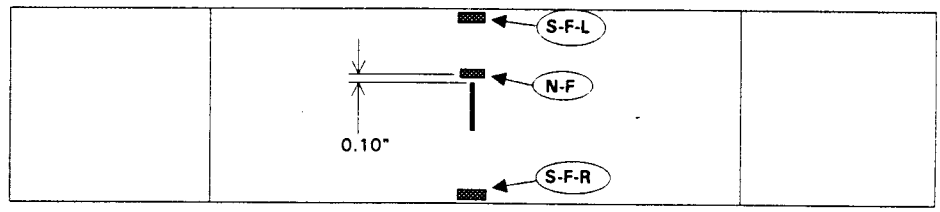


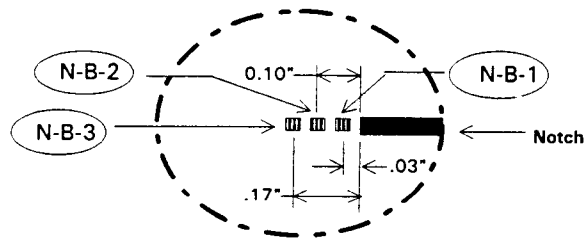


**Notch-tip Gage detail**

### Gage Specifications

| Gage I.D. | Length(in.) | G.F. | Kt | Measure | Bridge Network |
|---|---|---|---|---|---|
| S-B-L | 0.125 | 2.08 | 0.70% | B-face strain | Half bridge, leg #1, with S-B-R |
| S-B-R | " | " | " | " | Half bridge, leg #3, with S-B-L |
| S-F-L | " | " | " | F-face strain | Half bridge, leg #3, with S-F-R |
| S-F-R | " | " | " | " | Half bridge, leg #1, with S-F-L |
| N-B-1 | 0.02 | 1.96 | 2.20% | Surf.-Strain | Qtr. bridge, leg #1 |
| N-B-2 | " | " | " | " | " " |
| N-B-3 | " | " | " | " | " " |
| N-F | 0.125 | 2.115 | 1.00% | " | " " |

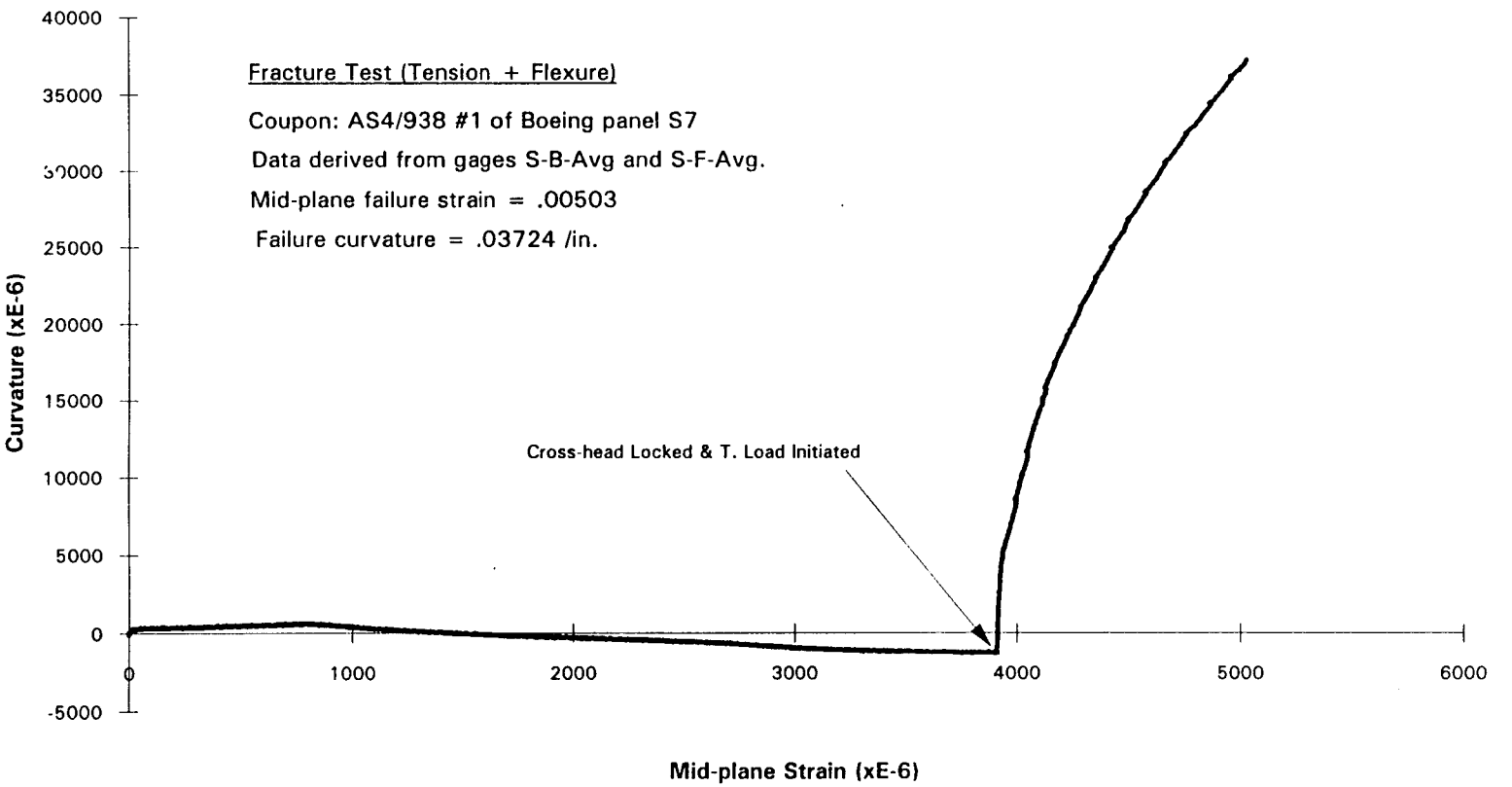
Fracture Test (Tension + Flexure)
Coupon: AS4/938 #1 of Boeing panel S7
Data derived from gages S-B-Avg and S-F-Avg.
Mid-plane failure strain = .00503
Failure curvature = .03724 /in.
Cross-head Locked & T. Load Initiated
Curvature (xE-6)
40000
35000
30000
25000
20000
15000
10000
5000
0
-5000
0
1000
2000
3000
4000
5000
6000
Mid-plane Strain (xE-6)

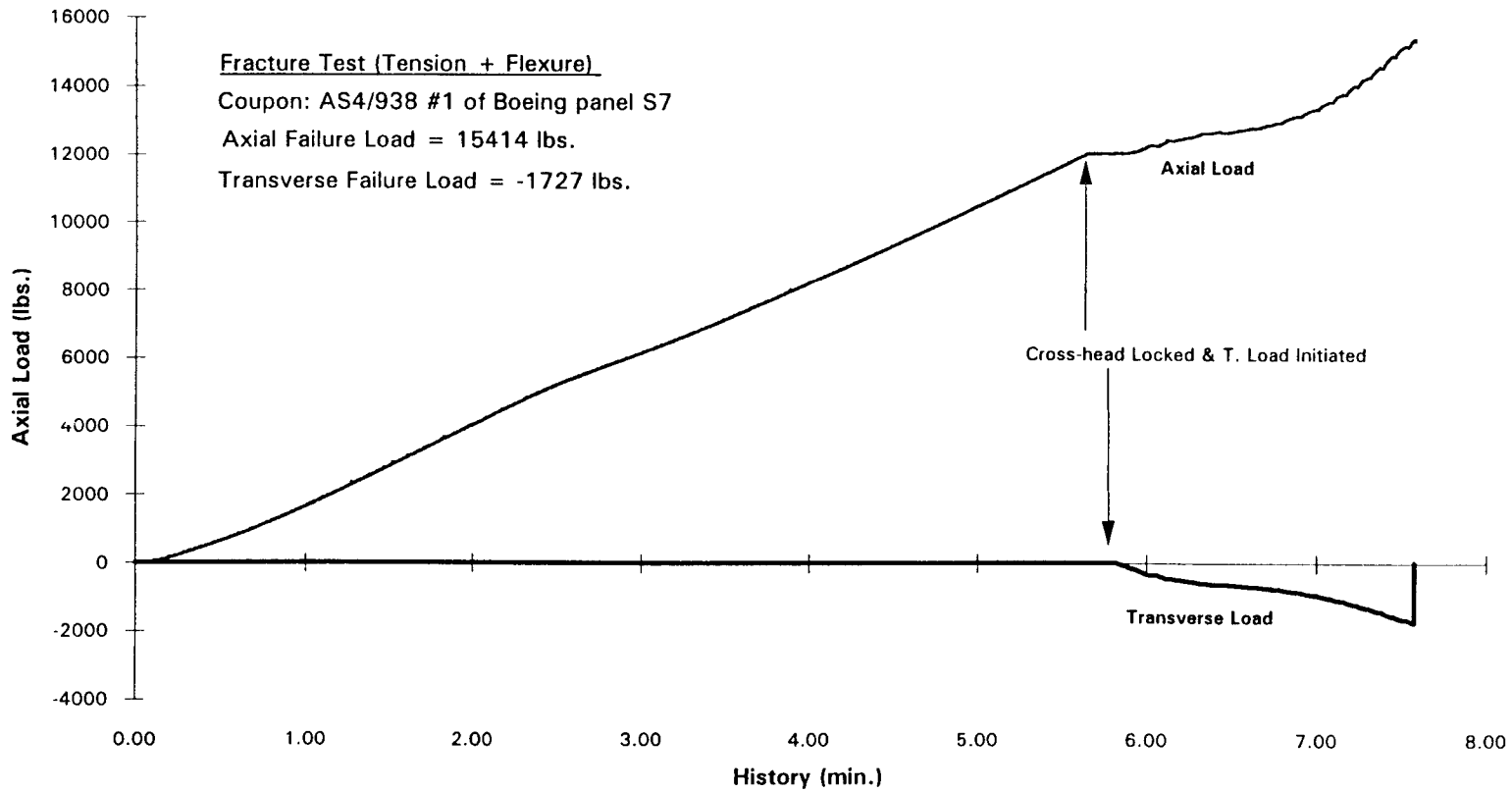
Fracture Test (Tension + Flexure)
Coupon: AS4/938 #1 of Boeing panel S7
Axial Failure Load = 15414 lbs.
Transverse Failure Load = -1727 lbs.
Axial Load
Cross-head Locked & T. Load Initiated
Transverse Load
Axial Load (lbs.)
16000
14000
12000
10000
8000
6000
4000
2000
0
-2000
-4000
0.00
1.00
2.00
3.00
4.00
5.00
6.00
7.00
8.00
History (min.)

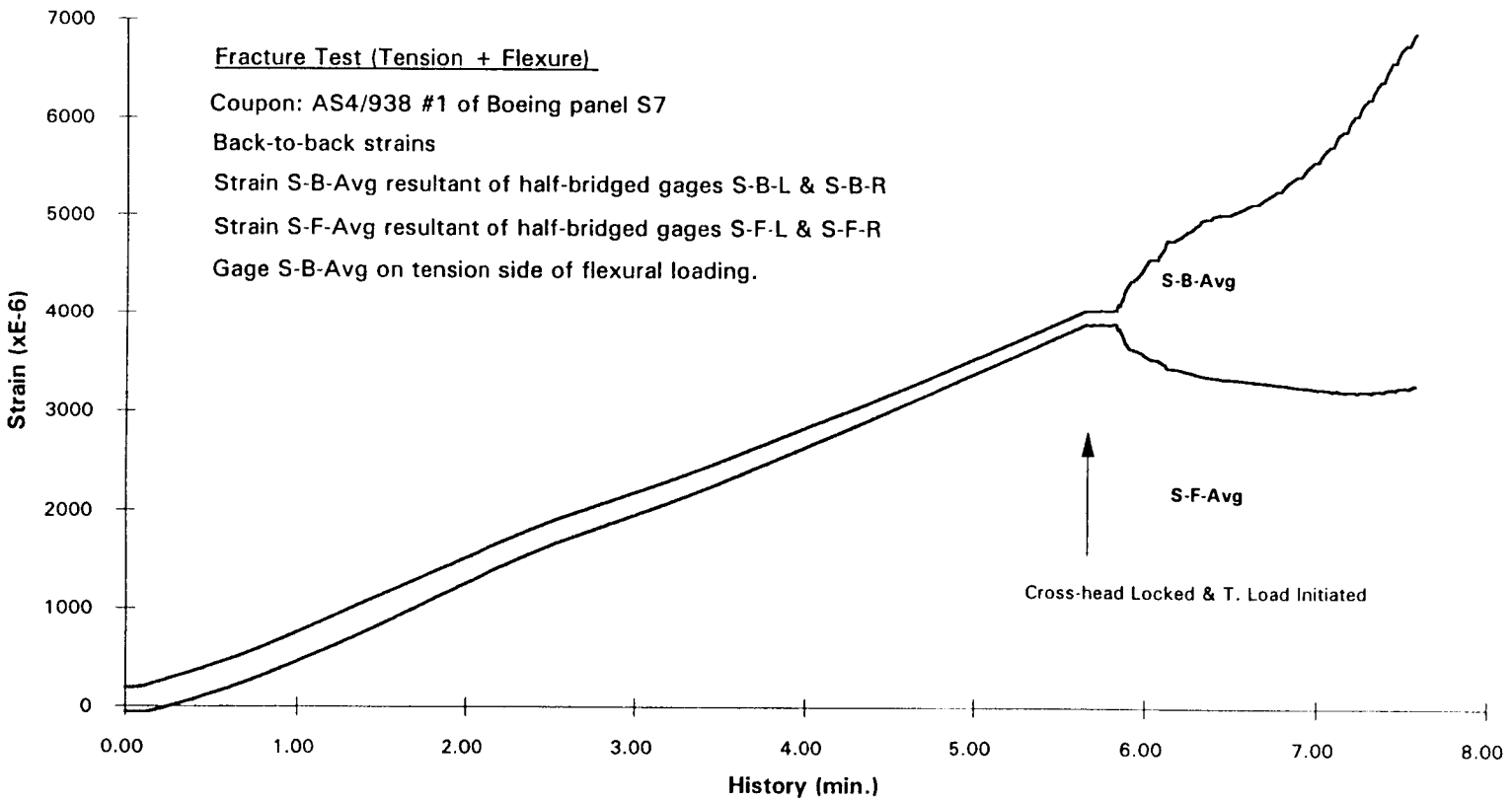
Fracture Test (Tension + Flexure)
Coupon: AS4/938 #1 of Boeing panel S7
Back-to-back strains
Strain S-B-Avg resultant of half-bridged gages S-B-L & S-B-R
Strain S-F-Avg resultant of half-bridged gages S-F-L & S-F-R
Gage S-B-Avg on tension side of flexural loading.
S-B-Avg
S-F-Avg
Cross-head Locked & T. Load Initiated
Strain (xE-6)
7000
6000
5000
4000
3000
2000
1000
0
0.00
1.00
2.00
3.00
4.00
5.00
6.00
7.00
8.00
History (min.)

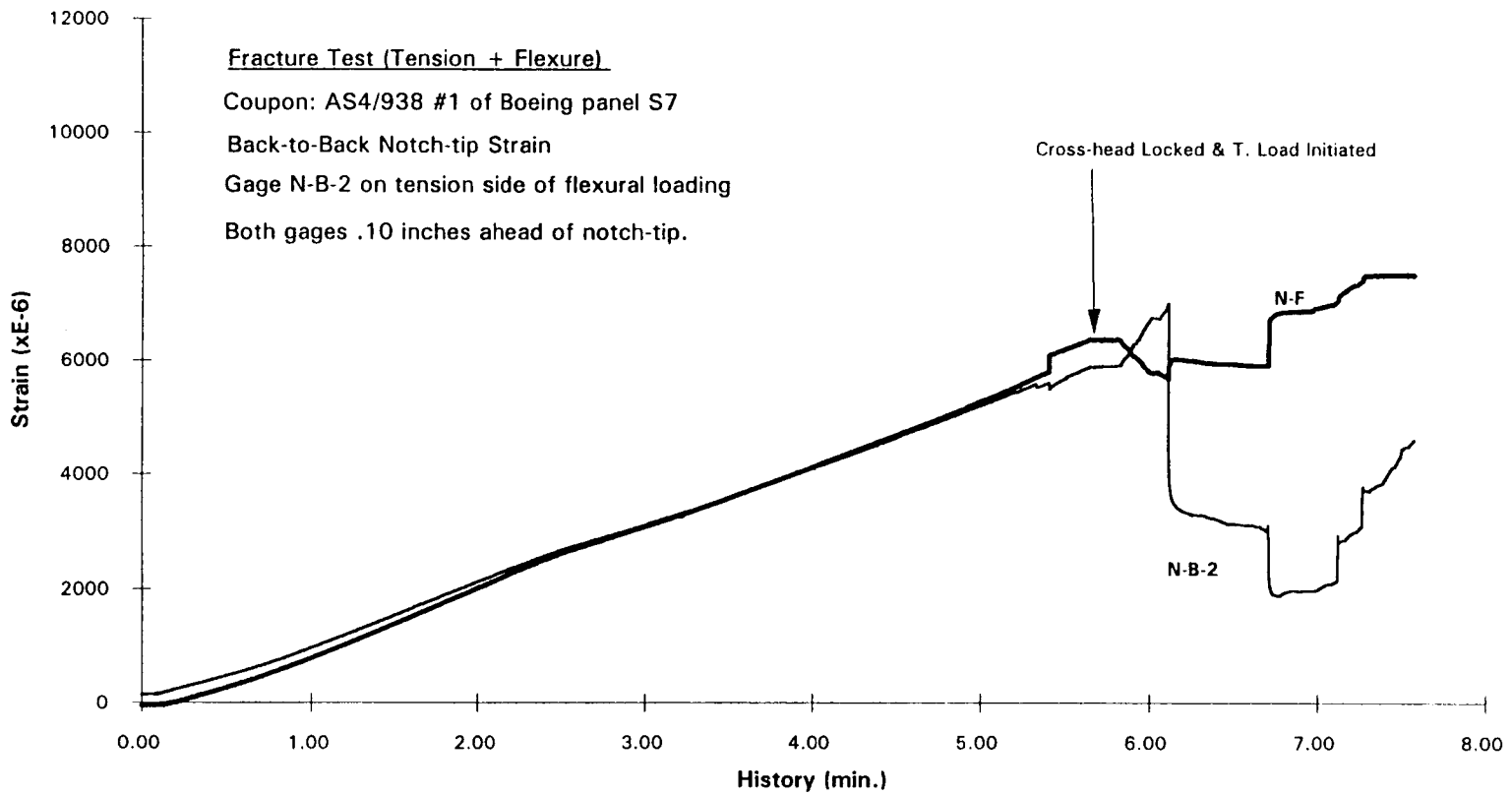
Fracture Test (Tension + Flexure)
Coupon: AS4/938 #1 of Boeing panel S7
Back-to-Back Notch-tip Strain
Gage N-B-2 on tension side of flexural loading
Both gages .10 inches ahead of notch-tip.
Cross-head Locked & T. Load Initiated
N-F
N-B-2
Strain (xE-6)
12000
10000
8000
6000
4000
2000
0
0.00
1.00
2.00
3.00
4.00
5.00
6.00
7.00
8.00
History (min.)

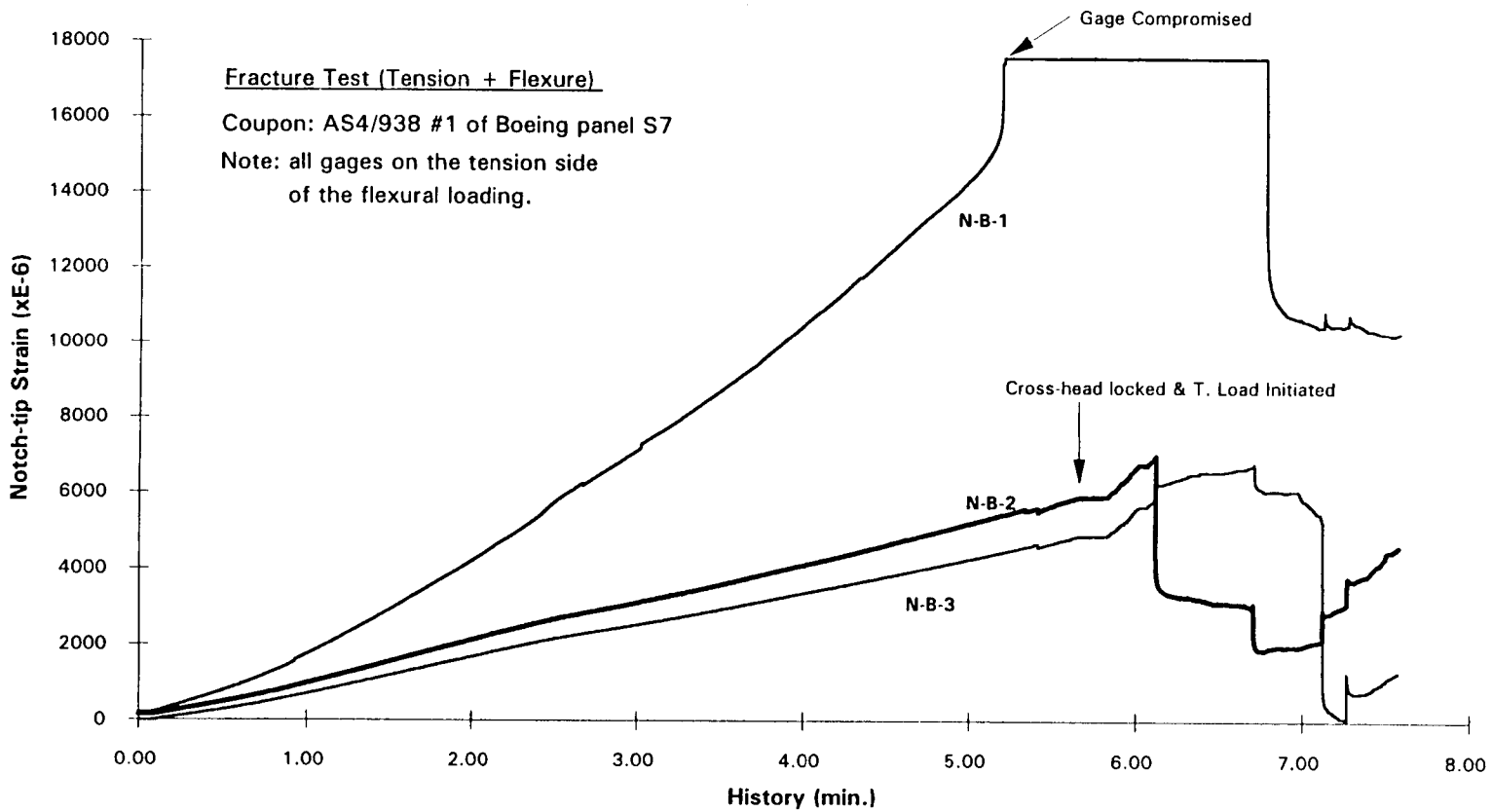
Fracture Test (Tension + Flexure)
Coupon: AS4/938 #1 of Boeing panel S7
Note: all gages on the tension side
of the flexural loading.
Gage Compromised
N-B-1
Cross-head locked & T. Load Initiated
N-B-2
N-B-3
Notch-tip Strain (xE-6)
18000
16000
14000
12000
10000
8000
6000
4000
2000
0
0.00
1.00
2.00
3.00
4.00
5.00
6.00
7.00
8.00
History (min.)

## Coupon AS4-2 & Gage Layout

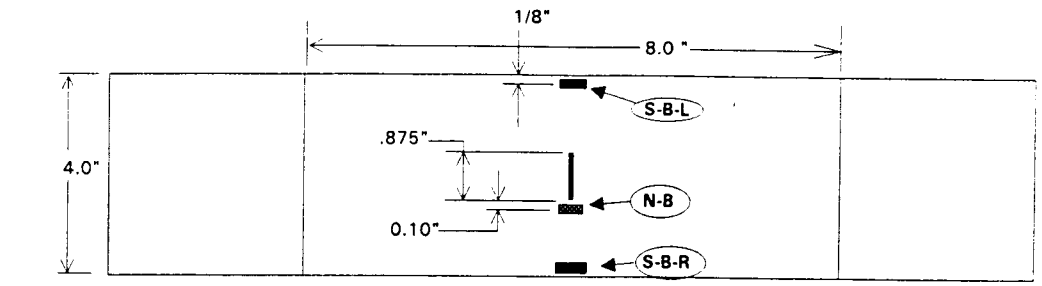


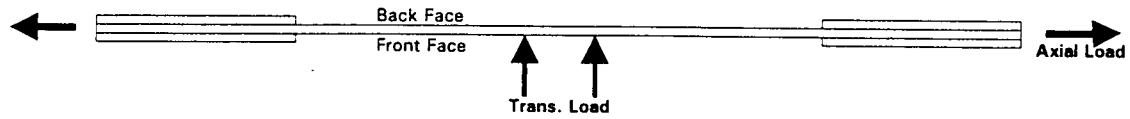


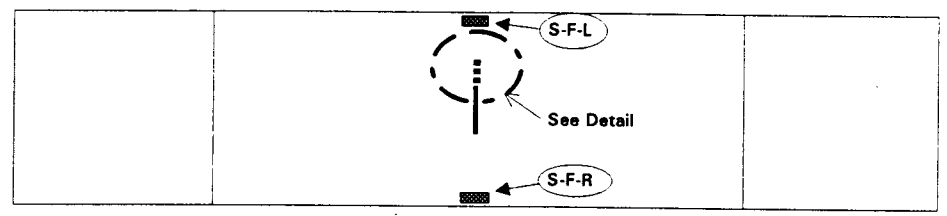


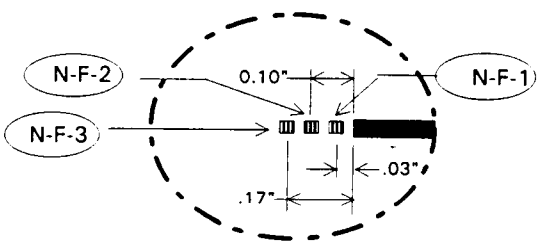


Notch-tip Gage Detail

## Gage Specifications

| Gage I.D. | Length(in.) | G.F. | Kt | Measure | Bridge Network |
|---|---|---|---|---|---|
| S-B-L | 0.125 | 2.08 | 0.70% | B-face strain | Half bridge, leg #1, with S-B-R |
| S-B-R | " | " | " | " | Half bridge, leg #3, with S-B-L |
| S-F-L | " | " | " | F-face strain | Half bridge, leg #3, with S-F-R |
| S-F-R | " | " | " | " | Half bridge, leg #1, with S-F-L |
| N-F-1 | 0.02 | 1.96 | 2.20% | Surf.-Strain | Qtr. bridge, leg #1 |
| N-F-2 | " | " | " | " | " " |
| N-F-3 | " | " | " | " | " " |
| N-B | 0.125 | 2.115 | 1.00% | " | " " |

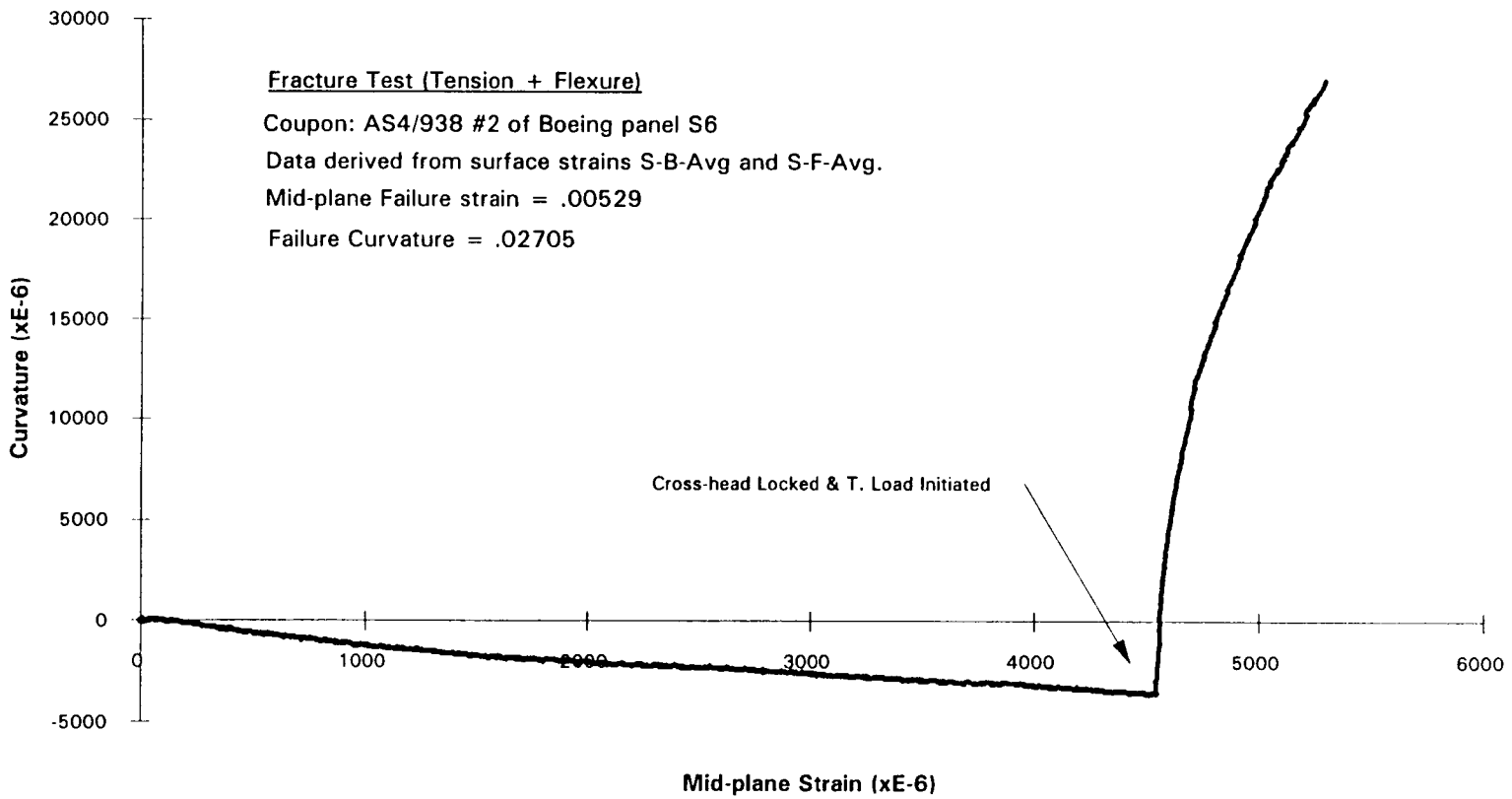
Fracture Test (Tension + Flexure)
Coupon: AS4/938 #2 of Boeing panel S6
Data derived from surface strains S-B-Avg and S-F-Avg.
Mid-plane Failure strain = .00529
Failure Curvature = .02705
Cross-head Locked & T. Load Initiated
Curvature (xE-6)
30000
25000
20000
15000
10000
5000
0
-5000
0
1000
2000
3000
4000
5000
6000
Mid-plane Strain (xE-6)

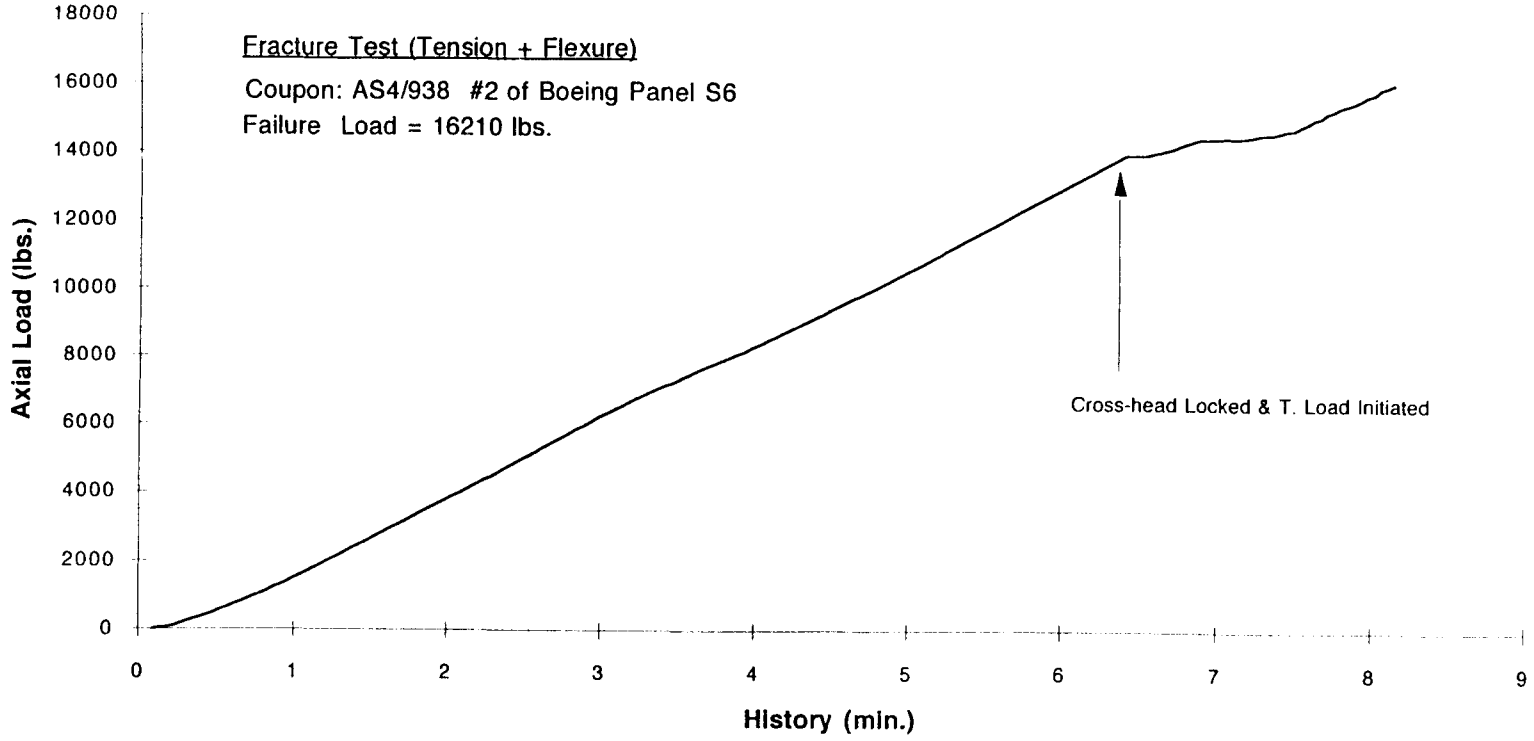
Fracture Test (Tension + Flexure)
Coupon: AS4/938 #2 of Boeing Panel S6
Failure Load = 16210 lbs.
Axial Load (lbs.)
18000
16000
14000
12000
10000
8000
6000
4000
2000
0
0
1
2
3
4
5
6
7
8
9
History (min.)
Cross-head Locked & T. Load Initiated

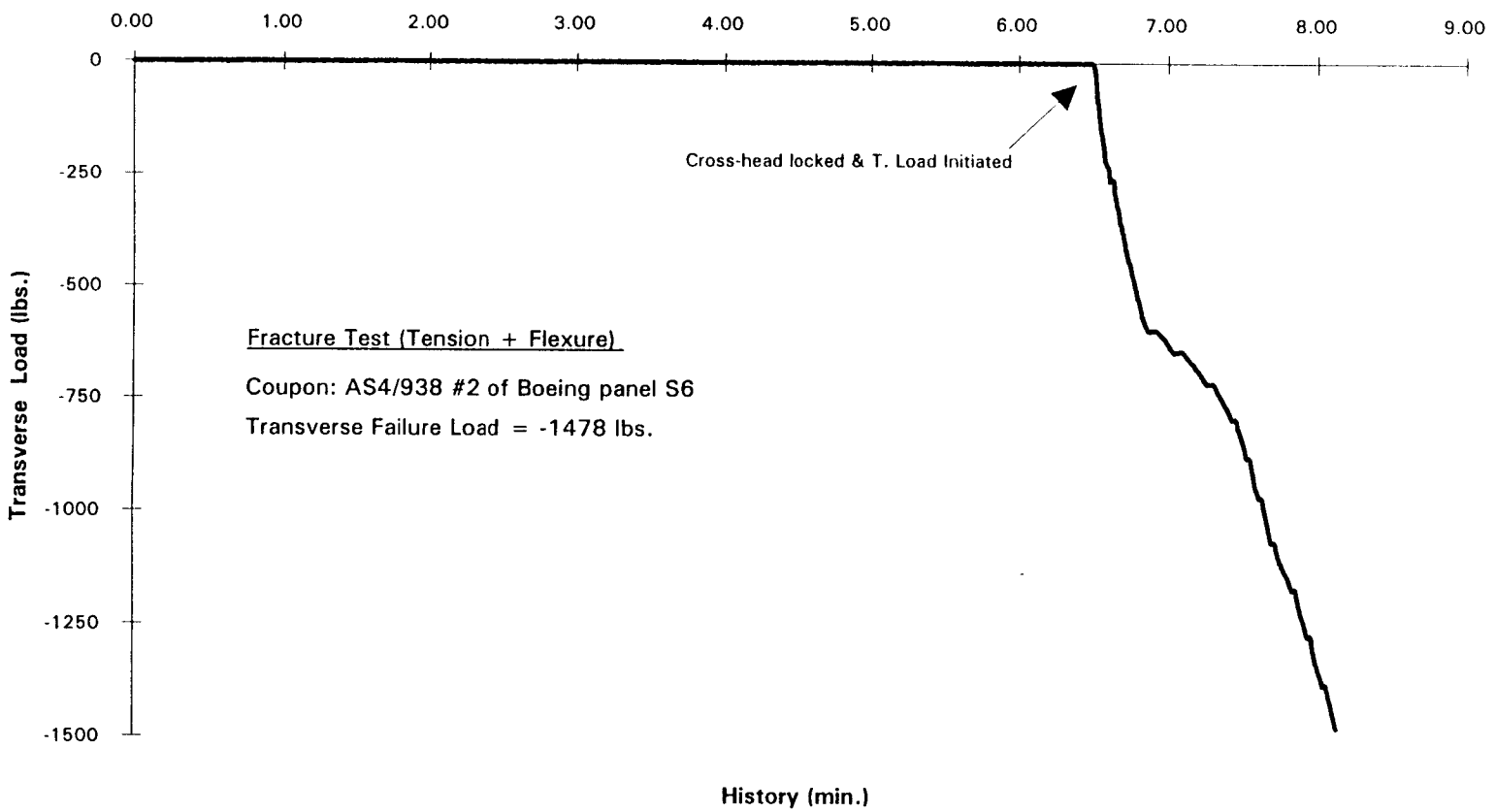
0.00
1.00
2.00
3.00
4.00
5.00
6.00
7.00
8.00
9.00
0
-250
-500
-750
-1000
-1250
-1500
Transverse Load (lbs.)
Cross-head locked & T. Load Initiated
Fracture Test (Tension + Flexure)
Coupon: AS4/938 #2 of Boeing panel S6
Transverse Failure Load = -1478 lbs.
History (min.)

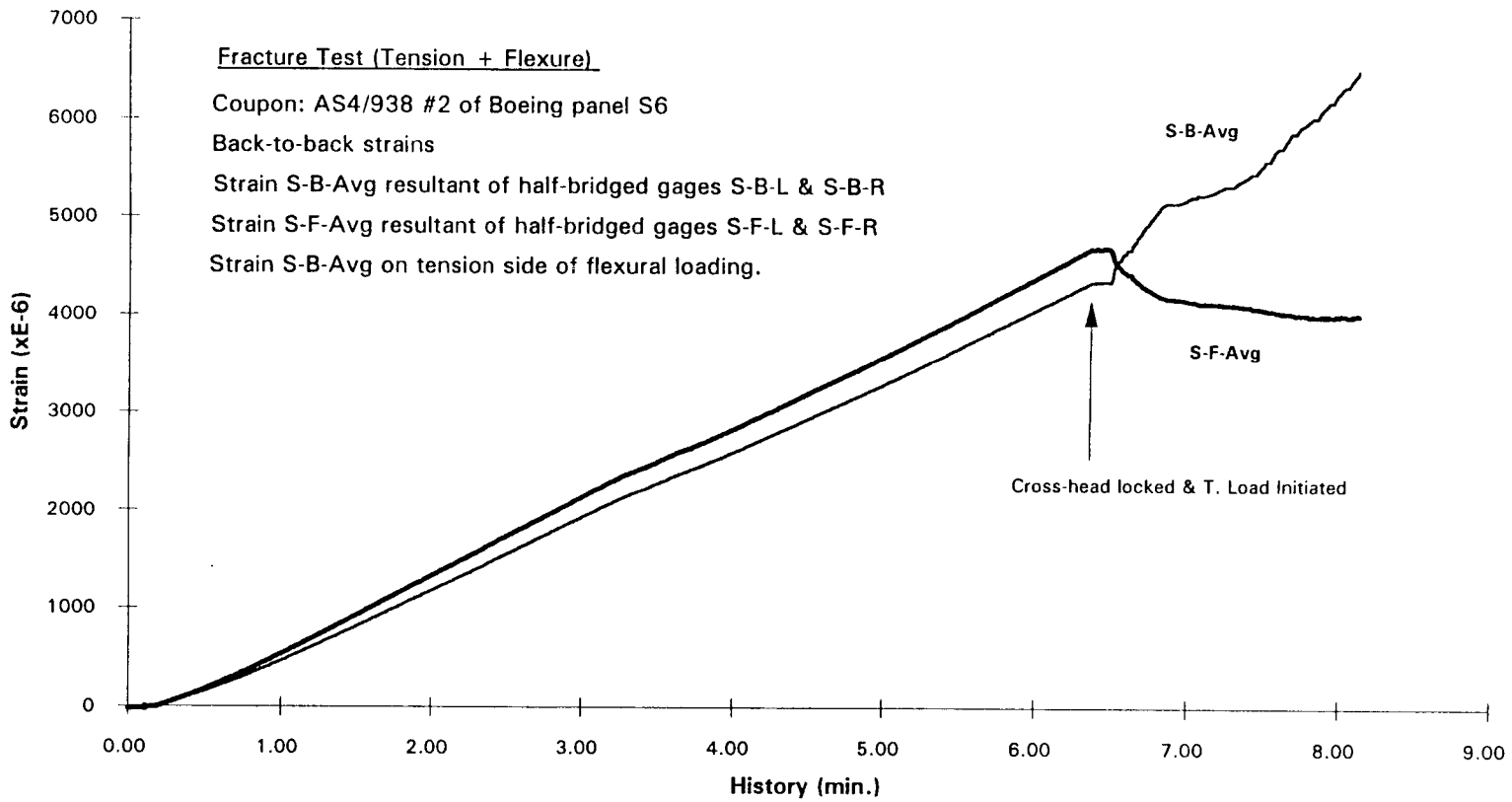
Fracture Test (Tension + Flexure)
Coupon: AS4/938 #2 of Boeing panel S6
Back-to-back strains
Strain S-B-Avg resultant of half-bridged gages S-B-L & S-B-R
Strain S-F-Avg resultant of half-bridged gages S-F-L & S-F-R
Strain S-B-Avg on tension side of flexural loading.
S-B-Avg
S-F-Avg
Cross-head locked & T. Load Initiated
Strain (xE-6)
7000
6000
5000
4000
3000
2000
1000
0
0.00
1.00
2.00
3.00
4.00
5.00
6.00
7.00
8.00
9.00
History (min.)

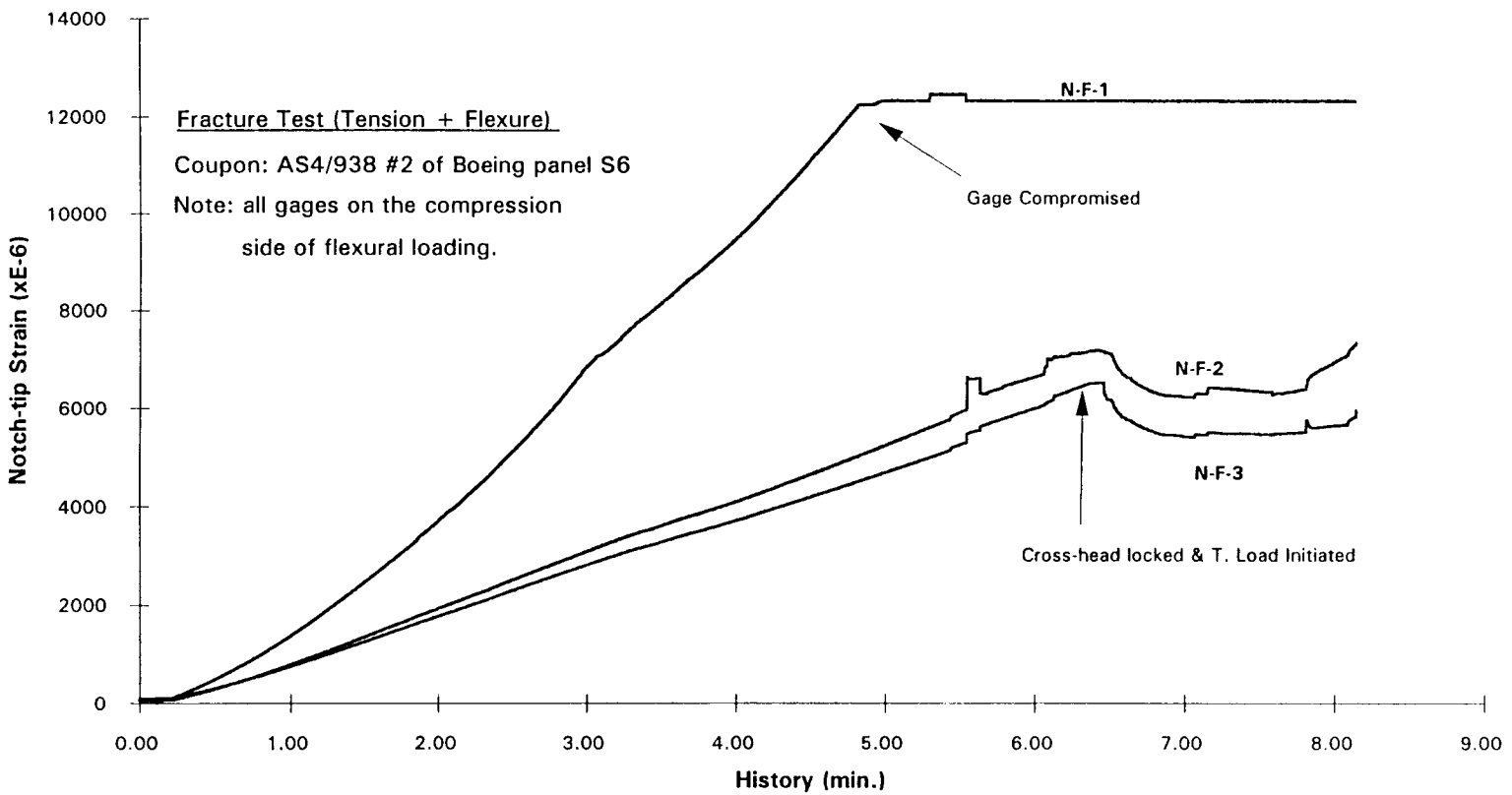
Fracture Test (Tension + Flexure)
Coupon: AS4/938 #2 of Boeing panel S6
Note: all gages on the compression
side of flexural loading.
N-F-1
Gage Compromised
N-F-2
N-F-3
Cross-head locked & T. Load Initiated
Notch-tip Strain (xE-6)
14000
12000
10000
8000
6000
4000
2000
0
0.00
1.00
2.00
3.00
4.00
5.00
6.00
7.00
8.00
9.00
History (min.)

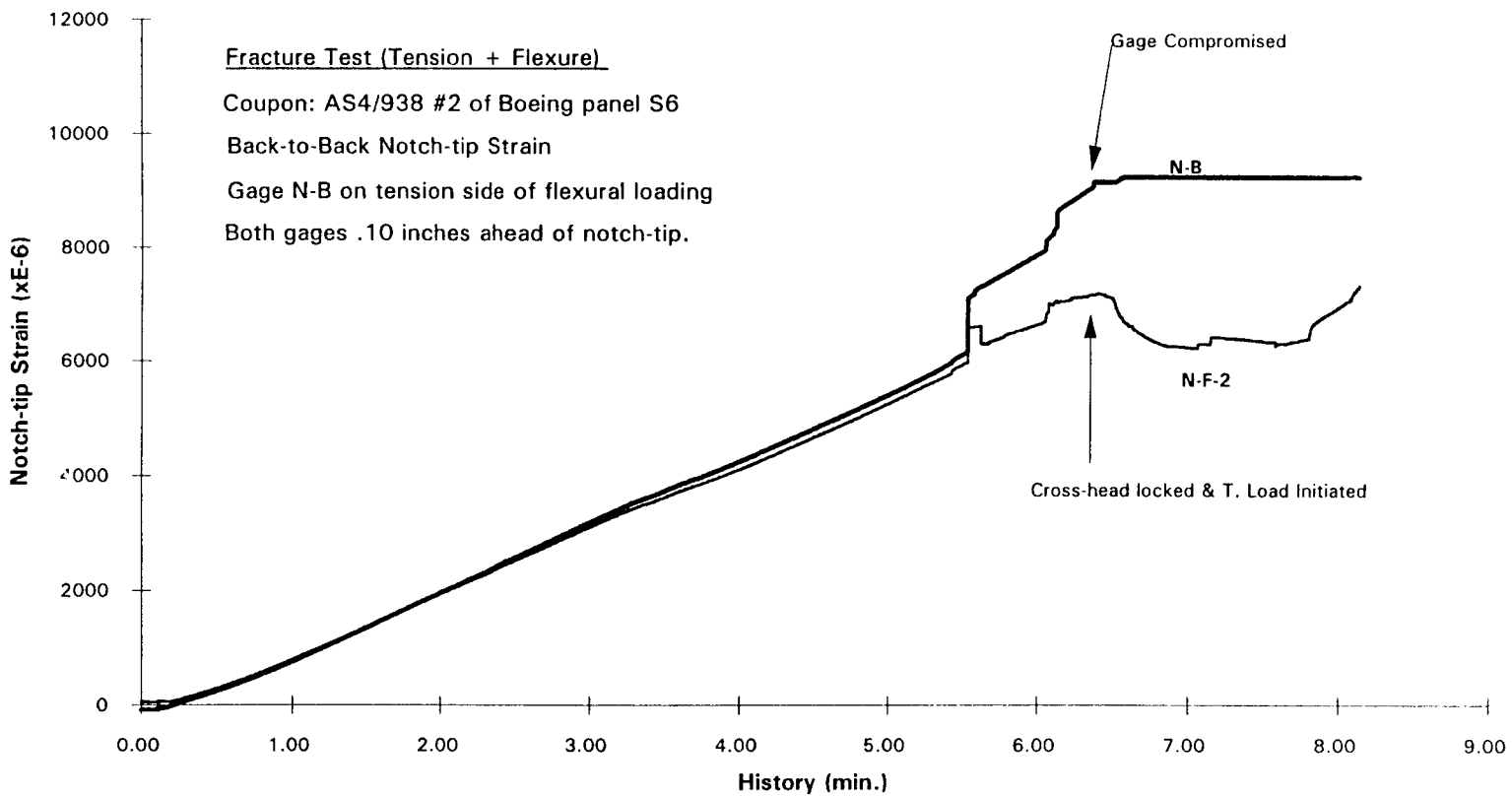
Fracture Test (Tension + Flexure)
Coupon: AS4/938 #2 of Boeing panel S6
Back-to-Back Notch-tip Strain
Gage N-B on tension side of flexural loading
Both gages .10 inches ahead of notch-tip.
Gage Compromised
N-B
N-F-2
Cross-head locked & T. Load Initiated
Notch-tip Strain (xE-6)
12000
10000
8000
6000
4000
2000
0
0.00
1.00
2.00
3.00
4.00
5.00
6.00
7.00
8.00
9.00
History (min.)

## Coupon AS4-4 & Gage Layout

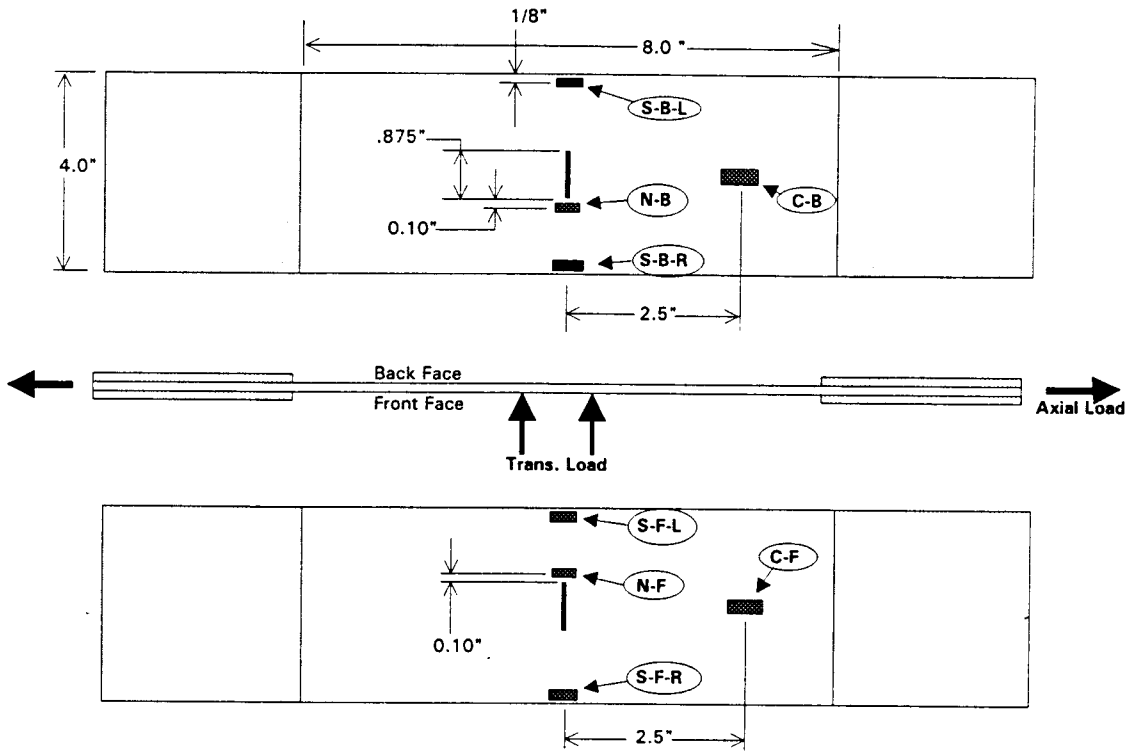


### Gage Specifications

| Gage I.D. | Length(in.) | G.F. | Kt | Measure | Bridge Network |
|---|---|---|---|---|---|
| S-B-L | 0.125 | 2.08 | 0.70% | B-face strain | Half bridge, leg #1, with S-B-R |
| S-B-R | " | " | " | " | Half bridge, leg #3, with S-B-L |
| S-F-L | " | " | " | F-face strain | Half bridge, leg #3, with S-F-R |
| S-F-R | " | " | " | " | Half bridge, leg #1, with S-F-L |
| C-B | 0.25 | 2.085 | 0.60% | Mid.-Strain | Half bridge, leg #3, with C-F |
| C-F | " | " | " | " | Half bridge, leg #1, with C-B |
| N-B | 0.125 | 2.115 | 1.00% | Surf. Strain | Qtr. bridge, leg #1 |
| N-F | " | " | " | " | " " |

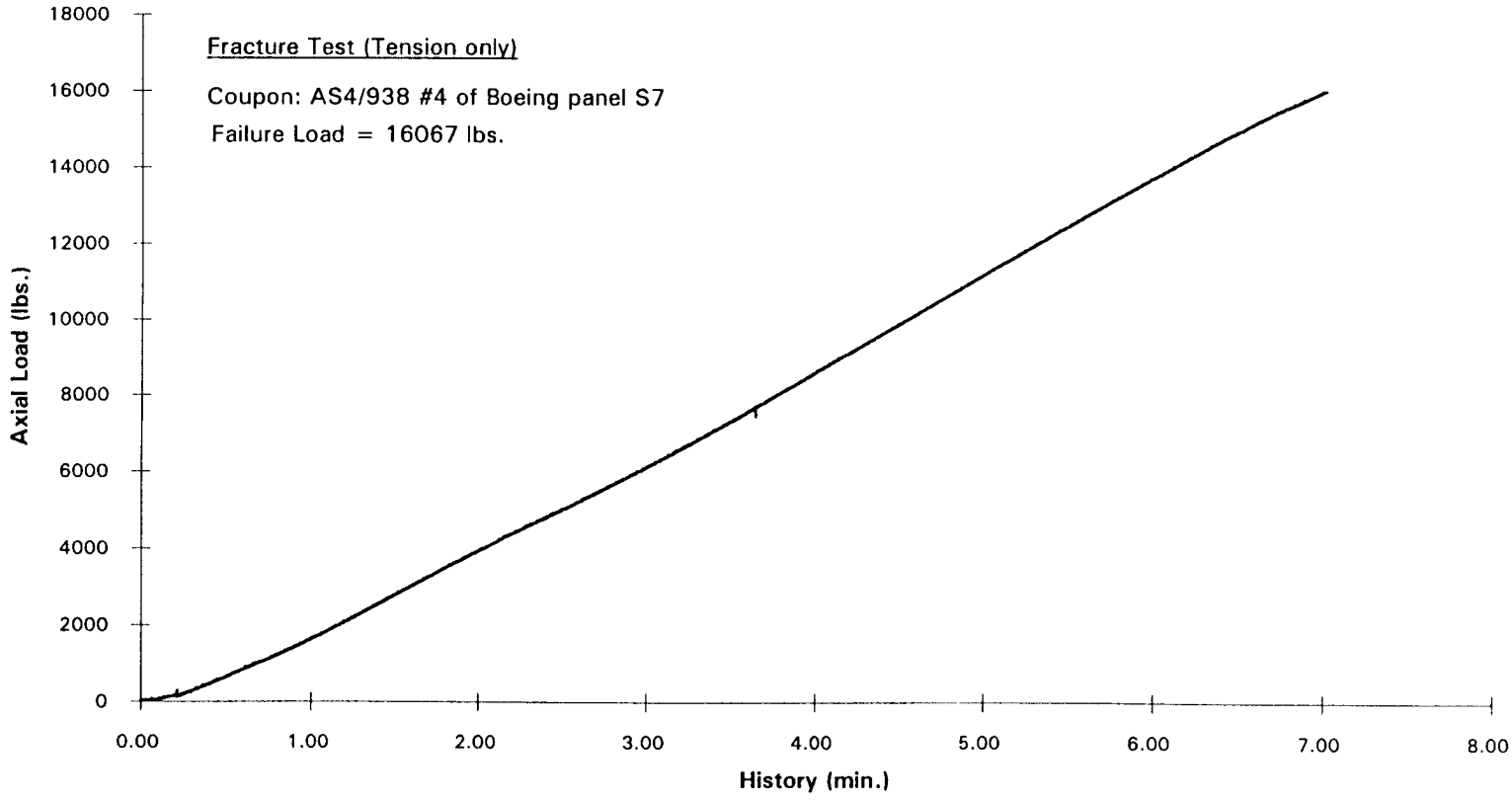
Fracture Test (Tension only)
Coupon: AS4/938 #4 of Boeing panel S7
Failure Load = 16067 lbs.
Axial Load (lbs.)
18000
16000
14000
12000
10000
8000
6000
4000
2000
0
0.00
1.00
2.00
3.00
4.00
5.00
6.00
7.00
8.00
History (min.)

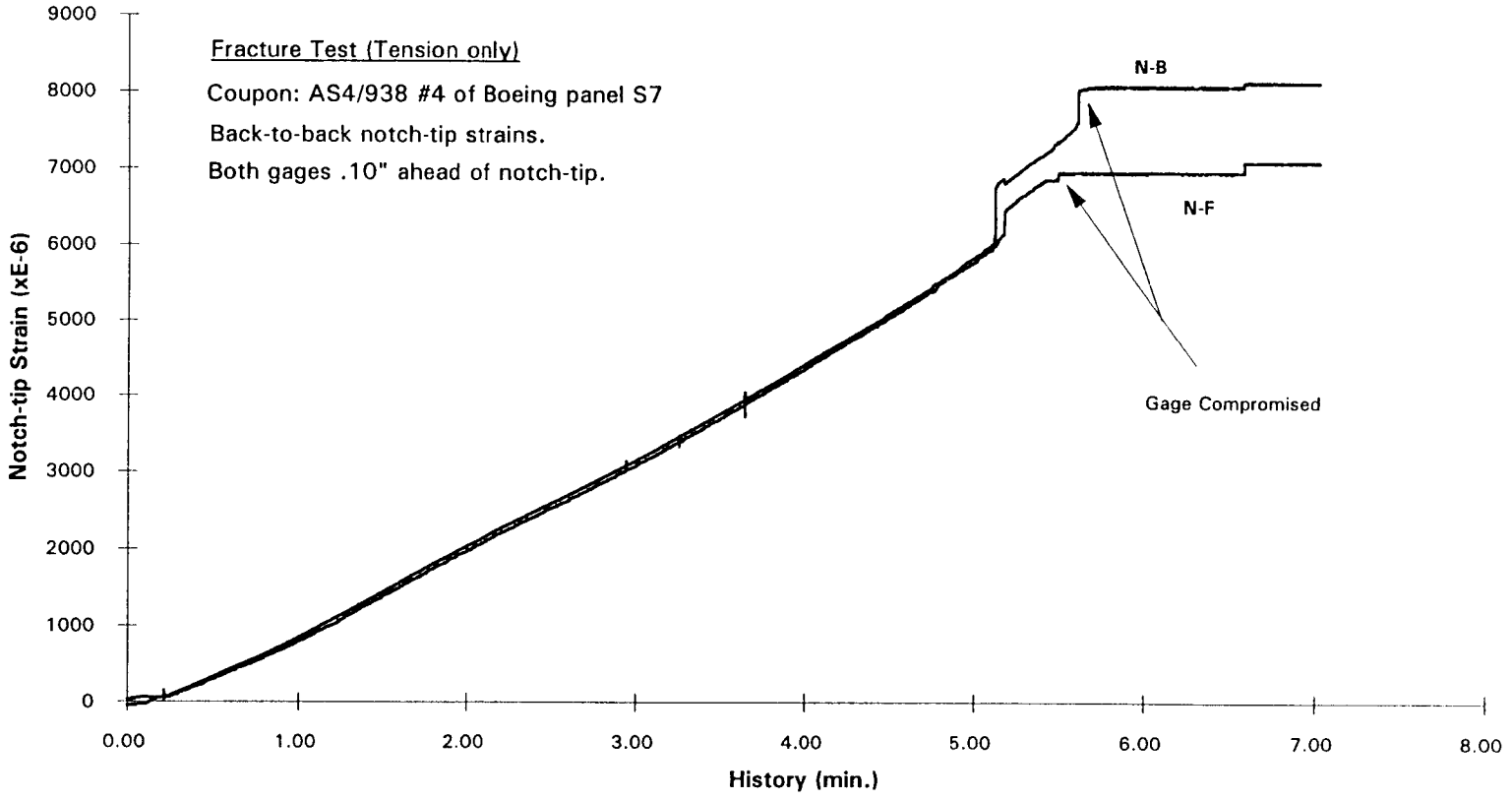
Fracture Test (Tension only)
Coupon: AS4/938 #4 of Boeing panel S7
Back-to-back notch-tip strains.
Both gages .10" ahead of notch-tip.
N-B
N-F
Gage Compromised
Notch-tip Strain (xE-6)
9000
8000
7000
6000
5000
4000
3000
2000
1000
0
0.00
1.00
2.00
3.00
4.00
5.00
6.00
7.00
8.00
History (min.)

## Coupon AS4-5 & Gage Layout

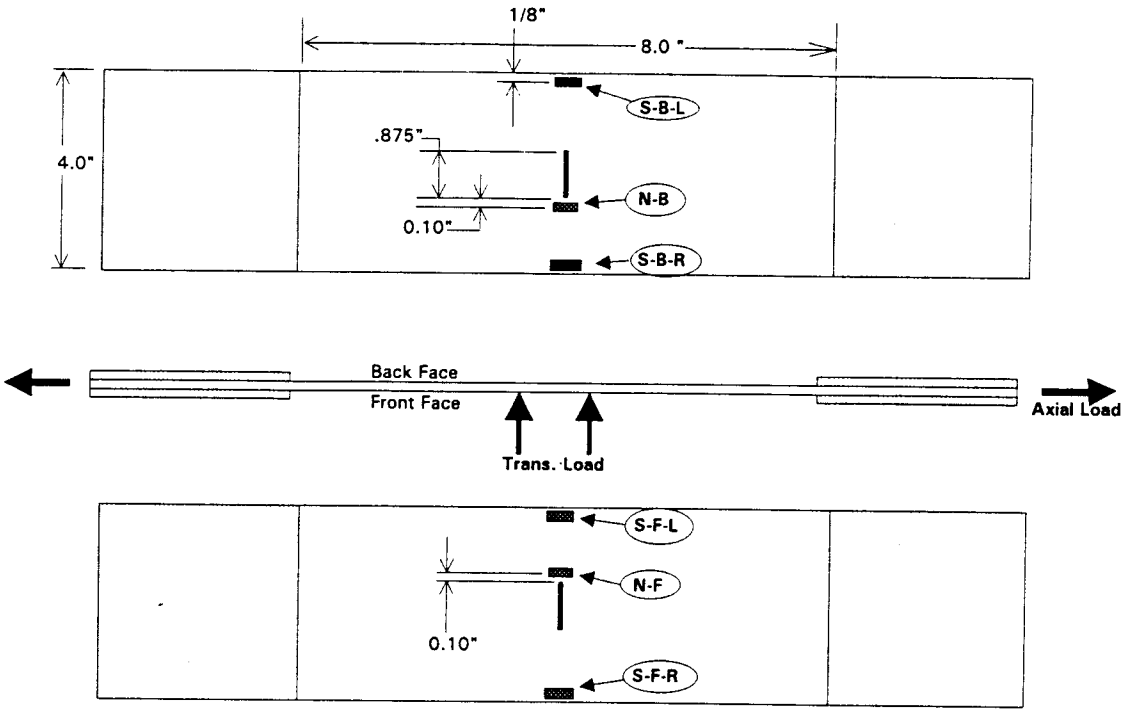


## Gage Specifications

| Gage I.D. | Length(in.) | G.F. | Kt | Measure | Bridge Network |
|---|---|---|---|---|---|
| S-B-L | 0.125 | 2.115 | 1.00% | Surf. Strain | Qtr. bridge, leg #1 |
| S-B-R | " | " | " | " | " " |
| S-F-L | " | " | " | " | " " |
| S-F-R | " | " | " | " | " " |
| N-B | " | " | " | " | " " |
| N-F | " | " | " | " | " " |

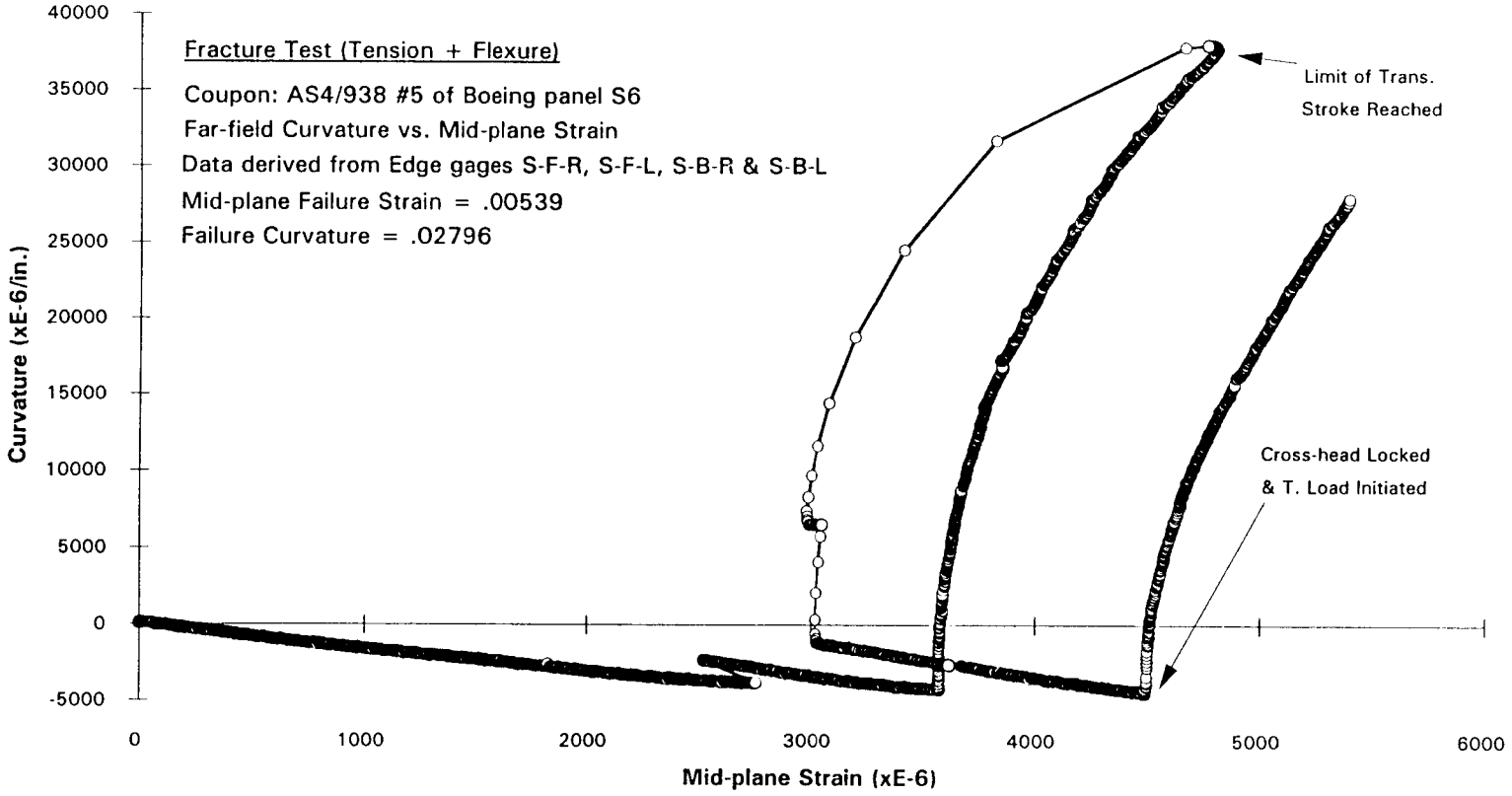
Fracture Test (Tension + Flexure)
Coupon: AS4/938 #5 of Boeing panel S6
Far-field Curvature vs. Mid-plane Strain
Data derived from Edge gages S-F-R, S-F-L, S-B-R & S-B-L
Mid-plane Failure Strain = .00539
Failure Curvature = .02796
Limit of Trans.
Stroke Reached
Cross-head Locked
& T. Load Initiated
Curvature (xE-6/in.)
Mid-plane Strain (xE-6)
40000
35000
30000
25000
20000
15000
10000
5000
0
-5000
0
1000
2000
3000
4000
5000
6000

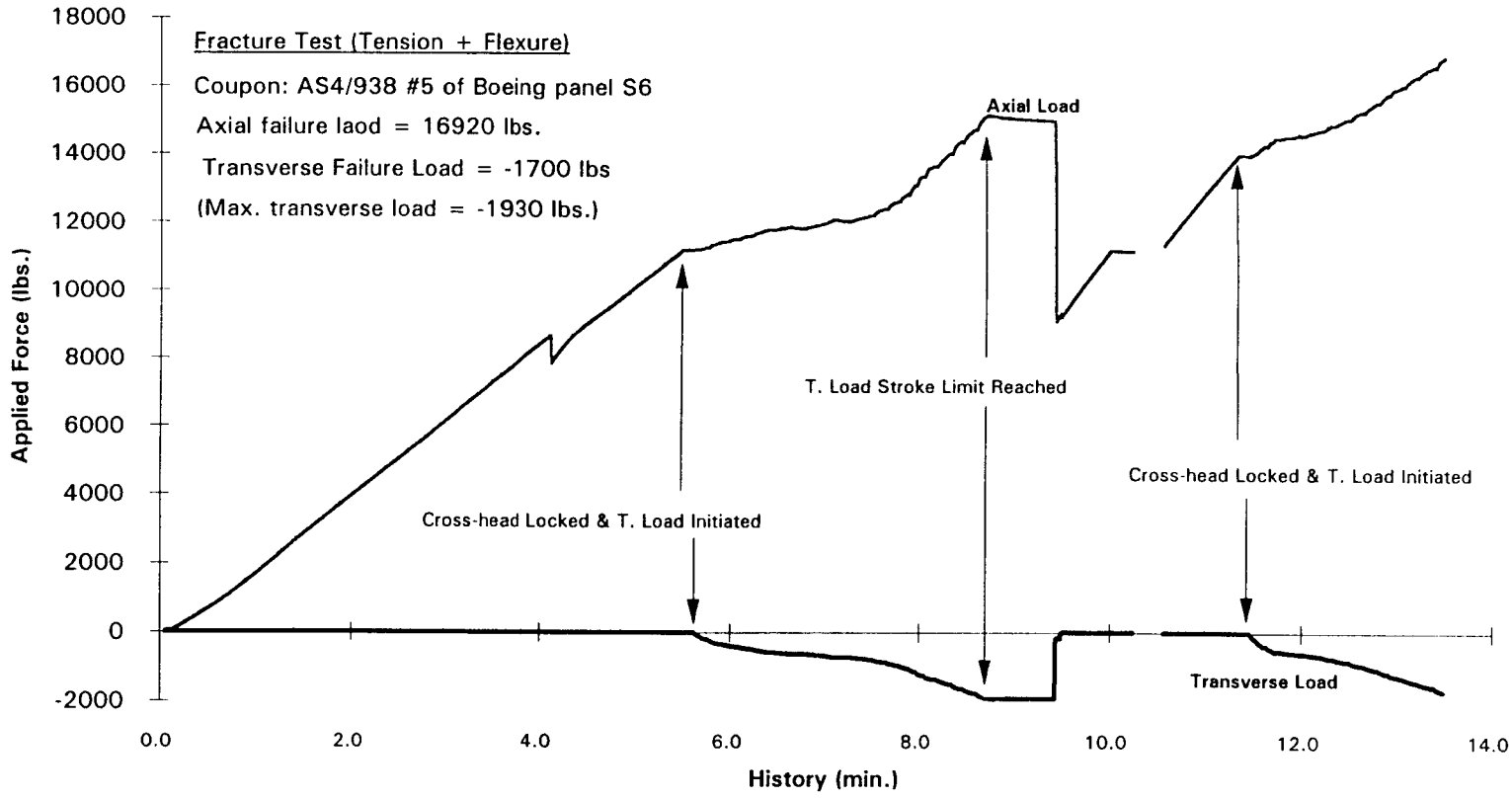
Fracture Test (Tension + Flexure)
Coupon: AS4/938 #5 of Boeing panel S6
Axial failure laod = 16920 lbs.
Transverse Failure Load = -1700 lbs
(Max. transverse load = -1930 lbs.)
Axial Load
T. Load Stroke Limit Reached
Cross-head Locked & T. Load Initiated
Cross-head Locked & T. Load Initiated
Transverse Load
Applied Force (lbs.)
18000
16000
14000
12000
10000
8000
6000
4000
2000
0
-2000
0.0
2.0
4.0
6.0
8.0
10.0
12.0
14.0
History (min.)

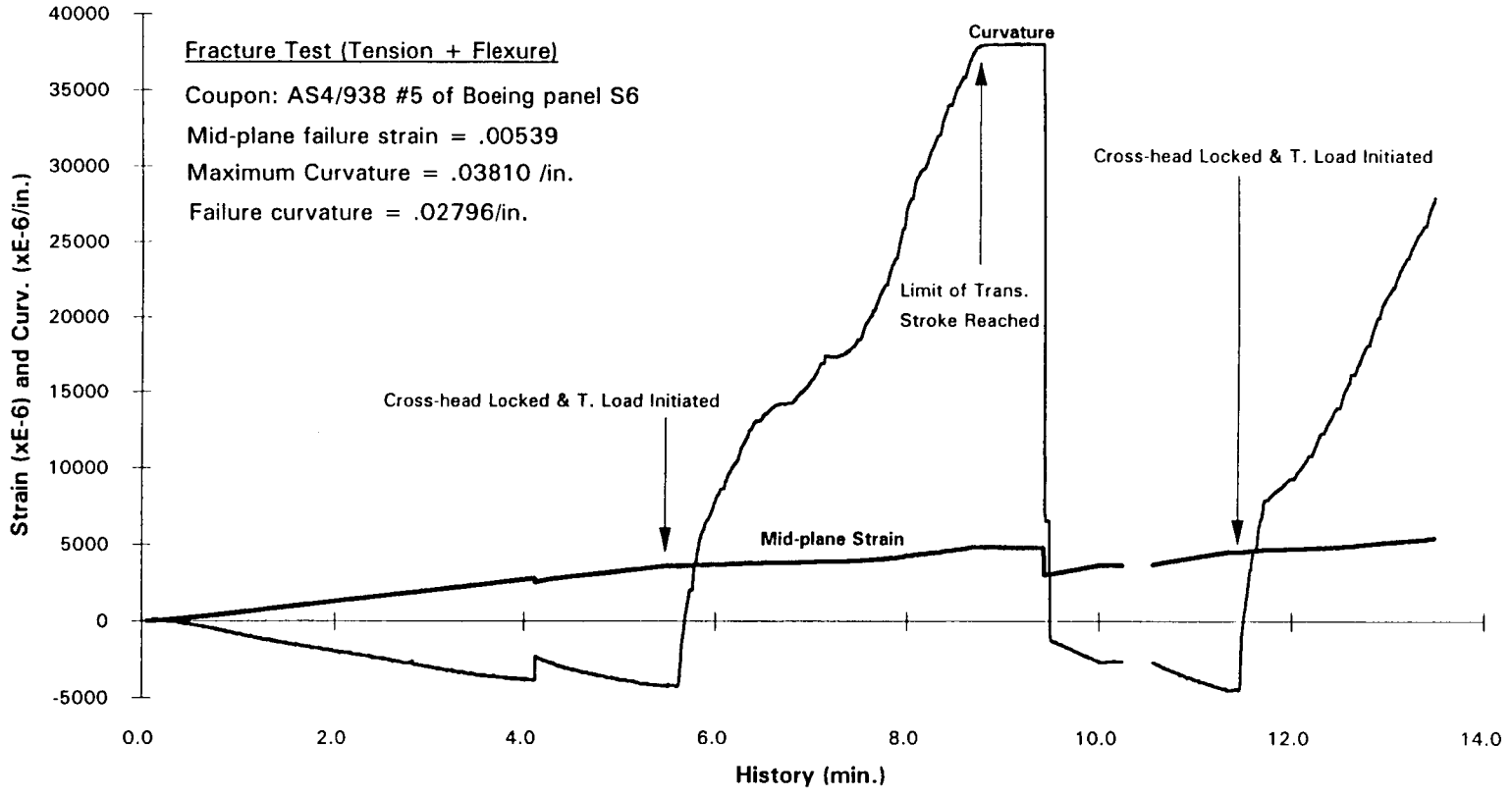
Fracture Test (Tension + Flexure)
Coupon: AS4/938 #5 of Boeing panel S6
Mid-plane failure strain = .00539
Maximum Curvature = .03810 /in.
Failure curvature = .02796/in.
Curvature
Limit of Trans.
Stroke Reached
Cross-head Locked & T. Load Initiated
Cross-head Locked & T. Load Initiated
Mid-plane Strain
Strain (xE-6) and Curv. (xE-6/in.)
History (min.)
40000
35000
30000
25000
20000
15000
10000
5000
0
-5000
0.0
2.0
4.0
6.0
8.0
10.0
12.0
14.0

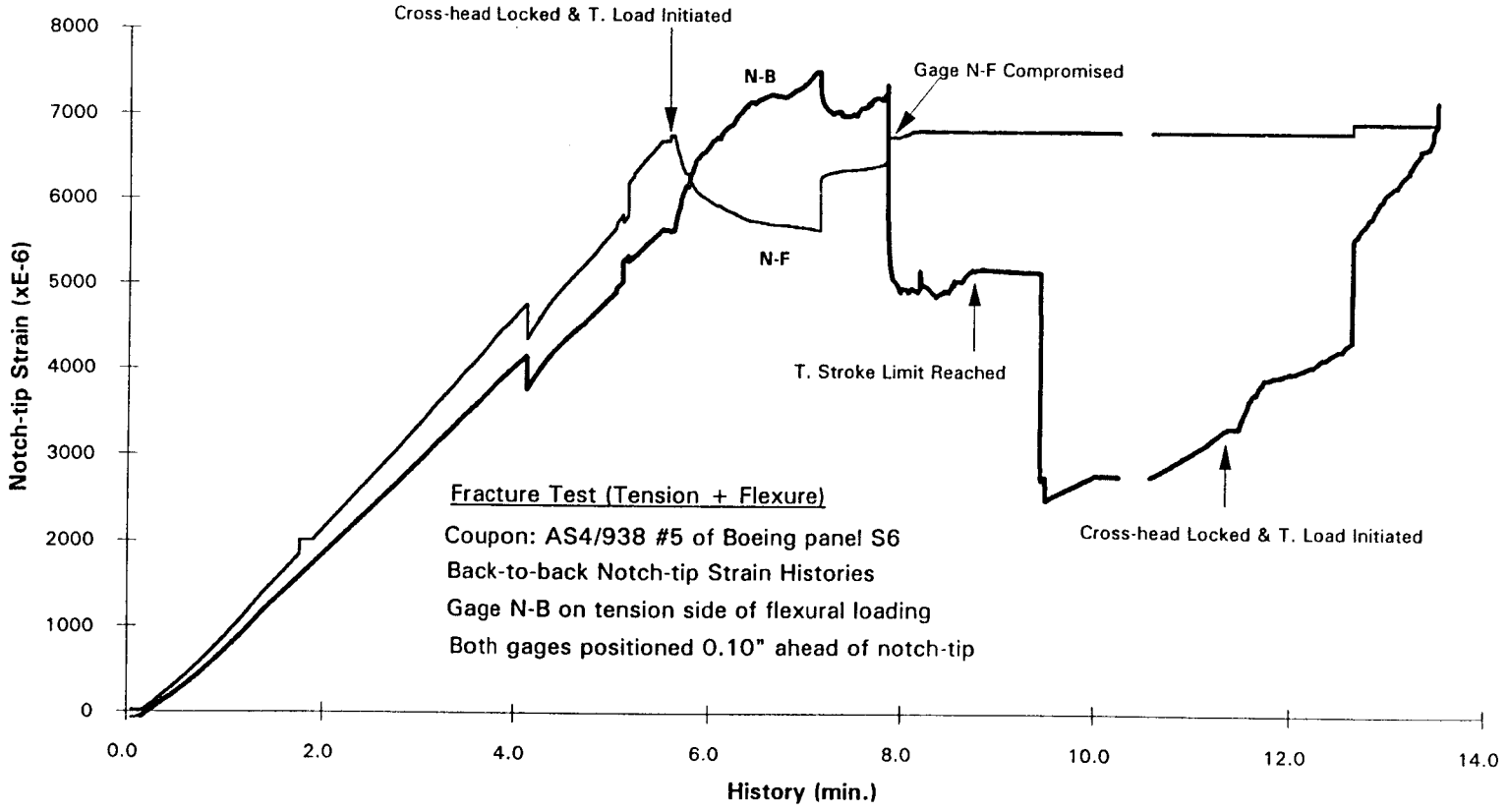
Cross-head Locked & T. Load Initiated
N-B
Gage N-F Compromised
N-F
T. Stroke Limit Reached
Cross-head Locked & T. Load Initiated
Fracture Test (Tension + Flexure)
Coupon: AS4/938 #5 of Boeing panel S6
Back-to-back Notch-tip Strain Histories
Gage N-B on tension side of flexural loading
Both gages positioned 0.10" ahead of notch-tip
Notch-tip Strain (xE-6)
8000
7000
6000
5000
4000
3000
2000
1000
0
0.0
2.0
4.0
6.0
8.0
10.0
12.0
14.0
History (min.)

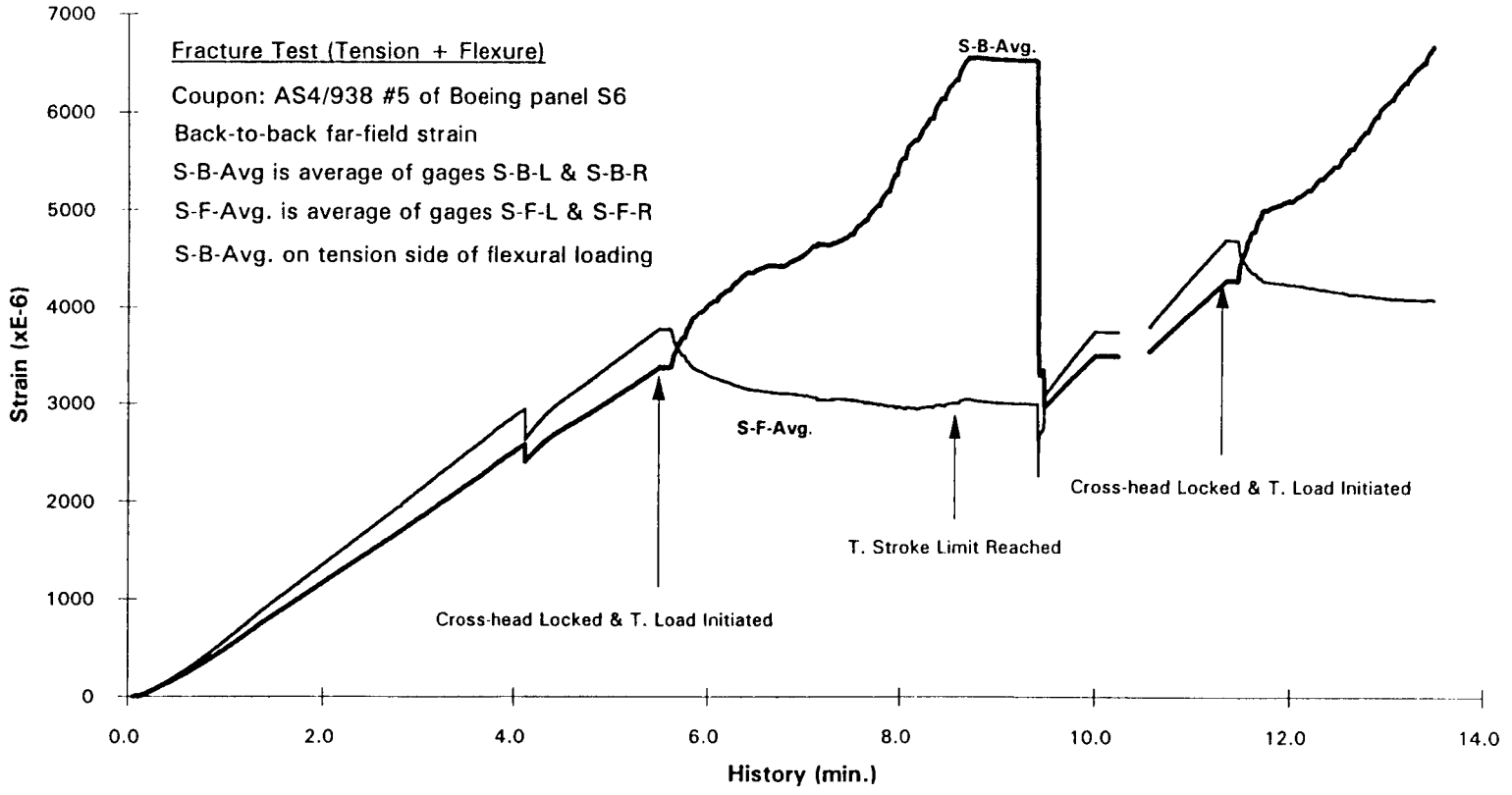
Fracture Test (Tension + Flexure)
Coupon: AS4/938 #5 of Boeing panel S6
Back-to-back far-field strain
S-B-Avg is average of gages S-B-L & S-B-R
S-F-Avg. is average of gages S-F-L & S-F-R
S-B-Avg. on tension side of flexural loading
S-B-Avg.
S-F-Avg.
Cross-head Locked & T. Load Initiated
T. Stroke Limit Reached
Cross-head Locked & T. Load Initiated
Strain (xE-6)
History (min.)
7000
6000
5000
4000
3000
2000
1000
0
0.0
2.0
4.0
6.0
8.0
10.0
12.0
14.0

## Coupon AS4-6 & Gage Layout

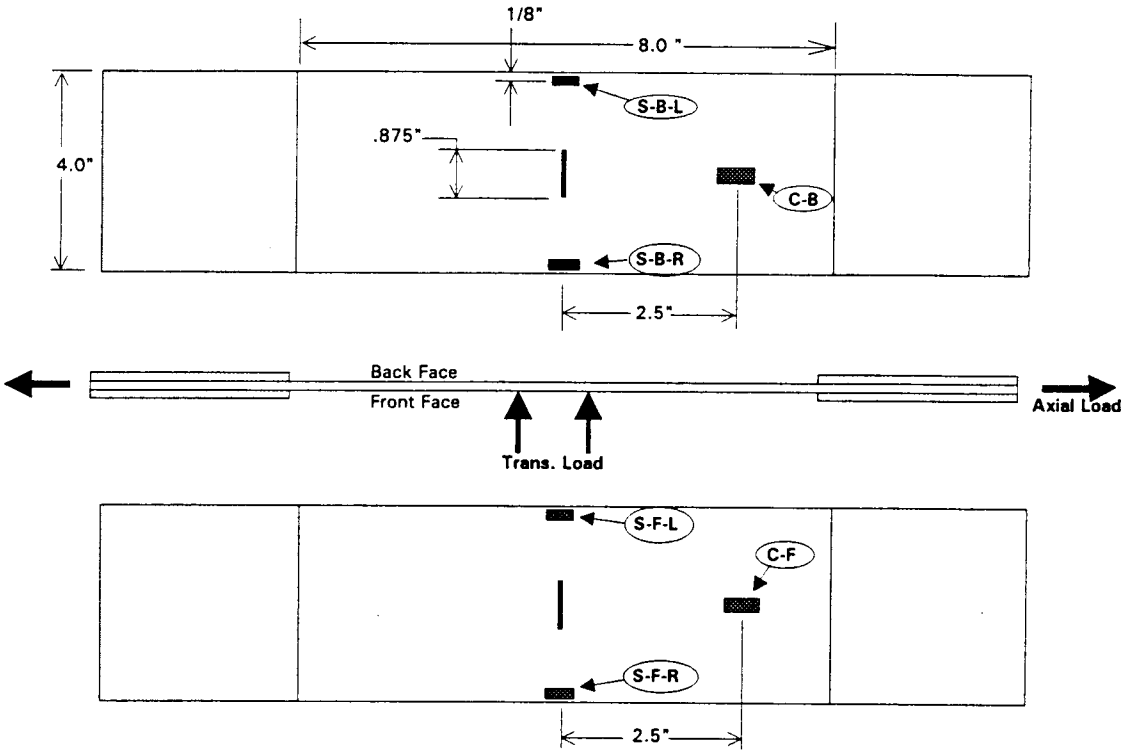


## Gage Specifications

| Gage I.D. | Length(in.) | G.F. | Kt | Measure | Bridge Network |
|---|---|---|---|---|---|
| S-B-L | 0.125 | 2.08 | 0.70% | Surf. Strain | Qtr. bridge, leg #1. |
| S-B-R | " | " | " | " | " " |
| S-F-L | " | " | " | " | " " |
| S-F-R | " | " | " | " | " " |
| C-B | 0.25 | 2.085 | 0.60% | " | " " |
| C-F | " | " | " | " | " " |

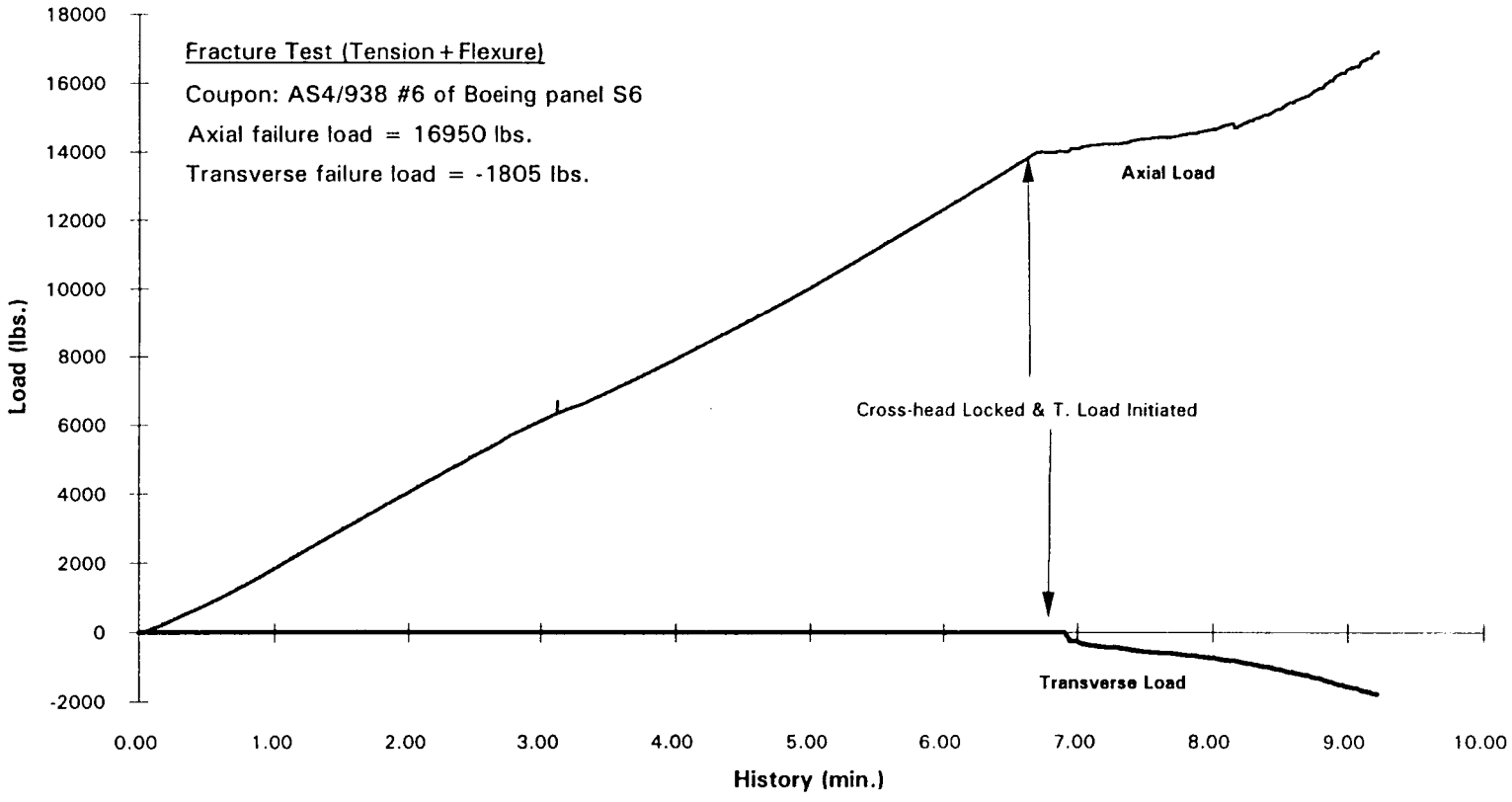
Fracture Test (Tension + Flexure)
Coupon: AS4/938 #6 of Boeing panel S6
Axial failure load = 16950 lbs.
Transverse failure load = -1805 lbs.
Axial Load
Cross-head Locked & T. Load Initiated
Transverse Load
Load (lbs.)
History (min.)
18000
16000
14000
12000
10000
8000
6000
4000
2000
0
-2000
0.00
1.00
2.00
3.00
4.00
5.00
6.00
7.00
8.00
9.00
10.00

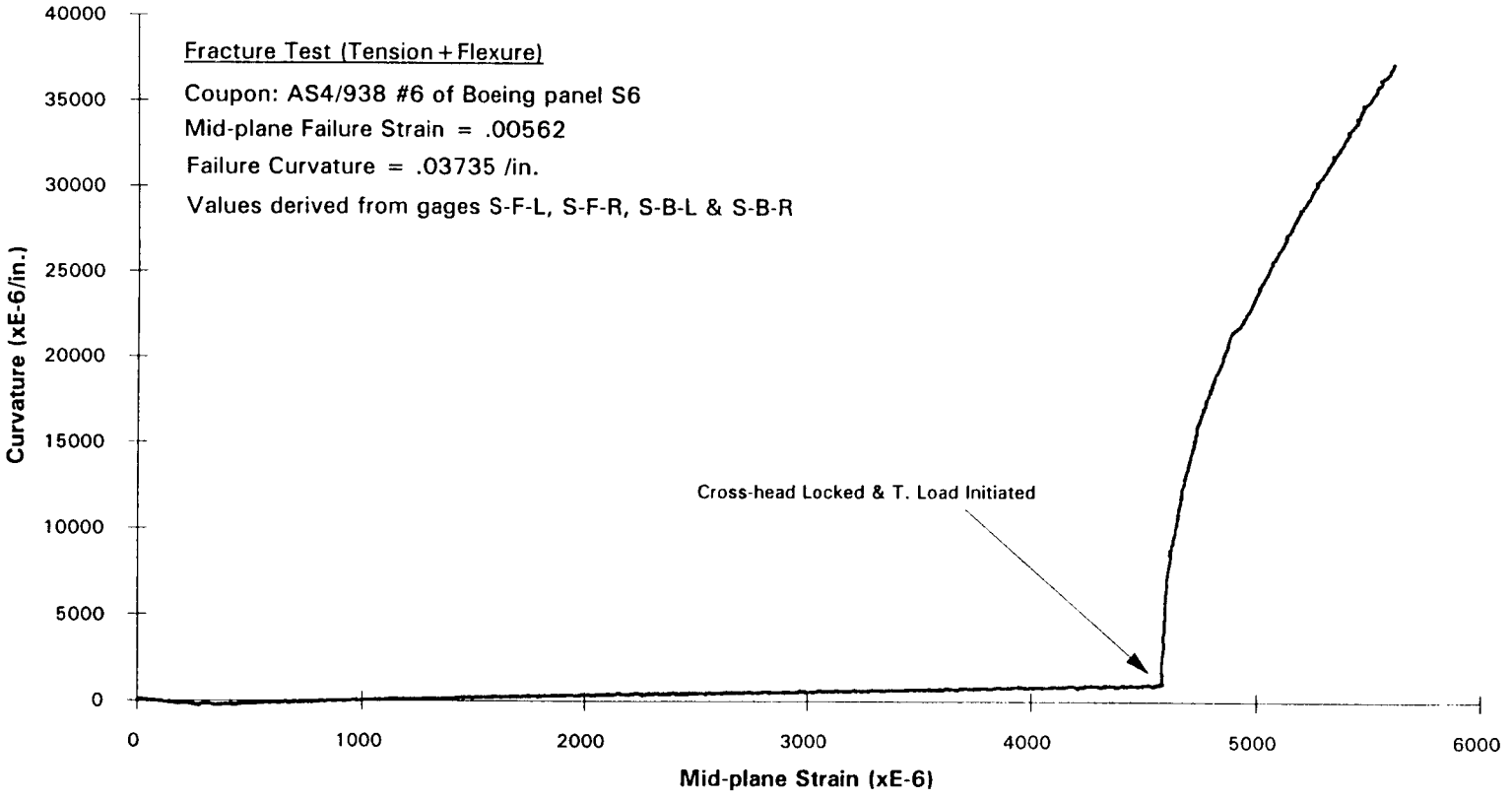
Fracture Test (Tension + Flexure)
Coupon: AS4/938 #6 of Boeing panel S6
Mid-plane Failure Strain = .00562
Failure Curvature = .03735 /in.
Values derived from gages S-F-L, S-F-R, S-B-L & S-B-R
Cross-head Locked & T. Load Initiated
Curvature (xE-6/in.)
Mid-plane Strain (xE-6)
40000
35000
30000
25000
20000
15000
10000
5000
0
0
1000
2000
3000
4000
5000
6000

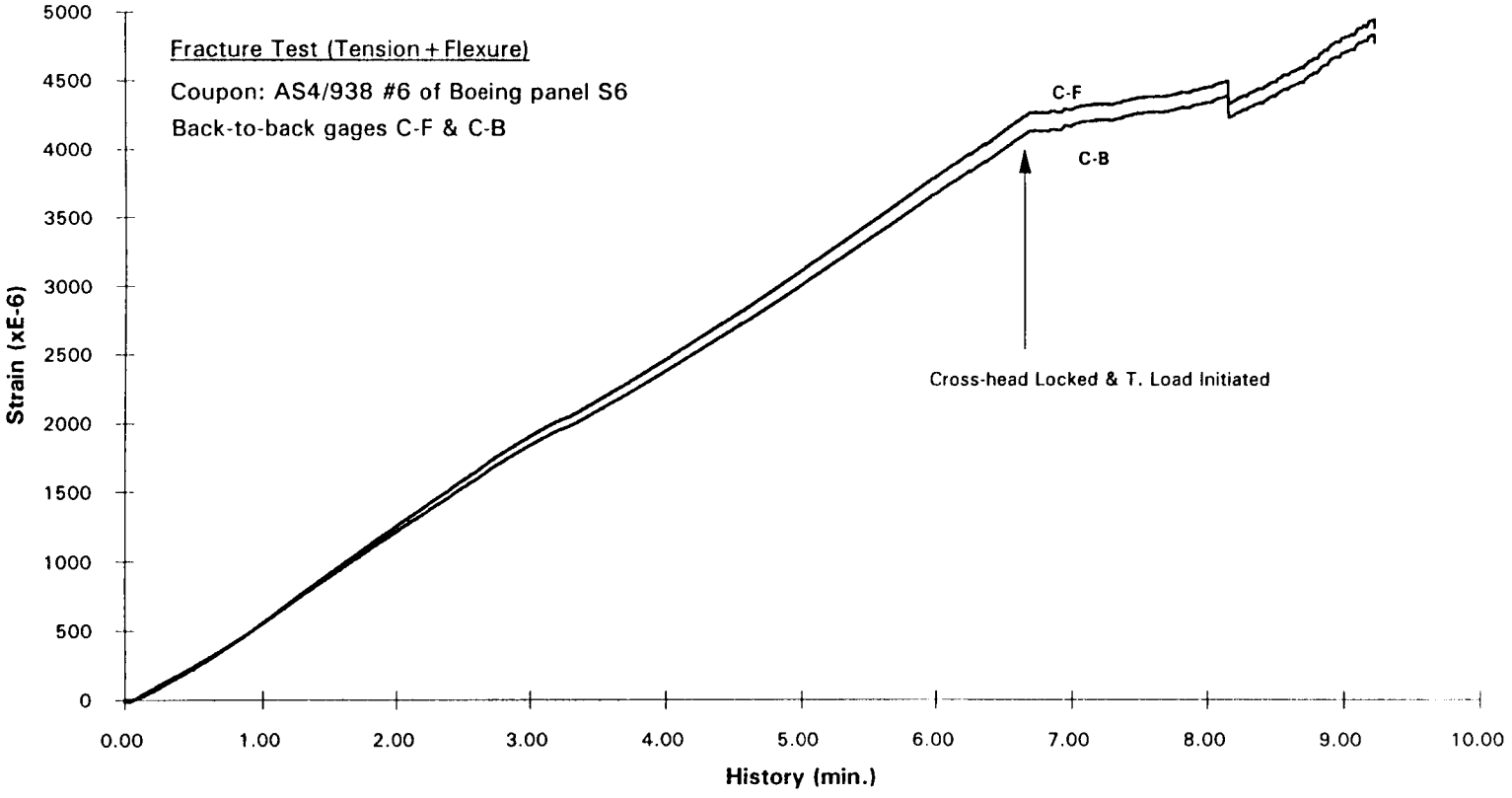
Fracture Test (Tension + Flexure)
Coupon: AS4/938 #6 of Boeing panel S6
Back-to-back gages C-F & C-B
C-F
C-B
Cross-head Locked & T. Load Initiated
Strain (xE-6)
5000
4500
4000
3500
3000
2500
2000
1500
1000
500
0
0.00
1.00
2.00
3.00
4.00
5.00
6.00
7.00
8.00
9.00
10.00
History (min.)

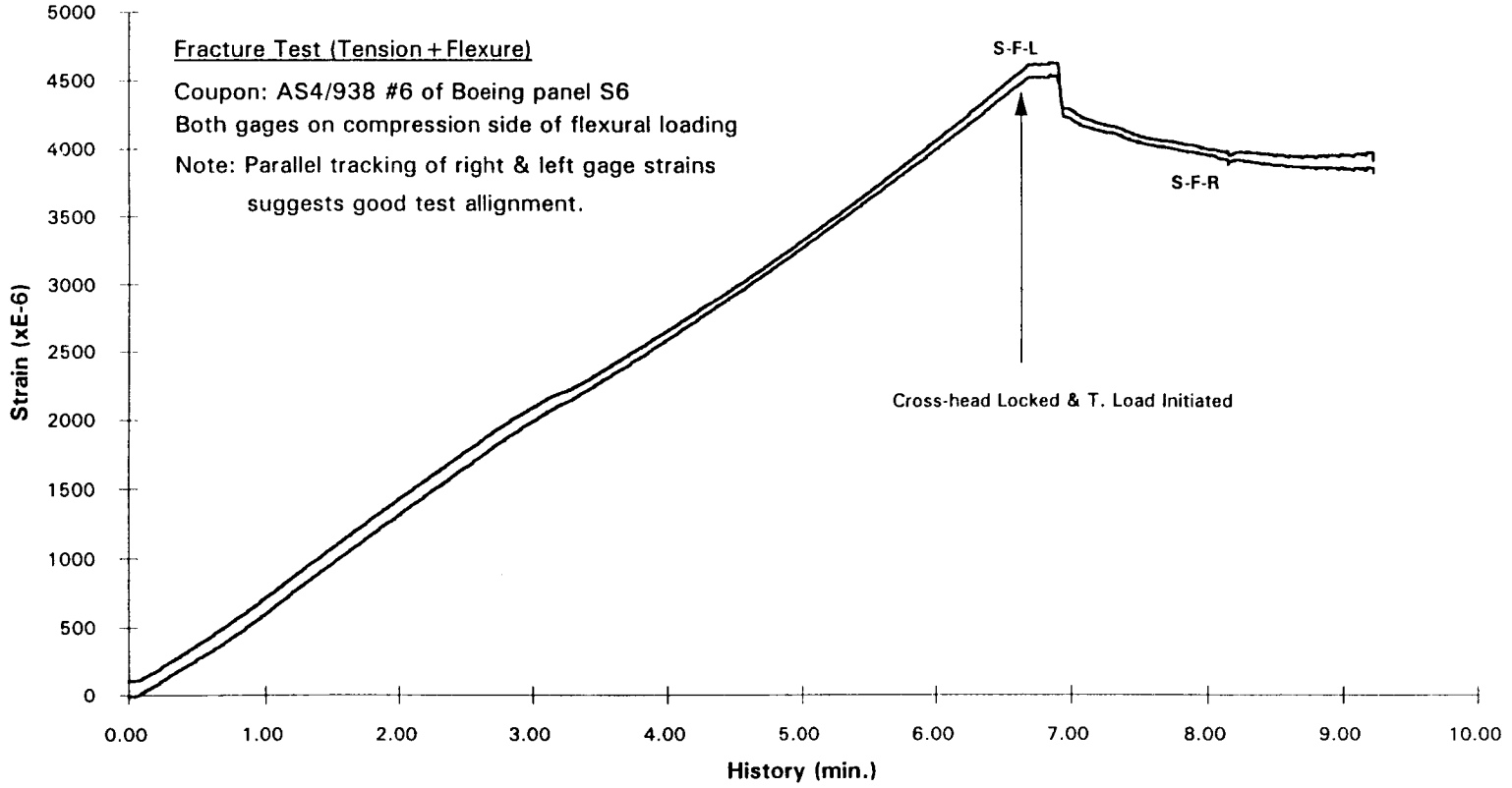
Fracture Test (Tension + Flexure)
Coupon: AS4/938 #6 of Boeing panel S6
Both gages on compression side of flexural loading
Note: Parallel tracking of right & left gage strains
suggests good test allignment.
S-F-L
S-F-R
Cross-head Locked & T. Load Initiated
Strain (xE-6)
5000
4500
4000
3500
3000
2500
2000
1500
1000
500
0
0.00
1.00
2.00
3.00
4.00
5.00
6.00
7.00
8.00
9.00
10.00
History (min.)

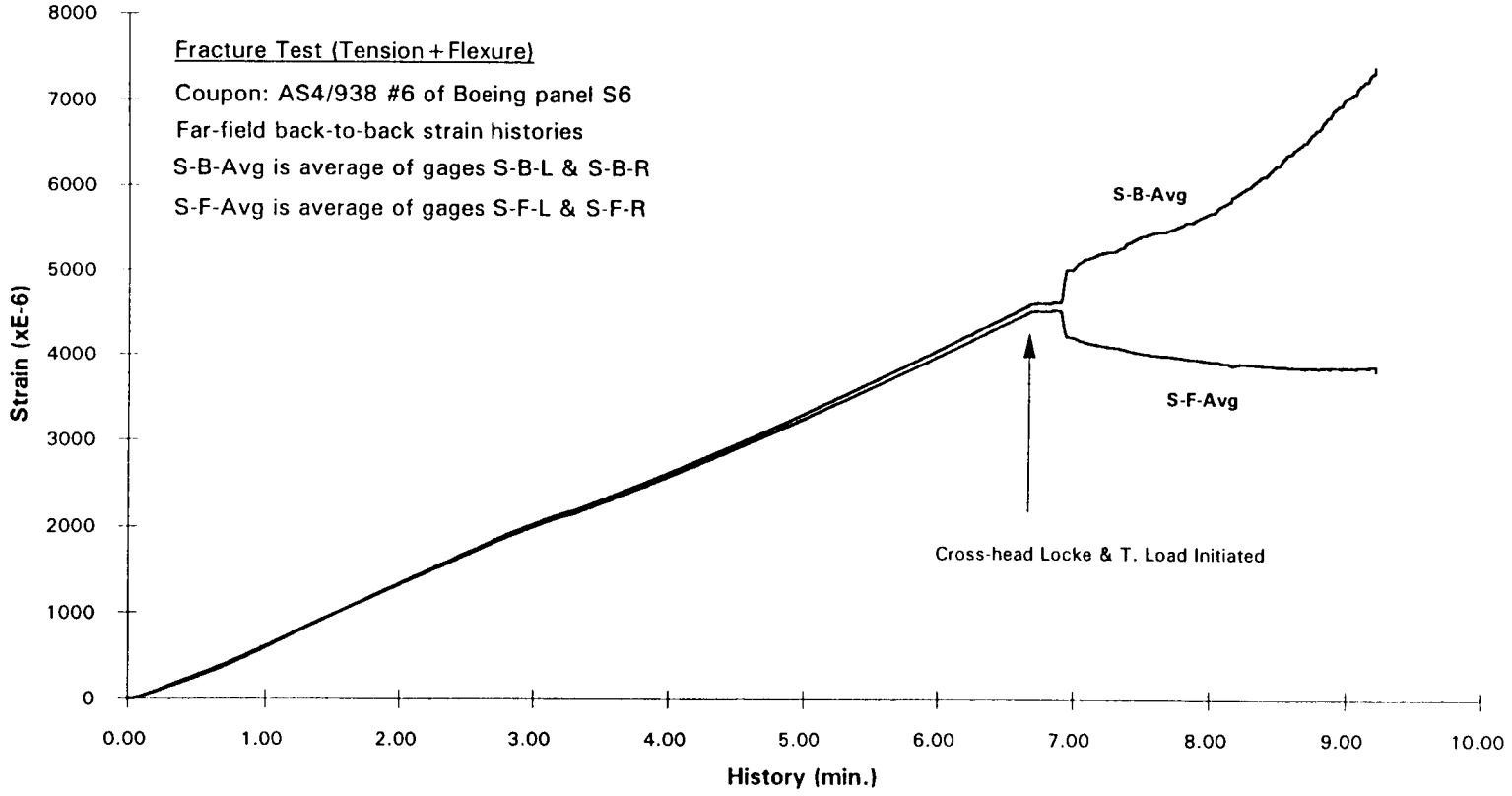
Fracture Test (Tension + Flexure)
Coupon: AS4/938 #6 of Boeing panel S6
Far-field back-to-back strain histories
S-B-Avg is average of gages S-B-L & S-B-R
S-F-Avg is average of gages S-F-L & S-F-R
S-B-Avg
S-F-Avg
Cross-head Locke & T. Load Initiated
Strain (xE-6)
History (min.)
8000
7000
6000
5000
4000
3000
2000
1000
0
0.00
1.00
2.00
3.00
4.00
5.00
6.00
7.00
8.00
9.00
10.00

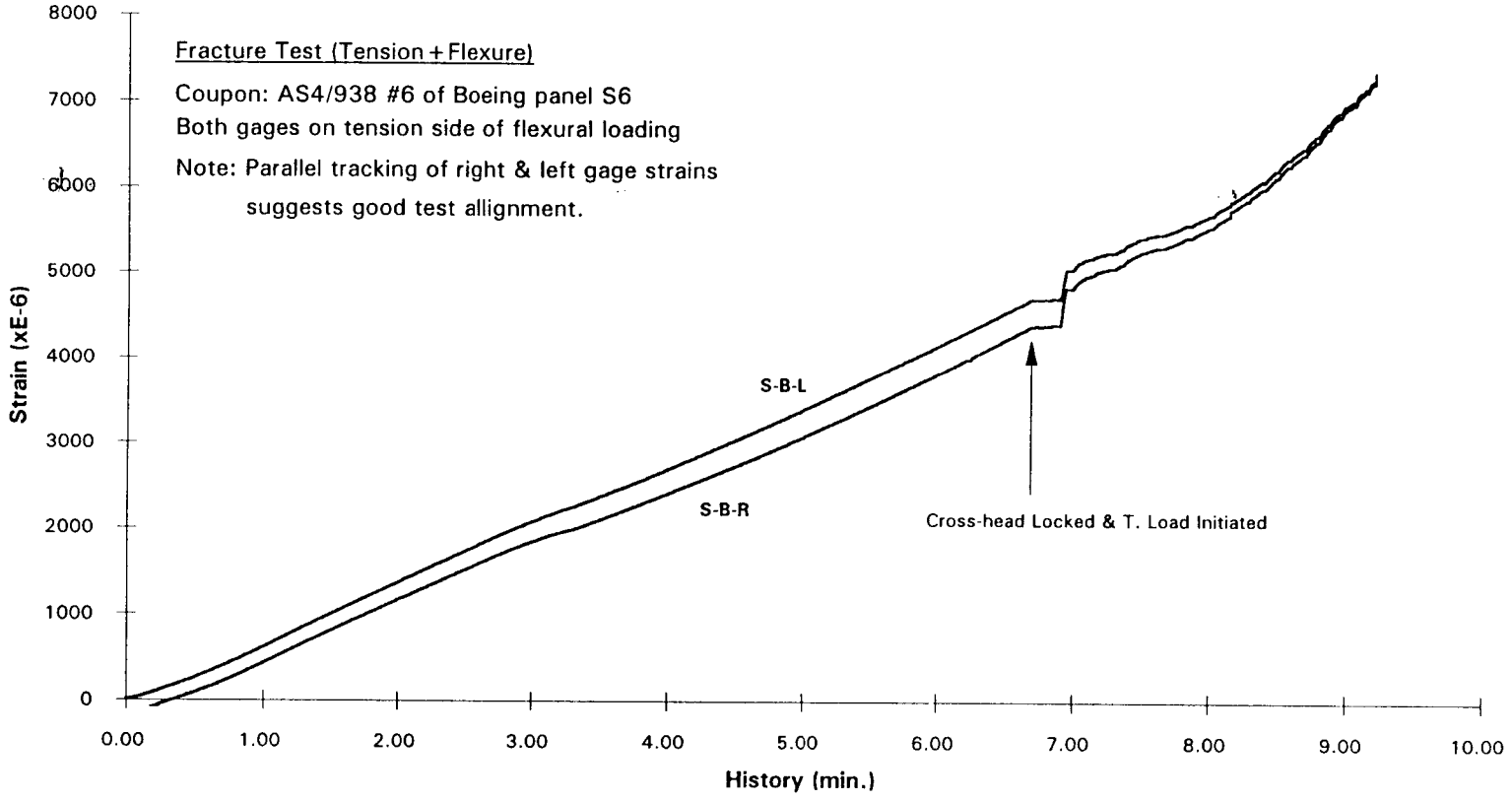
Fracture Test (Tension + Flexure)
Coupon: AS4/938 #6 of Boeing panel S6
Both gages on tension side of flexural loading
Note: Parallel tracking of right & left gage strains
suggests good test allignment.
S-B-L
S-B-R
Cross-head Locked & T. Load Initiated
Strain (xE-6)
History (min.)
8000
7000
6000
5000
4000
3000
2000
1000
0
0.00
1.00
2.00
3.00
4.00
5.00
6.00
7.00
8.00
9.00
10.00